

Internal Report  
DESY F31-86-06  
November 1986

TAU PHYSICS WITH THE CRYSTAL BALL DETECTOR

by

Stefan Keh

Eigentum der	DESY	Bibliothek
Property of		library
Zugang:	10. FEB 1987	
Accessions:		
Leihfrist:	7	days
Loan period:		

**DESY behält sich alle Rechte für den Fall der Schutzrechtserteilung und für die wirtschaftliche Verwertung der in diesem Bericht enthaltenen Informationen vor.**

**DESY reserves all rights for commercial use of information included in this report, especially in case of filing application for or grant of patents.**

**“Die Verantwortung für den Inhalt dieses  
Internen Berichtes liegt ausschließlich beim Verfasser“**

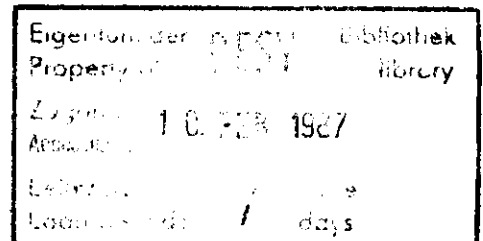
Internal Report  
DESY F31-86-06  
November 1986

# Tau Physics with the Crystal Ball Detector

Stefan M. Keh

Universität Würzburg  
8700 Würzburg, Germany  
*and*  
Deutsches Elektronen-Synchrotron DESY  
2000 Hamburg, Germany

Würzburg 1986.



Ph. D. Dissertation  
Universität Würzburg

# Abstract

With the Crystal Ball Detector at the  $e^+e^-$  storage ring DORIS we have searched for the Higgs boson in radiative decays of the  $\Upsilon$  and  $\Upsilon'$  resonance. We also have searched for lepton number violating decays of the  $\tau$  lepton,  $\tau \rightarrow e\gamma$  and  $\tau \rightarrow e\pi^0$ .

The Higgs particle is searched for in its decay into a  $\tau\bar{\tau}$  pair. Due to its narrow decay width we expect a monochromatic signal in the photon spectrum. Finding no significant structures in the photon spectrum, we obtain upper limits for the product branching ratio (at 90% confidence level):

$$\begin{aligned} \text{BR}(\Upsilon \rightarrow \gamma X \rightarrow \gamma\tau\bar{\tau}) &< (0.6 - 1.6) \times 10^{-3} \quad (M_{\tau\tau} < 9.0 \text{ GeV}) \\ \text{BR}(\Upsilon' \rightarrow \gamma X \rightarrow \gamma\tau\bar{\tau}) &< (0.6 - 3.0) \times 10^{-3} \quad (M_{\tau\tau} < 9.5 \text{ GeV}). \end{aligned}$$

This represents the first search in radiative  $\Upsilon'$  decays. The result for  $\Upsilon$  decays is comparable to that of an earlier experiment. These limits do not exclude a Higgs boson in the Standard Model with 1 Higgs doublet, since theoretical predictions are

$$\text{BR}(\Upsilon, \Upsilon' \rightarrow \gamma\text{Higgs}) \approx 10^{-4} - 10^{-5}.$$

However, the limits can be used to constrain the ratio of vacuum expectation values for models with more than one Higgs doublet. The search for the Higgs boson in its  $\tau\bar{\tau}$  decay mode is particularly important for models which predict this to be the dominant channel. A search in  $c\bar{c}$  type events, characterized by high final state multiplicity, would then be insensitive.

Lepton number violating decays of the  $\tau$  lepton are predicted in 'composite model' theories. Our limits

$$\text{and} \quad \begin{aligned} \text{BR}(\tau \rightarrow e\gamma) &< 3.4 \times 10^{-4} \\ \text{BR}(\tau \rightarrow e\pi^0) &< 4.4 \times 10^{-4} \end{aligned}$$

are considerably lower than previous results. The upper limit for the reaction  $\tau \rightarrow e\gamma$  can be converted into a lower limit on the compositeness mass scale  $\Lambda$  of

$$\Lambda/\sqrt{\alpha} > 65 \text{ TeV},$$

with  $\alpha$  being an unknown coupling constant ( $0.01 < \alpha < 1.00$ ).

# Contents

<b>1</b>	<b>Introduction</b>	<b>1</b>
<b>2</b>	<b>Theory and Summary</b>	<b>2</b>
2.1	Fundamental Interactions . . . . .	2
2.1.1	Quantum Chromodynamics and the Quark Model . . . . .	2
2.1.2	Heavy Vector Mesons . . . . .	4
2.1.3	Electroweak Interaction . . . . .	6
2.2	Properties of the Higgs Boson . . . . .	10
2.2.1	Standard Higgs Boson . . . . .	10
2.2.2	Non-standard Higgs Boson . . . . .	11
2.2.3	Search for Higgs Bosons in $\Upsilon$ Decays . . . . .	12
2.3	Tau Lepton Decays . . . . .	15
2.3.1	Conventional $\tau$ decays . . . . .	15
2.3.2	Unconventional $\tau$ decays . . . . .	16
<b>3</b>	<b>Experimental Layout</b>	<b>18</b>
3.1	DORIS II . . . . .	18
3.2	The Crystal Ball Detector . . . . .	20
3.2.1	Main Ball . . . . .	20
3.2.2	Endcaps . . . . .	21
3.2.3	Tubechambers . . . . .	24
3.2.4	Time of Flight System . . . . .	24
3.2.5	Flasher system . . . . .	25
3.2.6	Luminosity Monitor . . . . .	25
3.2.7	Electronics and Trigger . . . . .	26
3.2.8	Calibration . . . . .	28
<b>4</b>	<b>Datasamples and Production</b>	<b>30</b>
4.1	Datasamples . . . . .	30
4.2	Offline Production . . . . .	31
<b>5</b>	<b>The Decay <math>\Upsilon, \Upsilon' \rightarrow \gamma X \rightarrow \gamma \tau \bar{\tau}</math></b>	<b>35</b>
5.1	Analysis . . . . .	35
5.1.1	Introduction . . . . .	35
5.1.2	Preselection . . . . .	36
5.1.3	Final Selection . . . . .	38
5.2	Acceptance Studies . . . . .	48
5.2.1	Monte Carlo Studies . . . . .	48

5.2.2	Systematic Effects . . . . .	49
5.3	Physics Results . . . . .	50
<b>6</b>	<b>The Decays <math>\tau \rightarrow e\gamma</math> and <math>\tau \rightarrow e\pi^0</math></b>	<b>53</b>
6.1	Analysis . . . . .	53
6.1.1	Introduction . . . . .	53
6.1.2	Selection of $\tau \rightarrow e\gamma$ . . . . .	54
6.1.3	Kinematic Fitting . . . . .	59
6.1.4	Selection of $\tau \rightarrow e\pi^0$ . . . . .	61
6.2	Physics Results . . . . .	62
6.2.1	The Decay $\tau \rightarrow e\gamma$ . . . . .	62
6.2.2	The Decay $\tau \rightarrow e\pi^0$ . . . . .	63
<b>7</b>	<b>Conclusions</b>	<b>64</b>
<b>A</b>	<b>Particle Identification</b>	<b>65</b>
A.1	Introduction . . . . .	65
A.2	Signature of Particles . . . . .	65
A.3	Patterns . . . . .	67
A.4	$\pi^0/\gamma$ separation . . . . .	68
<b>B</b>	<b>Monte Carlo Techniques</b>	<b>72</b>
B.1	Introduction . . . . .	72
B.2	STEP1 . . . . .	72
B.3	STEP2 . . . . .	75
B.3.1	Electromagnetic Interactions . . . . .	75
B.3.2	Hadronic Interactions . . . . .	76
<b>C</b>	<b>Statistical Methods</b>	<b>79</b>
C.1	Introduction . . . . .	79
C.2	Likelihood Function . . . . .	79
C.3	Upper Limits . . . . .	80
C.4	Summary . . . . .	81

# List of Figures

1	Feynman diagram for $e^+e^- \rightarrow q\bar{q}$ . . . . .	3
2	R as function of CMS energy . . . . .	3
3	The $b\bar{b}$ system . . . . .	4
4	Feynman diagram for $e^+e^- \rightarrow \Upsilon, \Upsilon', \dots$ . . . . .	5
5	R as a function of CMS energy . . . . .	5
6	Feynman diagram for B meson production . . . . .	5
7	Feynman diagrams for Higgs production by the Wilczek mechanism . . . . .	12
8	90% upper limit as function of recoil mass, $\Upsilon$ . . . . .	13
9	90% upper limit as function of recoil mass, $\Upsilon'$ . . . . .	13
10	Lower limit $\kappa^2, \Upsilon$ . . . . .	13
11	Lower limit $\kappa^2, \Upsilon'$ . . . . .	13
12	90% upper limit on $\Upsilon \rightarrow \gamma X \rightarrow \gamma\tau\bar{\tau}$ type final state . . . . .	14
13	Feynman diagram for $\tau$ decay . . . . .	15
14	Feynman diagram for subsequent W decay . . . . .	15
15	Feynman diagram for $\tau \rightarrow e \pi^0$ . . . . .	18
16	Layout of Doris and peripherals . . . . .	19
17	Layout of the Crystal Ball detector . . . . .	20
18	Jargon used for the various components . . . . .	22
19	Event display of typical $e^+e^- \rightarrow e^+e^-$ event . . . . .	23
20	Tube chamber setup for 1983 . . . . .	24
21	Tube chamber setup for 1984 . . . . .	24
22	Time of Flight System . . . . .	25
23	Small angle Luminosity Monitor . . . . .	26
24	Hadronic cross section vs. CMS energy for $\Upsilon$ and $\Upsilon'$ . . . . .	30
25	Event display . . . . .	32
26	Group of neighbor crystals . . . . .	33
27	Energy in the endcaps for DBM events. . . . .	37
28	Track energies ( $\sum_{13}$ ) for Bhabha events . . . . .	38
29	Track energies ( $\sum_{13}$ ) for minimum ionizing particles . . . . .	38
30	Total energy for data . . . . .	40
31	Total energy for Monte Carlo $\gamma\tau\bar{\tau}$ . . . . .	40
32	Total energy for separated beam data . . . . .	40
33	z vertex for colliding beam data . . . . .	40
34	z vertex for separated beam data . . . . .	40
35	Offaxis event tracked onaxis . . . . .	41
36	Offaxis event tracked offaxis . . . . .	41
37	Onaxis event tracked onaxis . . . . .	41

38	$\rho$ vertex for colliding beam data . . . . .	42
39	$\rho$ vertex for separated beam data . . . . .	42
40	Total energy versus $z$ vertex for colliding beam data . . . . .	43
41	Total energy versus $\rho$ vertex for colliding beam data . . . . .	43
42	$E_T^2$ for colliding beam data . . . . .	44
43	$E_T^2$ for Monte Carlo $\gamma\tau\bar{\tau}$ events . . . . .	44
44	$E_T^2$ for separated beam data . . . . .	44
45	$E_T^2$ versus $z$ vertex (colliding beams) . . . . .	45
46	$E_T^2$ versus $\rho$ vertex (colliding beams) . . . . .	45
47	Electron energy spectrum from $\tau$ decays . . . . .	47
48	Energy of tracks from DBM events . . . . .	47
49	Detection efficiency for $\Upsilon \rightarrow \gamma X \rightarrow \gamma\tau\bar{\tau}$ . . . . .	49
50	Detection efficiency for $\Upsilon' \rightarrow \gamma X \rightarrow \gamma\tau\bar{\tau}$ . . . . .	49
51	Photon energy for $\gamma e\mu$ final states, $\Upsilon$ . . . . .	51
52	Photon energy for $\gamma e\mu$ final states, $\Upsilon'$ . . . . .	51
53	Photon energy for $\gamma e\mu$ final states, $\Upsilon$ Monte Carlo . . . . .	51
54	Photon energy for $\gamma e\mu$ final states, $\Upsilon'$ Monte Carlo . . . . .	51
55	Photon energy Monte Carlo events, $\Upsilon, \Upsilon' \rightarrow \gamma X \rightarrow \gamma\tau\bar{\tau}$ . . . . .	52
56	90% upper limit as function of recoil mass, $\Upsilon$ . . . . .	53
57	90% upper limit as function of recoil mass, $\Upsilon'$ . . . . .	53
58	Cos(angle) gamma electron vs. cos(angle) gamma others . . . . .	54
59	Total energy for events with an isolated electron gamma pair . . . . .	55
60	Energy ( $\Sigma_{13}$ ) of beamenergy Monte Carlo electrons . . . . .	55
61	Cos(Opening angle), 2 electrons in restframe, data . . . . .	56
62	Cos(Opening angle), 2 electrons in restframe, Monte Carlo . . . . .	56
63	Total energy for $\tau \rightarrow e\gamma$ , Monte Carlo prediction . . . . .	57
64	$E_T$ for data . . . . .	58
65	$E_T$ for Monte Carlo . . . . .	58
66	$E_T^2$ for data . . . . .	58
67	$E_T^2$ for Monte Carlo . . . . .	58
68	Debris energy for $\tau \rightarrow e\gamma$ data . . . . .	59
69	Debris energy for $\tau \rightarrow e\gamma$ Monte Carlo data . . . . .	59
70	Confidence level distribution $\tau \rightarrow e\gamma$ Monte Carlo events . . . . .	60
71	Confidence level distribution Monte Carlo radiative Bhabhas . . . . .	60
72	Confidence level distribution for data . . . . .	60
73	Invariant mass of electron and gamma, data . . . . .	62
74	Invariant mass of electron and gamma, Monte Carlo . . . . .	62
75	Invariant mass of electron and $\pi^0$ , data . . . . .	63
76	Invariant mass of electron and $\pi^0$ , Monte Carlo . . . . .	63

77	Electron of 5 GeV . . . . .	66
78	Muon of 5 GeV . . . . .	66
79	Ionization in 15.7 $X_0$ of NaI(Tl) . . . . .	66
80	Landau distribution . . . . .	66
81	Seen energy for 5 GeV pions . . . . .	67
82	Pion of 5 GeV . . . . .	67
83	Definition of $E_1, E_2, E_4$ and $E_{13}$ . . . . .	68
84	$\frac{E_1}{E_4}$ for electrons . . . . .	68
85	$\frac{E_4}{E_{13}}$ for electrons . . . . .	68
86	$\frac{E_1}{E_4}$ for pions . . . . .	69
87	$\frac{E_4}{E_{13}}$ for pions . . . . .	69
88	$\frac{E_1}{E_2}$ for muons . . . . .	69
89	$\frac{E_4}{E_{13}}$ for muons . . . . .	69
90	Probability for a $\pi^0$ to pass a photon pattern cut . . . . .	69
91	$\pi^0$ of 1500 MeV . . . . .	70
92	Gamma of 1500 MeV . . . . .	70
93	Shower mass for $\pi^0$ s . . . . .	71
94	Shower mass for gammas . . . . .	71
95	Lowest order diagram for $e^+e^- \rightarrow \tau\bar{\tau}$ . . . . .	73
96	Corrections to $e^+e^- \rightarrow \tau\bar{\tau}$ . . . . .	74
97	Resolution versus electron energy . . . . .	77
98	Resolution versus beam displacement . . . . .	77
99	Energy deposited by pions in BGO . . . . .	78
100	Longitudinal shower profile for pions in BGO . . . . .	78
101	Likelihood as function of amplitude A . . . . .	80

## List of Tables

1	Quarks and their quantum numbers . . . . .	2
2	Known $\tau$ decay modes . . . . .	16
3	Trigger Criteria . . . . .	27
4	Luminosities and number of resonance decays for $\Upsilon$ and $\Upsilon'$ . . . . .	31
5	Preselection criteria and transmission of subsequent cuts . . . . .	37
6	Final selection criteria and transmission of subsequent cuts . . . . .	46
7	Tubechamber efficiencies . . . . .	49
8	Number of events for $\gamma e \mu$ final state . . . . .	52
9	Selection criteria for the decay $\tau \rightarrow e \gamma$ . . . . .	57
10	Selection criteria for the decay $\tau \rightarrow e \pi^0$ . . . . .	61
11	Upper limits for $\tau \rightarrow e \gamma$ as function of peak position . . . . .	62
12	Upper limits for $\tau \rightarrow e \pi^0$ as function of peak position . . . . .	63
13	Particle types and their interactions in NaI(Tl) . . . . .	65
14	Patterncuts for different particle types . . . . .	70

# 1 Introduction

High energy physics investigates the basic structures of nature. This includes elementary particles as the building blocks and gauge bosons mediating the interactions between them. Currently we know 4 interactions, strong, electromagnetic, weak and gravitational.

The weak and electromagnetic interactions are unified in the Glashow-Weinberg-Salam [1] model based on the symmetry group  $SU(2) \times U(1)$ . The predicted neutral currents [2] as well as the gauge bosons  $W^\pm$  and  $Z^0$  were found experimentally [3]. In particular the latter discovery with masses close to the predicted values was a great success for the Glashow-Weinberg-Salam model.  $W^\pm$  and  $Z^0$  acquire mass through the mechanism of spontaneous symmetry breaking. This mechanism leads to a scalar particle, the Higgs boson, [4] which so far has not been observed.

The first part of this work is therefore devoted to a search for this particle in the  $\Upsilon$  region, i.e. in the mass range  $M_{\text{Higgs}} \leq 10 \text{ GeV}$ .

The  $\Upsilon$  itself was first found in the di-muon mass spectrum in proton-nucleon collisions at Fermilab [5]. The effort to find it also in  $e^+e^-$  collisions [6] revealed a whole spectrum of very narrow resonances. This led to the interpretation of this new particle as a bound state of a b quark and its antiquark.

The second part of this thesis deals with exotic decay modes of the  $\tau$  lepton. The  $\tau$  was discovered in 1975 by the MARK I collaboration at the SPEAR storage ring at Stanford [7]. Many experiments provided proof that it joins the familiar family of the leptons  $e, \nu_e, \mu, \nu_\mu$ .

Composite model theories try to reduce the number of elementary particles (quarks and leptons) by introducing more fundamental building blocks, e.g. so called preons. A consequence of these models is the prediction of reactions which are forbidden in the standard Glashow-Weinberg-Salam model, such as  $\tau \rightarrow e\gamma$  and  $\tau \rightarrow e\pi^0$ . Since those decay modes are expected to be very rare previous experiments may not have seen it. This work presents the most sensitive search for these reactions.

The chapters of this thesis are organized as follows: First we give an overview of theoretical ideas connected to Higgs particles and the  $\tau$  lepton in chapter 2. A description of the experimental setup, the Crystal Ball detector and the storage ring DORIS, follows in section 3. The data samples taken on the various  $\Upsilon$  resonances together with an introduction into the software tools needed for the data analysis is given in chapter 4. The next two chapters are devoted to the analyses for a Higgs search (chapter 5) and exotic  $\tau$  decays (chapter 6). Conclusions in chapter 7 summarize the achieved results and compare with other experiments and theoretical predictions.

Three appendices on particle identification in the Crystal Ball detector, Monte Carlo techniques and statistical methods are included.

## 2 Theory and Summary

In this section we will discuss the fundamental forces which govern interactions between particles. Special emphasis will be given to the unified electromagnetic and weak interactions, the Glashow-Weinberg-Salam model, and the Higgs particle which emerges from this theory. A discussion will follow of its properties together with results from an experimental search for this particle.

In a second part we will describe properties of the  $\tau$  lepton. In particular those decays will be investigated which are postulated by composite models. These theories predict various exotic processes, two of which will be investigated in more detail.

### 2.1 Fundamental Interactions

Presently we believe that matter is composed of spin 1/2 fermions, namely quarks and leptons. There are four fundamental forces by means of which these particles interact, the strong, electroweak unification of electromagnetic and weak, and gravitational force. The last one, being very weak at the relevant energies, will be neglected in the further discussion. Quarks and leptons participate in the electroweak interaction, quarks in addition are subject to the strong interaction. In the following we will discuss these fundamental forces in more detail.

#### 2.1.1 Quantum Chromodynamics and the Quark Model

With the large number of elementary particles found in the 1950s and 1960s it became clear that they should be composed of a comparatively small number of truly elementary particles. A first trial was due to Sakata [8], who tried to use the proton, the neutron and the  $\Delta$  hyperon as basic building blocks. Combining two of them yields mesons. By trying to construct baryons as a triplet of these fundamental particles however this model was ruled out since a lot of particles, unwanted since unobserved in nature, were predicted. A much more successful approach is the quark model due to Gell-Mann and Zweig, see reference [9]. They postulated three objects (u, d, s), now called flavor, with fractional charge and baryon number (see table 1). They carry an abstract quantum number, called color, which can take on three values (red, green and blue) [10]. Combining 2

	Charge	Baryon number	Strangeness
u	2/3	1/3	0
d	-1/3	1/3	0
s	-1/3	1/3	-1

Table 1: Quarks and their quantum numbers

or 3 quarks and antiquarks yielded the spectrum of observed particles and predicted

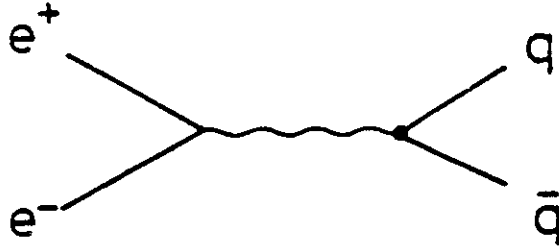


Figure 1: Feynman diagram for  $e^+e^- \rightarrow q\bar{q}$

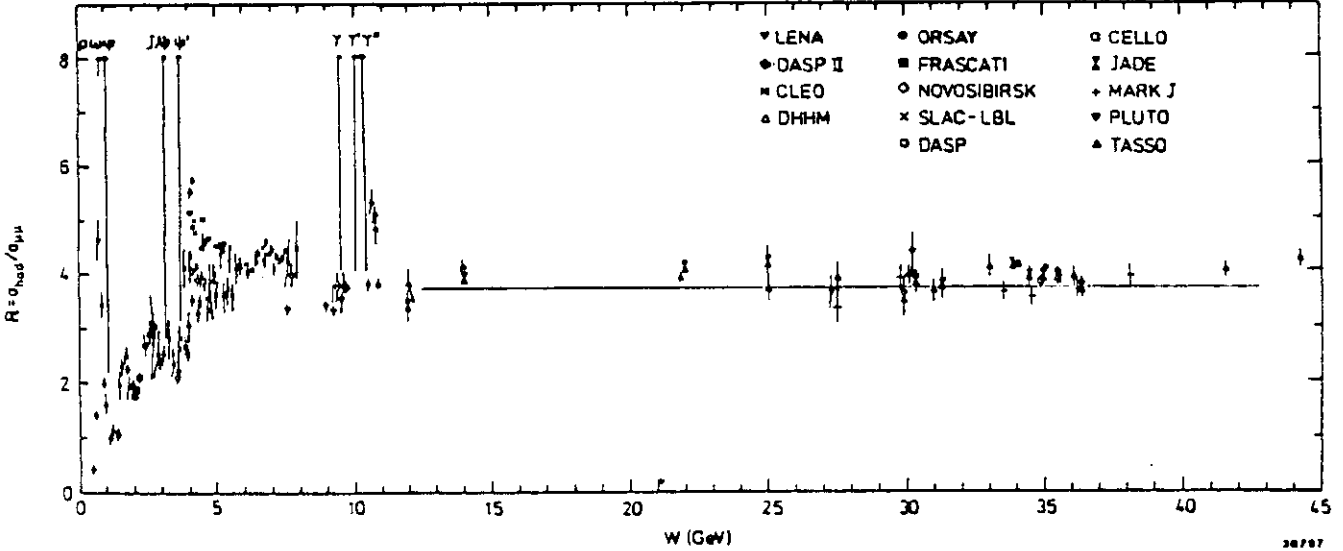


Figure 2:  $R$  as function of CMS energy

states which were found later experimentally, e.g. the  $\Omega^-$ . From the requirement that the observed particles in nature are color singlets, it follows that it is impossible to observe isolated quarks. One of the remarkable successes of the quark model is the correct prediction for

$$R = \frac{\sigma(e^+e^- \rightarrow q\bar{q} \rightarrow \text{hadrons})}{\sigma(e^+e^- \rightarrow \mu\bar{\mu})} = N_c \times \sum Q_i^2$$

where  $\sigma(e^+e^- \rightarrow q\bar{q})$  denotes the cross section for production of a quark-antiquark pair annihilating with probability 1 into hadrons in  $e^+e^-$  annihilations in lowest order (figure 1) and  $\sigma_{e^+e^- \rightarrow \mu\bar{\mu}}$  is the cross section for a pair of muons.  $N_c$  is the number of colors and  $Q_i$  the charge of the quark accessible in pair production at the given CMS energy. Figure 2 shows  $R$  as a function of CMS energy; indicated are the expectations for  $N_c = 3$ . The figure shows spikes at the  $\rho$ ,  $\omega$ ,  $J/\psi$  and  $Y$  mass due to resonant production of these particles. Clearly,  $R$  defined above applies only in between these resonances.

The interaction between colored quarks proceeds via the exchange of gluons which couple to the color charge. Quantum chromodynamics (QCD) is the corresponding non-Abelian gauge theory, based on the gauge group  $SU(3)$  of color transformations. Due

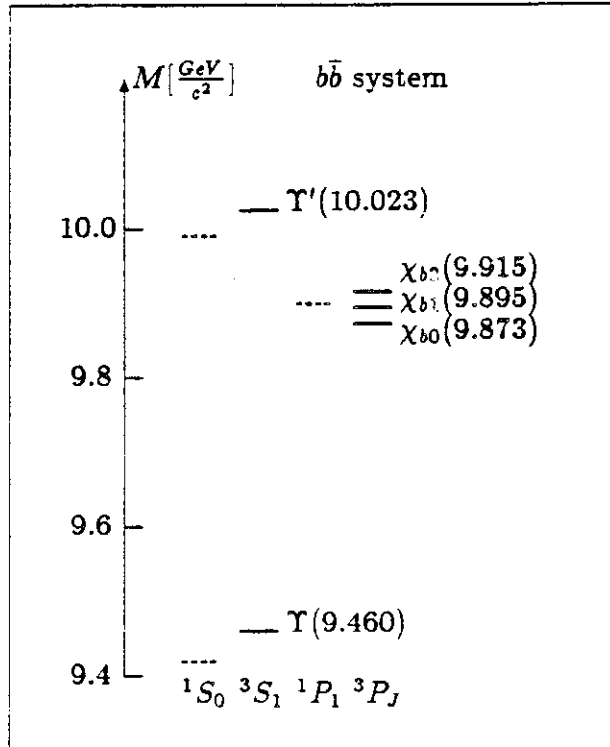


Figure 3: The  $b\bar{b}$  system. The dashed lines mark states which are not yet found. The subscript of the  $\chi$  lines denotes the total spin of the state.

to the  $SU(3)$  group governing the strong interaction we have an octet of colored gluons which can also interact among themselves. This implies the possible existence of bound states of gluons, see reference [11] for a detailed discussion.

### 2.1.2 Heavy Vector Mesons

In analogy to positronium, where the  $e^+$  and  $e^-$  form a bound state, heavy quarks can also form bound states. The  $\Upsilon$  is such a bound state of a quark and its antiquark. A level scheme of the various bound states is displayed in figure 3. The  $J^{PC} = 1^{--}$  states ( $\Upsilon, \Upsilon', \dots$ ) can be produced in  $e^+e^-$  annihilations via the process depicted in figure 4, since they have the same quantum numbers as the photon. A typical excitation curve for the production of the  $\Upsilon$  meson is shown in figure 5 where we display  $R$  as a function of CMS energy. The states up to the  $\Upsilon''$  lie below threshold for pair production of mesons containing one heavy  $b$  quark, by the process in figure 6. Thus the  $\Upsilon$  mesons decay predominately by annihilation into 3 gluons (the decay of a vector meson with  $J^{PC} = 1^{--}$  into 2 massless particles such as gluons is forbidden by conservation of angular momentum, see ref [12] and C parity) or 1 photon and 2 gluons. The gluons subsequently fragment into hadrons. The width of the  $\Upsilon$  resonance in figure 5 is entirely due to the energy resolution of the  $e^+e^-$  collider (see chapter 3). The resonance itself has a total width of about 43 keV. This width, which is incredibly small for a strong

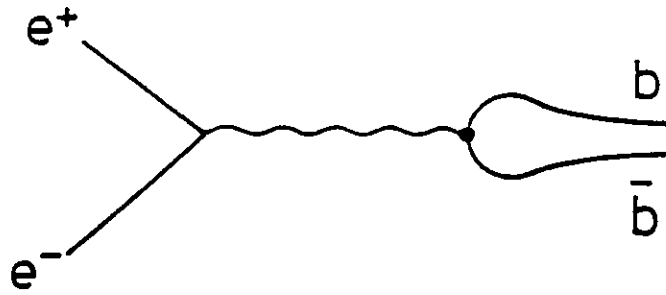


Figure 4: Feynman diagram for  $e^+e^- \rightarrow \Upsilon, \Upsilon', \dots$

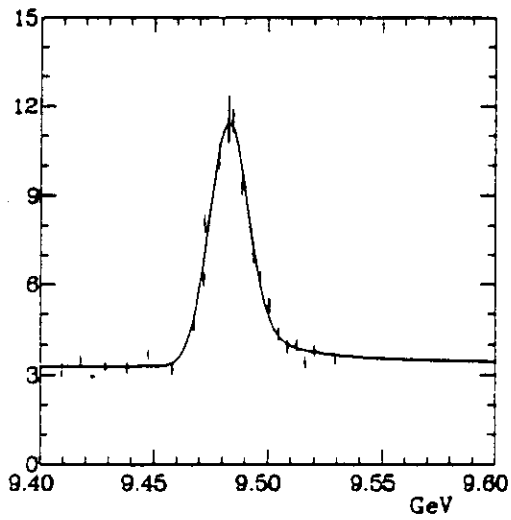


Figure 5:  $R$  as a function of CMS energy

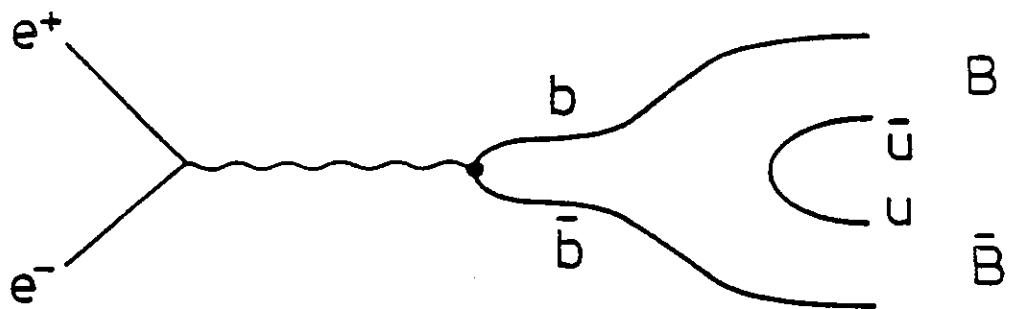


Figure 6: Feynman diagram for B meson production

interacting particle, can be understood by the ‘OZI’ rule [13]. This rule has been used to explain the predominance of the decay of  $\phi(1012)$  into KK over  $\pi\pi\pi^0$ , where naively the latter decay would be favored by phasespace. This rule states that any decay with disconnected quark lines between initial and final states is suppressed.

### 2.1.3 Electroweak Interaction

The first theory of weak interactions was due to Fermi. He postulated a four-fermion vertex with a coupling constant  $G_F \approx 10^{-5}/M_p^2$  ( $M_p =$  proton mass) to describe e.g. the nuclear beta decay. From dimensional arguments the cross section for  $\nu n \rightarrow e p$  scales like

$$\sigma_{\nu n \rightarrow ep} \approx G_F^2 \times S$$

where  $S$  is the CMS energy squared. Such a cross section will violate unitarity above a certain center of mass (CMS) energy. This problem can be cured by introducing a heavy boson  $W^\pm$  to mediate the charged current interaction as the photon does in QED. But this in turn will cause unitarity problems in

$$e^+e^- \rightarrow W^+W^-$$

thus calling for an ad-hoc introduction of a neutral boson.

A much more elegant and systematic approach is to unify electromagnetic and weak interactions. This so called ‘Standard Model’ was developed by Glashow, Weinberg and Salam [1]. The underlying non-Abelian symmetry group is  $SU(2) \times U(1)$  with the gauge groups  $SU(2)$  governing weak isospin and  $U(1)$  governing weak hypercharge. The four real parameters of the two groups lead to four gauge fields of spin 1:  $\vec{W}_\mu$  and  $B_\mu$ . The physical quanta are linear combinations:

$$\begin{aligned} W_\mu^\pm &= \frac{1}{\sqrt{2}}(W_{\mu_1} \mp iW_{\mu_2}) \\ Z_\mu &= W_{\mu_3} \cos \Theta_W - B_\mu \sin \Theta_W \\ A_\mu &= W_{\mu_3} \sin \Theta_W + B_\mu \cos \Theta_W \end{aligned} \quad (1)$$

where the Weinberg angle  $\Theta_W$  is a parameter to be determined experimentally,  $W^\pm$  and  $Z^0$  are the bosons mediating the charged and neutral weak currents and  $A$  is the usual photon field of QED.

This theory distinguishes left- and right-handed fermions from the very beginning by coupling only left-handed fermions and right-handed antifermions to the  $W^\pm$ . The  $Z^0$  and  $A$  field both couple to right- and left-handed fermions, although with different strengths. The left-handed fermions are grouped into weak isospin doublets, the right-

handed fermions into singlets, as is shown in the following table.

	Fermions			Q	weak $I_3$	weak Y
leptons	$\begin{pmatrix} \nu_e \\ e \end{pmatrix}_L$	$\begin{pmatrix} \nu_\mu \\ \mu \end{pmatrix}_L$	$\begin{pmatrix} \nu_\tau \\ \tau \end{pmatrix}_L$	$\begin{pmatrix} 0 \\ -1 \end{pmatrix}$	$\begin{pmatrix} 1/2 \\ -1/2 \end{pmatrix}$	$\begin{pmatrix} -1 \\ -1 \end{pmatrix}$
quarks	$\begin{pmatrix} u \\ d' \end{pmatrix}_L$	$\begin{pmatrix} c \\ s' \end{pmatrix}_L$	$\begin{pmatrix} t \\ b' \end{pmatrix}_L$	$\begin{pmatrix} 2/3 \\ -1/3 \end{pmatrix}$	$\begin{pmatrix} 1/2 \\ -1/2 \end{pmatrix}$	$\begin{pmatrix} 1/3 \\ 1/3 \end{pmatrix}$
leptons	$e_R$	$\mu_R$	$\tau_R$	-1	0	-2
quarks	$u_R$	$c_R$	$t_R$	2/3	0	4/3
	$d_R$	$s_R$	$b_R$	-1/3	0	-2/3

Q is the charge,  $I_3$  the third component of weak isospin and Y the weak hypercharge. The relationship between these quantum numbers is given by the analogue to the Gell-Mann Nishijima equation <sup>1</sup>

$$Q = I_3 + Y/2$$

The lower components of the left-handed quarks,  $d', s', b'$  are related to the quarks of the strong interaction  $d, s, b$  by a unitary transformation  $U_{qq'}$ , the so called Kobayashi-Maskawa matrix [14].

One important consequence of the model was the successful prediction of weak neutral currents

$$e + \nu_\mu \rightarrow e + \nu_\mu$$

mediated by the neutral  $Z^0$  boson.

Unfortunately at this stage, the above model predicts the gauge bosons to be massless. This is in contradiction to the short range nature of the weak interaction (which corresponds to a massive exchange boson). Introducing a mass term by hand into the Lagrangian would destroy the gauge invariance and thus the renormalizability of the theory. This can be solved by introducing the concept of 'spontaneous symmetry breaking' via the Higgs mechanism [4]. All is needed is a  $SU(2) \times U(1)$  gauge group with a groundstate of the Lagrangian, usually called the vacuum, of non zero expectation value. By construction the Lagrangian stays invariant, but the underlying symmetry is broken spontaneously.

This is a well known phenomenon in physics. For example, an infinitely extended ferromagnet is described by a Lagrangian which is invariant under space rotations. In the ground state this symmetry is apparently broken since the elementary spins

<sup>1</sup>This equation indicates that the photon (coupling to the electric charge Q) has to be a linear combination of the gauge fields W and B, see equation 1.

are aligned in a particular direction. There is, however, an infinite number of such groundstates which can be reached by rotation.

The symmetry breaking in the ground state leads to a massless scalar particle, a so-called Goldstone boson [15], for each degree of freedom in which the theory is spontaneously broken. The degrees of freedom associated with these particles can be absorbed, by virtue of Goldstones theorem [16], into additional degrees of freedom for the gauge bosons, e.g. longitudinal polarization which, in turn, is equivalent to massive gauge bosons.

The standard model introduces one complex SU(2) doublet of scalar fields

$$\Phi = \begin{pmatrix} \Phi_1 + i\Phi_2 \\ \Phi_3 + i\Phi_4 \end{pmatrix} \quad \Phi_i = \text{real.}$$

Introducing a self interaction potential of the form

$$V(\Phi) = \mu^2(\Phi^\dagger \Phi) + \lambda(\Phi^\dagger \Phi)^2$$

with  $\lambda > 0$  and  $\mu^2 < 0$  leads to a spontaneous broken mode. The vacuum expectation values of  $\Phi$  is given by

$$\langle \Phi^\dagger \Phi \rangle_{\text{vacuum}} = \frac{-\mu^2}{2\lambda}$$

The choice of

$$\Phi_{\text{vacuum}} = \frac{1}{\sqrt{2}} \begin{pmatrix} 0 \\ v \end{pmatrix}$$

results in a vacuum expectation value of

$$v = \left( \frac{-\mu^2}{\lambda} \right)^{\frac{1}{2}}.$$

Three of the four components  $\Phi_i$  can be identified as Goldstone bosons. They can be absorbed into the helicity 0 degrees of freedom for 3 of the 4 gauge fields, thus making  $W^\pm$  and  $Z$  massive. The gauge boson associated with  $U(1)_{em}$ , the photon, has to remain massless. Therefore one real scalar field survives. It is called the Higgs boson.

It is obvious, that the masses generated via symmetry breaking, of  $W^\pm$  and  $Z$  are related to the vacuum expectation value  $v$  of the Higgs field  $\Phi$  namely

$$M_W = \frac{gv}{2}$$

with  $g \sin \Theta_W = e$  and

$$M_Z = \frac{gv}{2 \cos \Theta_W}$$

The lepton and quark masses are determined similarly by a Yukawa type coupling to be

$$M_f = \frac{g_f v}{2}$$

where  $g_f$  are free parameters to be determined by experiment.

The vacuum expectation value  $v$  can be determined by comparison of the Fermi-type point interaction of the charged weak current processes such as  $\mu$  decay with the standard model prediction. In the low energy regime both should yield identical results. Thus

$$\frac{G_F}{\sqrt{2}} = \frac{g^2}{8M_W^2}$$

and

$$v^2 = \frac{1}{\sqrt{2}G_F} \approx (249 \text{ GeV})^2$$

This can be used to predict the masses of W and Z to be

$$M_W^2 = \frac{(37.3 \text{ GeV}/c^2)^2}{\sin^2 \Theta_W}$$

and

$$M_Z = \frac{M_W}{\cos \Theta_W}$$

With a measurement of  $\sin \Theta_W$  (e.g. from neutrino scattering experiments [20]) one predicts

$$M_W = (81.8 \pm 1.8) \text{ GeV}/c^2 \quad \text{and} \quad M_Z = (92.6 \pm 1.7) \text{ GeV}/c^2$$

in excellent agreement with experimental results from the  $p\bar{p}$  collider experiments [20].

## 2.2 Properties of the Higgs Boson

### 2.2.1 Standard Higgs Boson

We will discuss the properties and decay modes and hence the possibilities for experimental detection of a standard Higgs boson as it was introduced in the previous section:

- It has to be a scalar ( $J=0$ ) particle, since it gives the helicity zero degrees of freedom to the  $W^\pm$  and  $Z$  bosons, thus making them massive
- Since the photon has to be massless, the Higgs has to be neutral. This is due to the fact that the neutral part of the complex isodoublet Higgs field has a non-zero vacuum expectation value.
- The mass of the Higgs is given by

$$M_H^2 = -2\mu^2 = 2\lambda v^2$$

Unfortunately  $\lambda$  is a parameter not predicted by the theory. There exist, however, limits since a very big value of  $\lambda$  would imply strong self interactions and render the simple potential of the form  $V(\Phi) = \mu^2(\Phi^\dagger\Phi) + \lambda(\Phi^\dagger\Phi)^2$  questionable. On the other hand the Higgs boson cannot be arbitrary light. Higher order corrections to self- interactions modify the potential and result in a lower limit on the mass. These arguments constrain the Higgs mass to  $O(7 \text{ GeV}/c^2) \leq M_H \leq O(1 \text{ TeV}/c^2)$  [17]. This mass constraint is only true in the minimal scheme with one complex Higgs doublet. With more than one doublet (see below), the only stringent limit comes from experimental searches for  $K^+ \rightarrow \pi^+ \text{Higgs} \rightarrow \pi^+ \mu^+ \mu^-$  [18]. The resulting lower limit is  $325 \text{ MeV}/c^2$ .

- The decay modes of the Higgs are determined by the strength of its coupling to ordinary particles. The coupling to any particle X which gets its mass via spontaneous symmetry breaking is given by

$$g_{XXH} = \frac{2M_X}{v} = \frac{M_X}{123 \text{ GeV}/c^2} \quad (2)$$

where  $M_X$  denotes the mass of X.

The following characteristics result from the proportionality of the coupling with mass:

- The Higgs will have the largest branching ratio into the heaviest accessible pair of fermions. Therefore it clearly does not obey lepton universality.
- There is no lowest order coupling to  $\gamma\gamma$  or  $gg$  ( $g$ =gluon).

- The total width of the Higgs particle depends on the number of open decay channels and thus on its mass. For  $M_H < M_Z$  one finds [19] :

$$\Gamma_{tot} = M_H \frac{G_F}{4\sqrt{2}\pi} \sum_{i=1}^{N_f} N_c M_f^2 \left(1 - \frac{4M_f^2}{M_H^2}\right)^{3/2} \quad N_c = \begin{cases} 1 & \text{for leptons} \\ 3 & \text{for quarks} \end{cases}$$

This means that for the masses accessible in this work ( $M_H \leq 10$  GeV with a width of order 1 keV) the Higgs should show up as a very narrow resonance.

### 2.2.2 Non-standard Higgs Boson

In principle there is no reason to have only one complex doublet of Higgs fields. It is just the simplest possibility. There are however constraints from experimental data on the structure of the Higgs sector. In the case of one complex doublet the parameter  $\rho$  turns out to be (except for small radiative corrections)

$$\rho = \frac{M_W^2}{M_Z^2 \cos^2 \Theta_W} = 1$$

The experimental results from  $M_W$  and  $M_Z$  [3]

$$M_W = (81.8 \pm 1.8) \text{ GeV}/c^2 \quad \text{and} \quad M_Z = (92.6 \pm 1.7) \text{ GeV}/c^2$$

together with  $\sin^2 \Theta_W$  from neutrino scattering experiments [20]

$$\sin^2 \Theta_W = (0.223 \pm 0.006)$$

results in an experimental value for  $\rho$

$$\rho = (1.006 \pm 0.008)$$

It can be shown that the prediction for  $\rho$  stays at 1 for an arbitrary number of Higgs doublets [21]. Weak isospin triplets, however, would need adjustment of model parameters to keep  $\rho$  at 1. In the following we refer to extensions of the Higgs sector containing doublets only.

The introduction of two complex Higgs doublets results in additional Higgs bosons, some of them being charged. There is a certain freedom in choice which of the two Higgs fields couples to which type of particles. One possible scenario is to have one Higgs doublet to couple to down-type quarks and leptons, the other one to up-type quarks [22]. This could result in an enhancement of the Higgs coupling to  $\tau$  leptons over  $c$  quarks. At the same time the production rate of a Higgs boson can be enhanced if this happens via coupling to down-type quarks (see next section).

Summarizing one can say that enlargements of the minimal scheme with one Higgs doublet can result in large changes of production, decay widths and branching fractions for Higgs bosons. The only stringent limitation seems to come from the closeness of the  $\rho$  parameter to 1, thus calling for a doublet structure.

### 2.2.3 Search for Higgs Bosons in $\Upsilon$ Decays

Heavy quarkonia provide a very good possibility for Higgs searches. This was first realized by Wilczek [23] who calculated the width for the decay of a bound state of a heavy quark-antiquark pair into a Higgs boson via emission of a photon. The relevant Feynman graphs are given in figure 7. The rate in the minimal scheme is given by

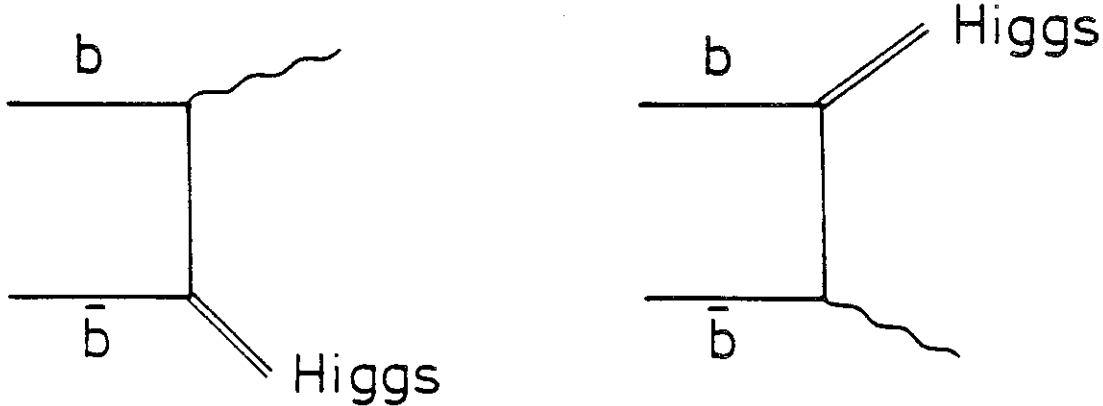


Figure 7: Feynman diagrams for Higgs production by the Wilczek mechanism

$$\frac{\text{BR}(V \rightarrow \gamma H)}{\text{BR}(V \rightarrow \mu^+ \mu^-)} = \frac{G_F M_V^2}{4\sqrt{2}\pi\alpha} \left(1 - \frac{M_H^2}{M_V^2}\right) \quad (3)$$

where  $V$  denotes the decaying vector resonance and  $G_F$  the Fermi constant. The Higgs boson itself would, according to equation 2, decay into a pair of  $c$  quarks or  $\tau$  leptons in the ratio  $\approx 3/1$ . The higher decay rate to charmed quarks is due to the approximately equal masses of  $c$  quark and  $\tau$  lepton and the factor 3 from color. QCD radiative corrections [24] reduce the above prediction by about a factor 2.

In this work we searched for final states containing a photon and a pair of  $\tau$  leptons, corresponding to the reaction

$$\Upsilon, \Upsilon' \rightarrow \gamma \text{Higgs} \rightarrow \gamma \tau^+ \tau^-$$

Since we do not observe any significant signal in the photon spectrum (for details see chapter 5) we calculate an upper limit (at 90% confidence level) as a function of the Higgs mass. In figures 8 and 9 these limits are shown for the  $\Upsilon$  and  $\Upsilon'$  data sets, respectively. The branching ratios predicted by the Wilczek mechanism for the minimal scheme (equation 3) are in the range from  $10^{-4}$  to  $10^{-5}$ . This is clearly below our experimental sensitivity.

In the treatment of non-standard Higgses, in particular with 2 complex doublets, it was shown that

- the branching fraction for  $\Upsilon \rightarrow \gamma \text{Higgs}$  could be enhanced due to different Higgses giving mass to the up- and down-type sector [22]

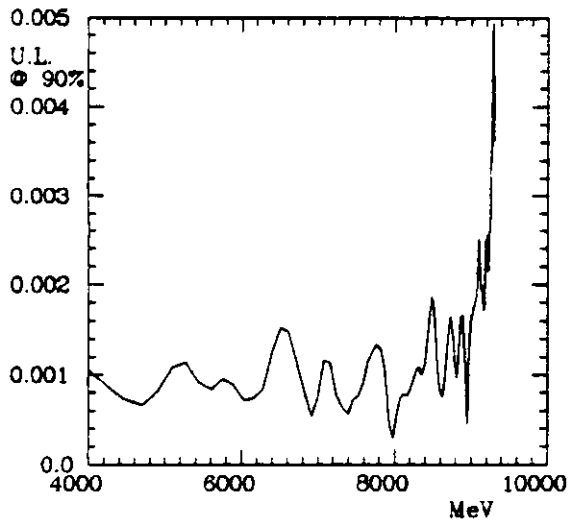


Figure 8: 90% upper limit as function of recoil mass,  $\Upsilon$

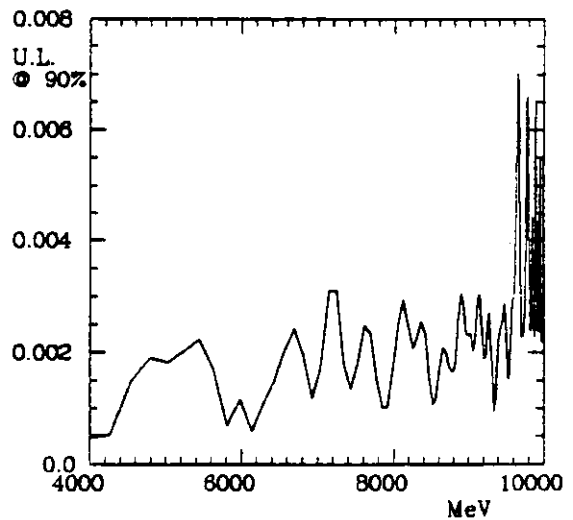


Figure 9: 90% upper limit as function of recoil mass,  $\Upsilon'$

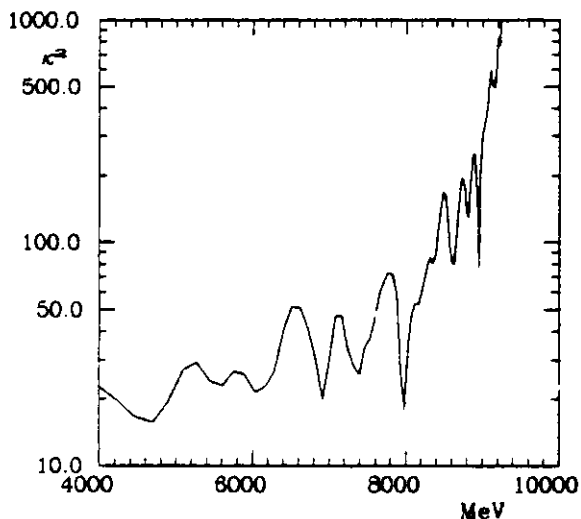


Figure 10: Lower limit  $\kappa^2$ ,  $\Upsilon$

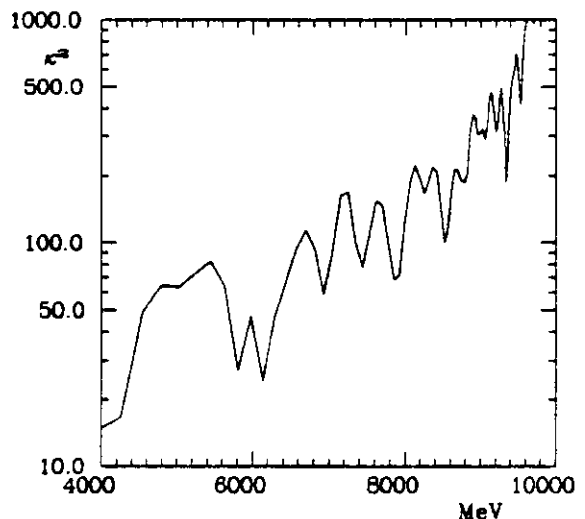


Figure 11: Lower limit  $\kappa^2$ ,  $\Upsilon'$

- the 3/1 ratio for  $\text{Higgs} \rightarrow c\bar{c}/\text{Higgs} \rightarrow \tau\bar{\tau}$  can be modified. Actually the  $\tau\bar{\tau}$  mode can become the dominant Higgs decay [22].

Therefore we can compute lower limits on an enhancement factor  $\kappa^2$  for  $\Upsilon \rightarrow \gamma\text{Higgs}$  in dependence on the Higgs decay couplings, with  $\kappa^2$  defined by

$$\text{BR}(\Upsilon \rightarrow \gamma\text{Higgs})_{2\text{doublets}} = \kappa^2 \text{BR}(\Upsilon \rightarrow \gamma\text{Higgs})_{1\text{doublets}}$$

and  $\text{BR}(\Upsilon \rightarrow \gamma\text{Higgs})_{1\text{doublet}}$  is the theoretical prediction from equation 3. This parameter  $\kappa^2$  is the square of the ratio of the vacuum expectation values of the two Higgs fields. We get lower limits on the enhancement factor  $\kappa^2$  as shown in figure 10 and 11 for  $\Upsilon$  and  $\Upsilon'$  for a 3/1 coupling of the Higgs to  $c$  quarks and  $\tau$  leptons. A different coupling would just rescale the y-axis (e.g. a 100% coupling to  $\tau\bar{\tau}$  would divide the numbers by 4).

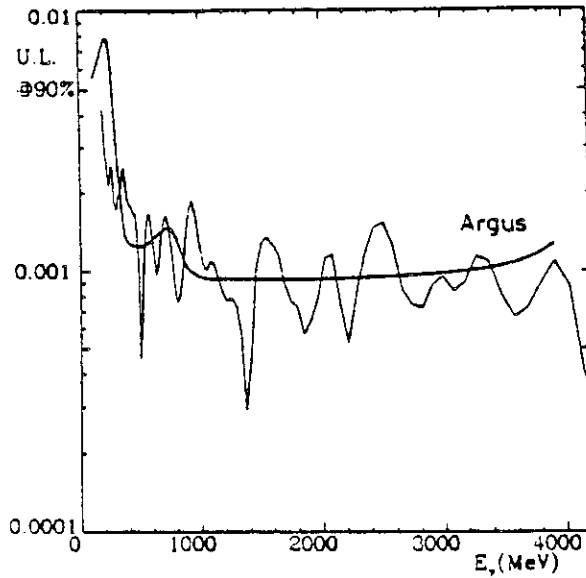


Figure 12: 90% upper limit on  $\Upsilon \rightarrow \gamma X \rightarrow \gamma \tau \bar{\tau}$  type final state

Since the lower limits on the enhancement factor are always greater than unity we cannot rule out a minimal Higgs but we present constraints on the ratio of vacuum expectation values for models with 2 complex Higgs doublets.

This search presents the first limits for  $\Upsilon' \rightarrow \gamma X \rightarrow \gamma \tau \bar{\tau}$  type final states. At the  $\Upsilon$ , the results are comparable to a previous measurement by ARGUS [25] for photon energies above 1 GeV and superior for smaller energies. In figure 12 we show an overlay of ARGUS and Crystal Ball results for the decay  $\Upsilon \rightarrow \gamma X \rightarrow \gamma \tau \bar{\tau}$ .

## 2.3 Tau Lepton Decays

In this subsection we will first discuss the properties of the heaviest known lepton, the  $\tau$ . In a second part we will present a search for unconventional  $\tau$  decays motivated by the concept of compositeness of quarks and leptons.

### 2.3.1 Conventional $\tau$ decays

The discovery of the  $\tau$  lepton in 1975 by Mark I at SPEAR [7] provided the first direct indication for the existence of a third family of leptons. Many experiments studied the  $\tau$  lepton in detail and were able to prove that the  $\tau$  lepton is a heavy 'carbon copy' of electron and muon (and not some exotic object). The  $\tau$  lepton has its own neutrino and the upper limit on the  $\tau$  neutrino is  $M_{\nu_\tau} < 70 \text{ MeV}$  [26].

The decay modes of the  $\tau$  lepton can be calculated in the standard model. The  $\tau$  decays via the charged weak current into its neutrino under emission of a  $W$  boson (figure 13) which then turns into leptons or hadrons (figure 14).

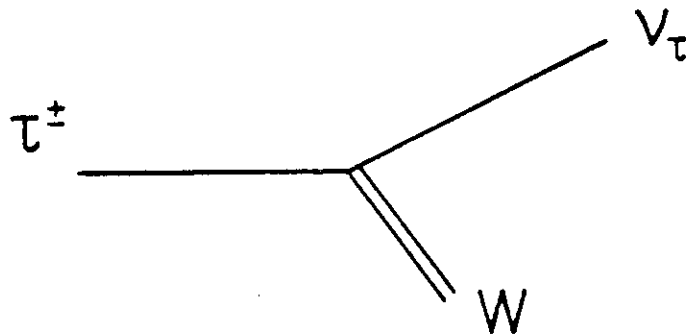


Figure 13: Feynman diagram for  $\tau$  decay

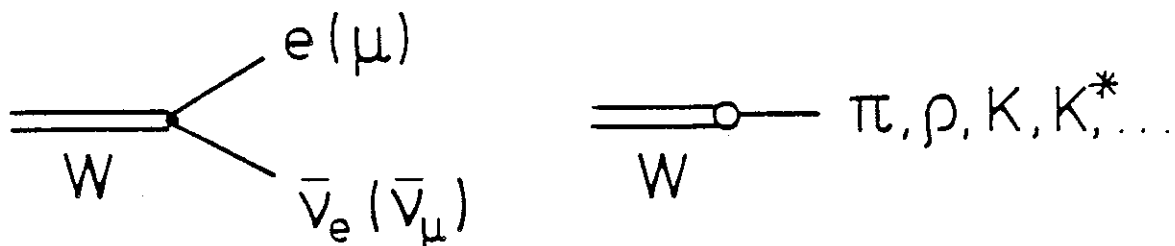


Figure 14: Feynman diagram for subsequent  $W$  decay

A rough estimate of the relative branching fractions can be obtained by neglecting mass effects and Cabibbo suppressed decays involving strange quarks. Due to color hadronic decays should be 3 times more abundant than leptonic final states. Since 2 leptons are accessible we get a branching fraction of 20% for  $\tau \rightarrow e \bar{\nu}_e \nu_\tau$  and  $\tau \rightarrow \mu \bar{\nu}_\mu \nu_\tau$  decays and 60% for hadronic decays.

Channel	Branching fraction %	
	1 charged particle	3 charged particles
$\tau \rightarrow e \bar{\nu}_e \nu_\tau$	17.9	-
$\tau \rightarrow \mu \bar{\nu}_\mu \nu_\tau$	17.4	-
$\tau \rightarrow \pi \nu_\tau$	10.9	-
$\tau \rightarrow K \nu_\tau$	0.7	-
$\tau \rightarrow (\pi\pi)^- \nu_\tau$	22.0	-
$\tau \rightarrow (K\pi)^- \nu_\tau$	1.1	0.3
$\tau \rightarrow (4\pi)^- \nu_\tau$	1.0	4.9
sum	71.0	5.2
$\tau \rightarrow (3\pi)^- \nu_\tau$	< x	x
$\tau \rightarrow (5\pi)^- \nu_\tau$	< 0.12	y
$\tau \rightarrow (6\pi)^- \nu_\tau$	< 0.21	< 0.64
$\tau \rightarrow (K\bar{K})^- \nu_\tau$	< 1.2	< 0.6
$\tau \rightarrow (K\bar{K}\pi)^- \nu_\tau$	< 1.29 z	z
$\tau \rightarrow (K\pi\pi)^- \nu_\tau$	< 4/5 w	w

Table 2: Known  $\tau$  decay modes with calculated branching fractions using  $\text{BR}(\tau \rightarrow e \bar{\nu}_e \nu_\tau) = 17.9\%$ .

The widths for the leptonic modes can be calculated precisely within the standard model. They can be converted into branching ratios using the measured tau lifetime [27]. Calculations of hadronic final states are more involved and need additional experimental input, e.g. to determine  $\tau \rightarrow \pi \nu_\tau$  the pion decay constant and the Cabibbo angle is needed. A detailed treatment of these calculations can be found in reference [28].

A summary of all known  $\tau$  decay modes and their branching fractions is given in table 2 (from reference [29]). The calculations for the reactions in the lower part of table 2 have considerable theoretical uncertainties. Limits on the unknown parameters (x, y, z, w) can be derived from isospin considerations as well as experimental data.

Comparing theoretical and experimental branching fractions yields indications for yet unknown  $\tau$  decay modes into 1 charged particle and neutrals. Inclusive measurements of the branching fraction into 1 charged particle yields [20]

$$B_1 = (86.5 \pm 0.3)\%$$

whereas from table 2 we get a range (depending on the values for x, y, z, w) of

$$B_1 = (74.2 - 81.0)\%$$

The missing decay modes constitute the last open problem in  $\tau$  decays.

### 2.3.2 Unconventional $\tau$ decays

It has been argued that the Glashow Weinberg Salam model for electroweak interactions is probably not the fundamental but rather an effective low energy theory. This is

supported by the multitude of free parameters (number of families, Yukawa couplings, Weinberg angle ...) and by the rich spectrum of the fundamental leptons and quarks. In analogy to the situation in the early 1960s, where the large number of elementary particles led to the introduction of the quark model one solution is a possible substructure of leptons and quarks. Composite models could be realized by the existence of so called preons, combinations of which would explain the known particle spectrum. An important parameter of these models is the relevant mass scale at which new phenomena will show up.

Important consequences of compositeness are various predictions for processes which are strictly forbidden in the standard model as well as corrections to parameters, like  $\rho = M_W^2 / M_Z^2 \cos^2 \Theta_W$ .

In general the corrections to these parameters, however, are extremely small [30].

One class of predicted reactions are inter-family transitions such as  $\mu \rightarrow e\gamma$ ,  $\tau \rightarrow e\gamma$ , ... Buchmüller [30] finds

$$\Lambda = \left( \frac{3 \times 2^{10} \pi^3 \alpha}{8 \text{BR}(l_i \rightarrow l_j \gamma)} \right)^{\frac{1}{4}} \left( \frac{v}{M_i} \right)^{\frac{1}{2}} v$$

where  $l_j$  denotes a lepton of mass  $M_j$  and  $v$  is the usual vacuum expectation value of the Higgs field ( $v \approx 249 \text{ GeV}$ ).

Experimental limits on  $\mu \rightarrow e \gamma$  yield a very high value of  $\Lambda \approx 10^4 \text{ TeV}$ , which on first sight renders a search for  $\tau \rightarrow e\gamma$  useless, since the resulting  $\Lambda$  will be much lower. The reaction  $\mu \rightarrow e\gamma$  however could be strictly forbidden by a yet unknown conserved quantum number which would have different values for  $\mu$  and  $e$ , but the same value for  $e$  and  $\tau$ . Therefore our experimental limit of (for details see chapter 6)

$$\text{BR}(\tau \rightarrow e\gamma) < 3.4 \times 10^{-4}$$

(at 90% confidence level) which can be converted into

$$\Lambda > 65 \text{ TeV}$$

adds useful information to composite model theories.

The process  $\tau \rightarrow e\pi^0$  could proceed as in figure 15 and could thus be used to give lower limits on the mass of the exchanged object X. The mass of X would be of the order  $\Lambda$ [31]. Unfortunately no detailed theoretical work has been devoted to this problem up to now [32]. There is, however, some structural similarity of this reaction to the decay  $K^0 \rightarrow e\mu$  which already has been analyzed [30].

The upper limits on decays of the type  $\tau \rightarrow e\gamma$  and  $\tau \rightarrow e\pi^0$  are well below previous results by the MARK II collaboration [33], in particular for the  $e\pi^0$  final state.

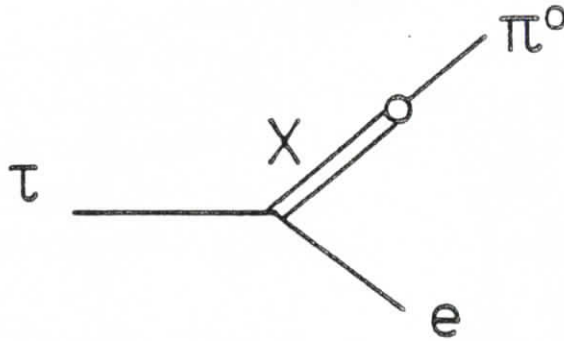


Figure 15: Feynman diagram for  $\tau \rightarrow e \pi^0$

### 3 Experimental Layout

#### 3.1 DORIS II

The data used for this analysis were taken at the DORIS II storage ring at DESY during 1983 and 1984. Initially DORIS was designed as a double ring storage ring (DORIS stands for DOppeL RIng Speicher) to study electron electron collisions at center of mass (CMS) energies up to about 7 GeV. With the discovery of the  $\Upsilon$  resonance at a fixed target experiment [5] a more careful <sup>2</sup> study at an  $e^+e^-$  collider required DORIS to be used as a single ring device with CMS energies up to 10 GeV. It was rebuilt in 1981/82 in order to lower the power consumption and to increase the available CMS energies up to 11 GeV. This opened the possibility to study the whole  $\Upsilon$  family up to open b threshold (just below the  $\Upsilon'''$  the CMS energy is high enough to produce mesons containing b and  $\bar{b}$  quark respectively). Moreover the luminosity was increased by an order of magnitude by inserting mini- $\beta$ -quadrupole magnets near the interaction regions [34].

The energy resolution of an  $e^+e^-$  storage ring is governed by synchrotron radiation. In the arcs of the machine electrons (in the following electrons mean  $e^+$  as well as  $e^-$ ) radiate photons. The total energy loss  $U$  per revolution amounts to

$$U = \frac{4\pi}{3} \frac{r_e}{(mc^2)^3} \frac{E_0^4}{\rho}$$

where  $r_e$  and  $m$  are the classical electron radius and the electron mass,  $E_0$  is the beam energy and  $\rho$  the magnetic radius of the bending magnets. The parameters of DORIS result in an average energy loss of 4 MeV per beam. This energy loss is compensated by high frequency transmitters. The quantum fluctuations in this loss however yield an energy spread of 4 MeV per beam [35]. Moreover synchrotron radiation is of potential danger to the Crystal Ball detector, since the lightoutput of the NaI(Tl) crystals can be degraded. No such degradation has been seen up to now [36]. On the other hand

<sup>2</sup>The mass resolution of an  $e^+e^-$  machine (limited by synchrotron radiation, see below) is orders of magnitude better than at a fixed target experiment.

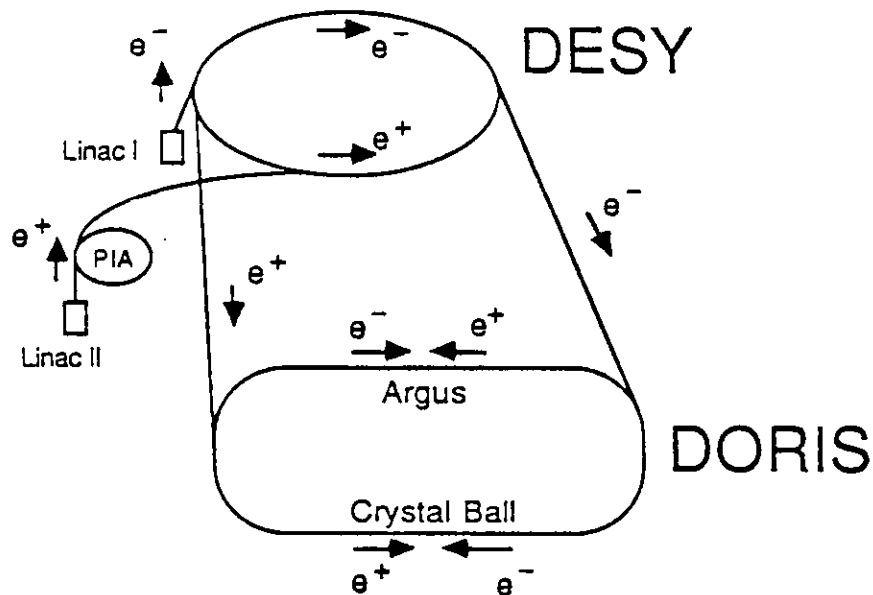


Figure 16: Layout of Doris and peripherals

the synchrotron radiation has the positive effect of building up a polarization of the beams as high as 80% at the  $\Upsilon'$  (no such polarization is observed at the  $\Upsilon$  due to depolarizing resonances of the machine [37]). This is known as the Sokolov-Ternov effect [38]. Destroying the polarization by means of an adjustable RF frequency transmitter provides a very precise measurement of the beam energy ( $\pm 0.2$  MeV) which in turn can be used for a precise measurement of the  $\Upsilon'$  mass [39].

The whole setup to provide colliding  $e^+e^-$  beams of about 5 GeV each is sketched in figure 16. The electrons produced by emission off a heated surface are accelerated with a linear accelerator (LINAC I) to an energy of 60 MeV. They are then injected into a synchrotron (DESY) which accelerates them up to the final beam energy. The positrons are produced via pair production following bremsstrahlung: electrons accelerated by LINAC II up to 240 MeV impinge onto a tungsten target where the bremsstrahlung and pair production takes place. The positrons are focused, 'cooled down'<sup>3</sup> and accumulated in a small ring PIA (this stands for Positron Injection Accumulator). These positrons are then injected into the synchrotron. Once the electrons and positrons have reached their final energy they are transferred to DORIS II, contained in 2 separate bunches of about  $10^{11}$  particles each. The bunch size is about 1mm in the plane of the ring and much less than that in the vertical dimension. In the beam direction the bunch is gaussian distributed with  $\sigma_z \approx 2.1$  cm. This in turn yields a gaussian vertex distribution of  $\approx 1.5$  cm. These 2 bunches (rotating clockwise and anticlockwise respectively) collide

<sup>3</sup>On leaving the converter the positrons have a high momentum spread. In a small ring the momentum spectrum can be narrowed via emission of synchrotron radiation. In analogy to thermodynamics this is called cooling.

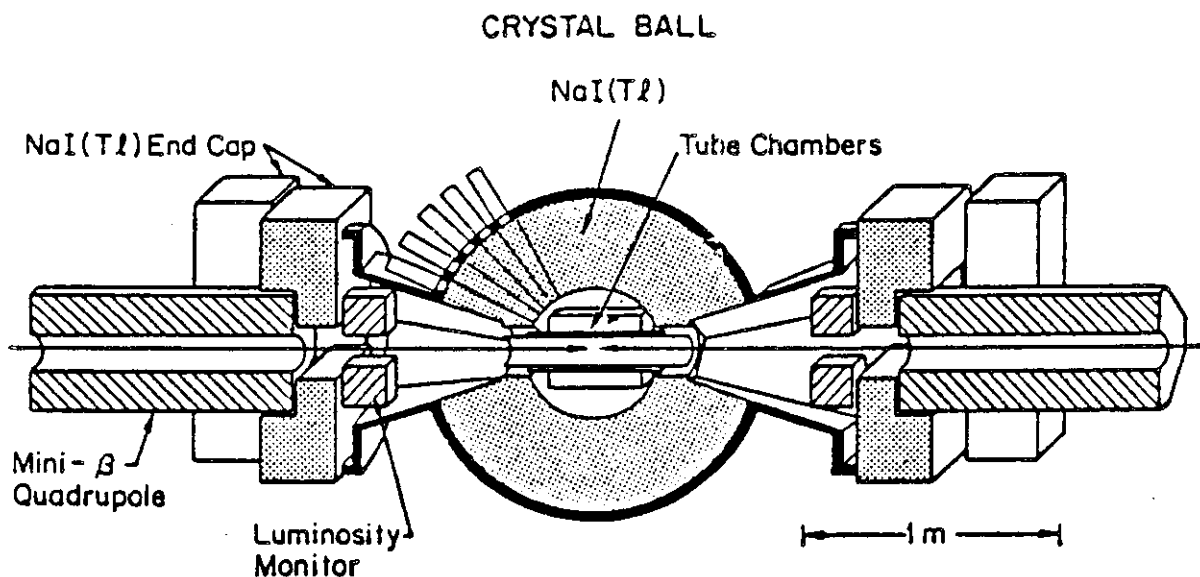


Figure 17: Layout of the Crystal Ball detector

every microsecond at 2 interaction regions: The south hall is occupied by ARGUS [40], a magnetic general purpose detector, the north hall by Crystal Ball.

### 3.2 The Crystal Ball Detector

The Crystal Ball is designed as an electromagnetic calorimeter with very good energy resolution. To this end one sacrifices the advantages of a magnetic field which would give better particle identification <sup>4</sup>. Surrounding the beampipe is a system of tube chambers which allows charged particle tagging and gives directional information for charged particles. The NaI(Tl) endcap crystals together with a small angle luminosity detector and a time of flight (TOF) system provide additional information. Figure 17 shows the general layout of the detector relative to the beamline. The whole device is located in a temperature and humidity controlled dryhouse, since NaI(Tl) is extremely hygroscopic. In the following we describe the various components, more details can be found in references [41] [42].

#### 3.2.1 Main Ball

The main detector is a spherical array of NaI(Tl) crystals. NaI(Tl) is very well suited for electromagnetic calorimetry, since the amount of scintillation light created in the crystals is to a very good approximation linearly proportional to the energy deposited [43]. The Thallium doping (0.1%) improves the scintillation properties of NaI such that one roughly gets one photon per 25eV deposited energy. The energy resolution achieved

<sup>4</sup>For details on particle identification see appendix A

for electrons and photons can be described as

$$\frac{\sigma_E}{E} = \frac{2.7\%}{\left(\frac{E}{\text{GeV}}\right)^{0.25}}$$

The jargon used to characterize the geometry of this array of crystals is presented in figure 18 . We start off with an icosaedron (a 20 sided solid), each triangular surface being called a 'major triangle'. Dividing each of these into four triangles yields the 'minor triangles'. Each minor triangle is further divided into nine modules of triangular cross section (crystals). The axis of each of these modules points towards the interaction point. This process creates 720 crystals covering the whole  $4\pi$  solid angle. Leaving a hole for the entry and exit of the beampipe reduces the 720 crystals to 672. This results in a 93% coverage of the full solid angle.

Each of the two hemispheres contains 336 optically isolated crystals. This optical isolation is achieved by wrapping each individual crystal in paper and aluminized mylar foil [41]. Thus the basic geometry of the crystals is a truncated pyramid of triangular cross section. All the crystals together form a spherical shell of 10 and 26 inches inner and outer radius respectively. During the assembly every crystal was sanded and/or polished to achieve a uniform response to a  $^{137}\text{Cs}$  source placed along its axis (so called 'compensation'). Each crystal is 16 inch long corresponding to 15.7 radiation lengths and 1 nuclear absorption length. A photomultiplier sitting at the rear end converts the collected light into an electrical signal. The crystals of each hemisphere are stacked and sealed in a steel can for dryness and support. Those two hemispheres can be separated via a hydraulic mechanism to allow easy access to the inner components of the detector such as tubechambers and luminosity monitor. After closing the hemispheres there is still a gap of up to 8mm due to mechanical tolerances. This gap is accounted for in the simulation programs, for details see appendix B.

There is a mercator type display of the detector, called 'flat', used to illustrate the energy recorded in each crystal, see figure 19 . The numbers are crystal energies in MeV (in excess of 0.5 MeV).

### 3.2.2 Endcaps

NaI(Tl) crystals of hexagonal cross section are used to extend the solid angle coverage from 93% (main ball) to almost 98% of  $4\pi$ . 20 crystals with 3 to 9 radiation lengths surround the beampipe on each side. The energy measurement with these endcaps is clearly degraded in comparison to the main ball. They can however be used to veto events which record a huge amount of energy outside the main ball.

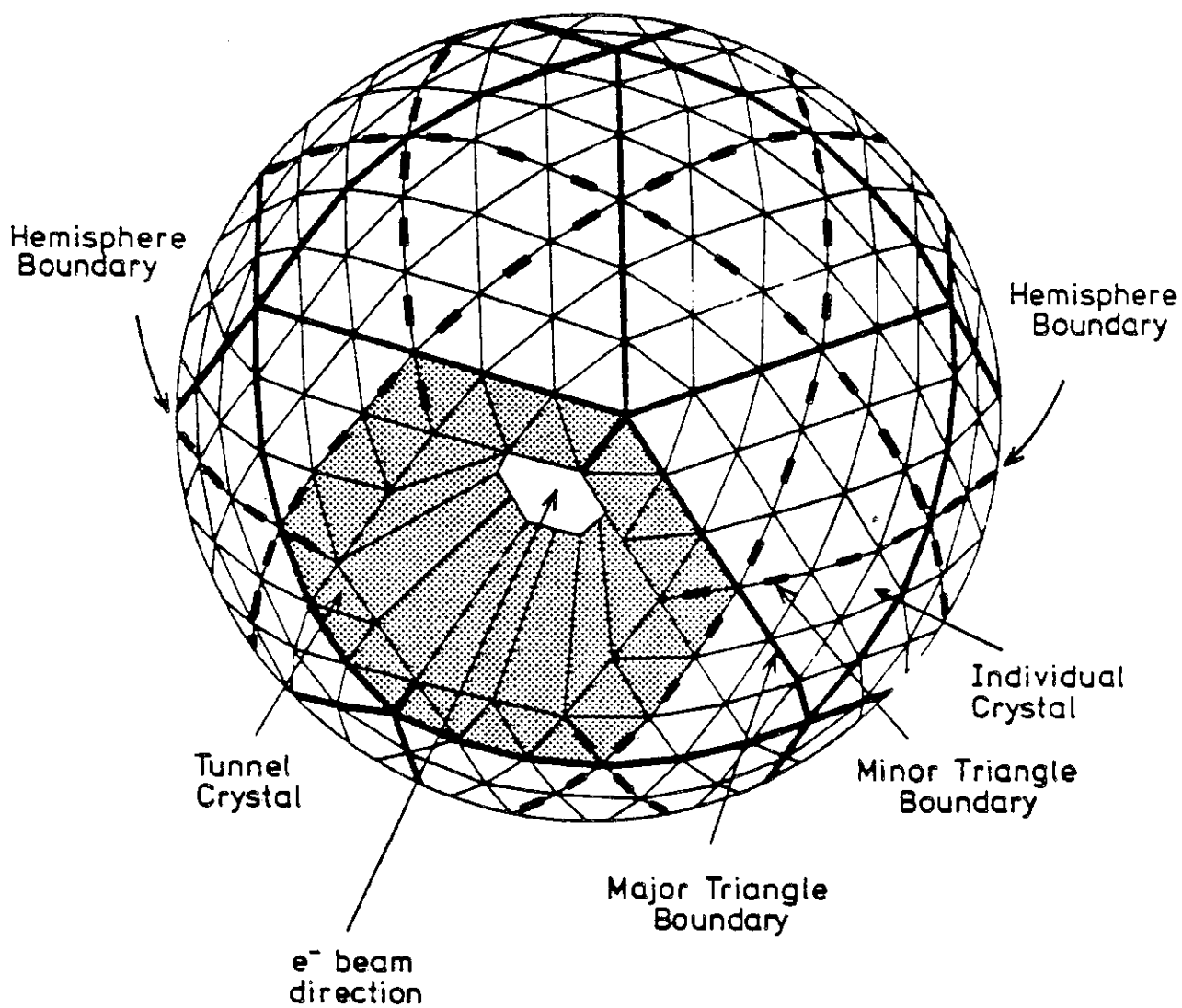


Figure 18: Jargon used for the various components

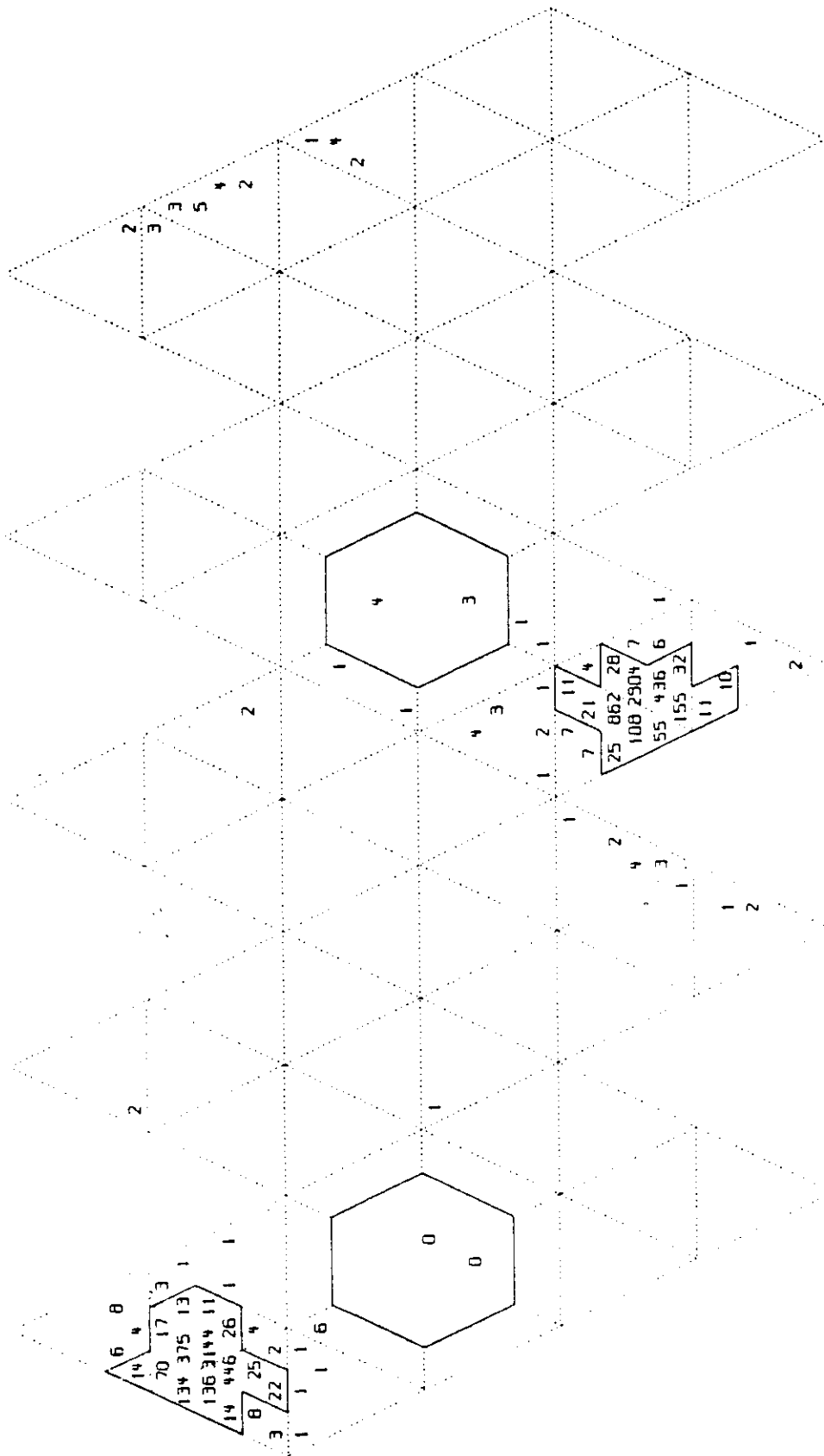


Figure 19: Event display of typical  $e^+e^- \rightarrow e^+e^-$  event

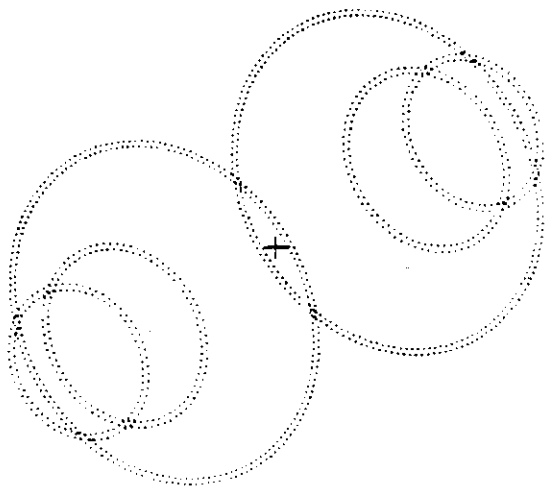


Figure 20: Tubechamber setup for 1983

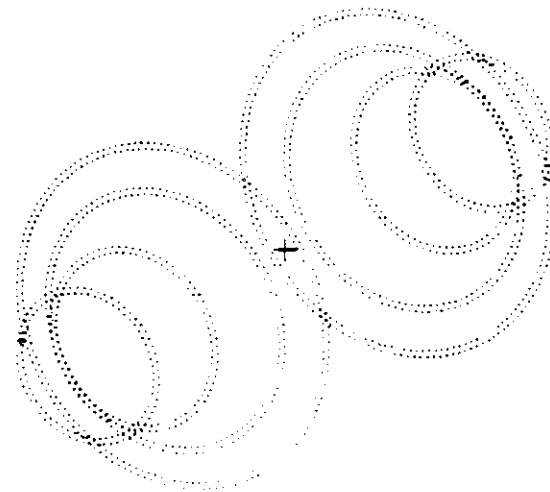


Figure 21: Tubechamber setup for 1984

### 3.2.3 Tubechambers

Information on the charge of a particle is supplied by a set of tubechambers mounted around the beampipe, see figure 17. It required 4 different configurations until an optimal performance was achieved. The two characteristic setups with 3(4) double layers of 64-160 tubes per layer used in 1983(84) are shown in figures 20 and 21. All tubes have the same diameter (5mm), but different lengths. The walls are aluminum (0.08mm thickness) and a resistive wire is used as signal wire. Charge division can then be used to get information about the position of the signal along the wire. The chambers are operated in a 'restricted proportional mode' with an Argon-CO<sub>2</sub> gas mixture (20%CO<sub>2</sub>, 1% methane and argon). In principle one could get much higher pulseheights independent of the primary ionization by using 'magic gas' (20% isobutane, 4% methylal, 0.25% freon and argon). This gas mixture however tends to disintegrate under radiation exposure and leads to organic growth on the wires. This in turn limits the operating voltage and therefore the efficiency. A small fraction of the data used for this analysis were taken with this gas mixture (first tubechamber configuration).

Amplifiers mounted at each end of the wire boost and shape the output pulse. From the ratio of pulse heights on both ends one can infer on the coordinate along the wire to within 1% - 2% of the chamber length. The resolution in the  $\phi$  coordinate is about  $1^\circ - 2^\circ$  (from the angular segmentation).

### 3.2.4 Time of Flight System

In order to get rid of cosmic ray background a time of flight system (TOF) covering 50% of the upper solid angle ( $2\pi$ ) is installed on the roof of the dryhouse (see figure 22). It consists of 94 plastic scintillator counters which have ADCs (Analog Digital Converters) and TDCs (Time to Digital Converters) attached at both ends. This provides both timing and directional information so that hits in the TOF can be correlated with

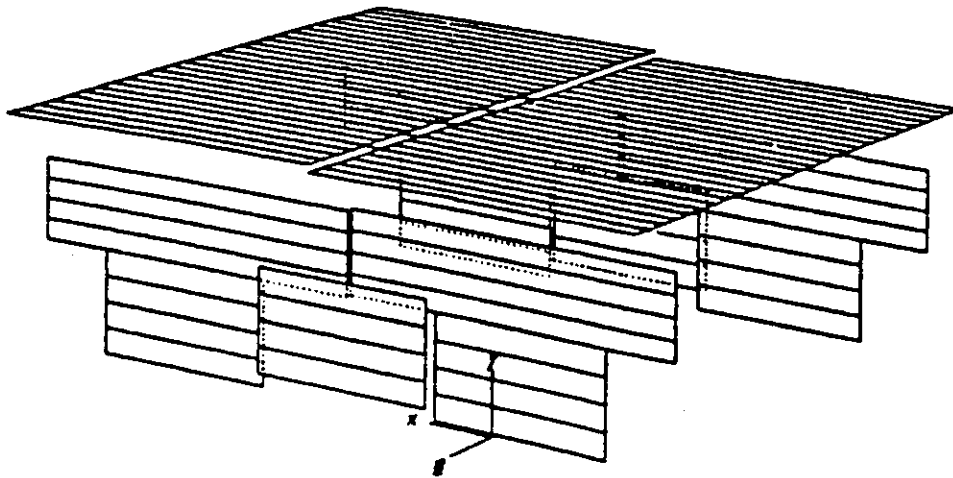


Figure 22: Time of Flight System

particles detected in the main detector. With an average distance from the interaction point to the TOF of about 3 meters a high energetic particle will need about 10ns. Since this is much more than the TDC timing resolution a clear separation between cosmics and annihilation events is possible.

In addition each of the 20 major triangles of the ball has a TDC as well as the full ball, the top and the bottom hemisphere.

### 3.2.5 Flasher system

A light pulser system is used to monitor the performance of the crystal light readout. To this end light from a Xenon flash lamp is distributed into the photomultipliers of each crystal with glass fibres. Moreover LEDs are mounted directly on the phototubes. This system is run at about 0.1Hz, to be compared to a typical event rate of 5 events per second.

### 3.2.6 Luminosity Monitor

In order to convert event rates into cross sections one needs the integrated luminosity collected by the experiment. This is accomplished using the well known Bhabha process ( $e^+e^- \rightarrow e^+e^-$  scattering) in two ways.

A small angle luminosity monitor system (see figure 23) is located at about  $8^\circ$  from the beampipe. It has a very high counting rate since the Bhabha cross section peaks towards the beamaxis. The P and C counters in the figure are scintillation counters defining the angular acceptance of the system. The S counters are lead- scintillator sandwich and provide a measure of the energy of the electrons and positrons. A logic connects the information of these counters such that a tilting of the beam cancels to first order. The luminosity is calculated by dividing the number of counts in the counterarms

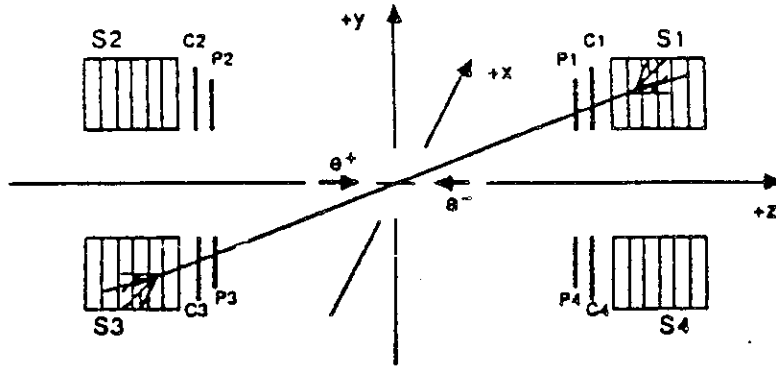


Figure 23: Small angle Luminosity Monitor

by the acceptance corrected Bhabha cross section (SAB) which is calculated using Monte Carlo simulation methods.

A second method to measure the luminosity uses the main detector itself to look for an  $e^+e^-$  pair scattered at large angles relative to the beam (large angle Bhabha, LAB). This measurement is more time consuming since the rates are lower and the analysis has to be done offline.

The precision of the SAB measurement suffers from the dead material (cables etc.) between interaction point and counters which is difficult to simulate. Therefore the final luminosity measurement is done using LAB because the acceptance is better known. The SAB luminosity on the other hand provides a quick online measurement on a run by run basis which is used to check the performance of the accelerator.

### 3.2.7 Electronics and Trigger

The signals from the crystal phototubes of the main ball and the endcaps are led to the controlroom together with signals from the tubechambers, TOF and SAB. The crystal signals are split to be used for integration as well as trigger purposes.

The trigger is based on the crystal information by requiring certain topological and total energy criteria. The group of nine crystals forming a 'minor triangle' (see figure 18) constitutes a useful geometrical unit. The phototube signals from the crystals of each minor triangle are summed to form an analog sum of nine ( $\Sigma_9$ ). The four minor triangle sums of a major triangle are also summed ( $\Sigma_{36}$ ). All  $\Sigma_9$  constitute the total energy  $E_{Total}$ . This sum does not include endcaps nor tunnels which are most susceptible to spurious beam related energy. Some of the triggers have a veto if the tunnel energy exceeds a certain threshold. The most important triggers for this analysis are given in table 3, for details see reference [44].

These triggers (besides  $E_{Total}$ ) require an event to possess certain spacial symmetries in order to suppress events originating from beam-gas, beam-wall interactions or cosmic rays. An annihilation event should fulfill approximate momentum balance. Charged

E TOTAL	$E_{\text{Total}}$ has to exceed 1700 MeV. This is 100% efficient for the $\tau \rightarrow e\gamma$ and $\tau \rightarrow e\pi^0$ search.
NIM TOPO	$E_{\text{Total}} \geq 800$ MeV, energy in top and bottom hemisphere $\geq 180$ MeV each. Vetoed if sum of energies in the tunnel exceeds 30 MeV.
TOPO 6	$E_{\text{Total}} \geq 980$ MeV, each of the 6 hemispheres must have at least one major triangle with $\sum_{36} \geq 150$ MeV.
TOPO 20	$E_{\text{Total}} \geq 770$ MeV, each of the 20 hemispheres must have at least one major triangle with $\sum_{36} \geq 150$ MeV.

Table 3: Trigger Criteria

particles do not deposit their full energy in the Crystal Ball detector, but virtually all of them are at least 'minimum ionizing', corresponding to an energy deposit of at least 150 MeV. The  $\tau$  leptons under study involve neutrinos which escape detection. It will however be seen later that the above triggers are still very efficient for reactions involving  $\tau$  lepton decays.

An additional trigger, the Doris Bunch Marker (DBM) trigger, is used to study beam related background. Every  $10^7$  bunch crossing (i.e. every 10sec) the whole detector is read out regardless of any of the above triggers being set or not. This trigger samples randomly the spurious background energy present in the interaction region. These events will be used later to correct computer simulated 'events' which of course do not account for this random background.

The integration of the crystal signals is done by two RC circuits per crystal where one circuit is a factor 20 less sensitive than the other. This increases the sensitivity for low energies. The more sensitive circuit is called 'low channel' and ranges from 0 to 330 MeV, the other one 'high channel' and covers the range up to 6500 MeV. If none of the trigger criteria is fulfilled the charge on the capacitors decays such that at the next beam crossing ( $1\mu\text{s}$  later) virtually no charge is left. If however one or more of the trigger criteria are satisfied the capacitor is isolated from the rest of the system. The voltage on the capacitor is then presented to a 13 bit ADC (50MHz) once at a time (controlled by computer), digitized and stored in a temporary buffer. After all the signals are digitized the information is read out by the online computer (PDP 11/55t). The tube chamber signals are digitized in an analogous manner (one channel) by a separate ADC at the same time as the crystals. On the online computer these signals are compressed by suppressing those which are virtually zero (less than 100 keV over pedestal). The SAB signals go directly into a logic and are scaled there. The

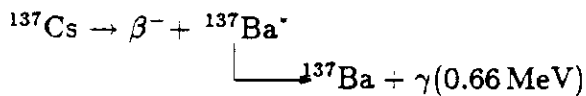
TOF signals are compressed on the hardware level by an 'intelligent' (Le Croy 2280) processor and sent to the online computer as well.

### 3.2.8 Calibration

In order to achieve the quoted resolution of

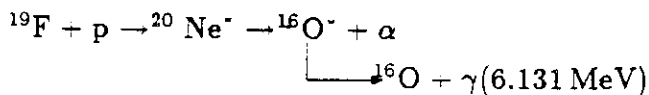
$$\frac{\sigma_E}{E} = \frac{2.7\%}{\left(\frac{E}{\text{GeV}}\right)^{0.25}}$$

the crystals have to be calibrated frequently (about every two weeks). The calibration procedure assumes that the relationship between deposited energy and light output is linear (see below for deviations from this linear behaviour). Since we have a low and a high channel we need a total of 4 constants per crystal (2 pedestals and 2 slopes). To get these constants we use a bootstrap approach. After taking pedestals (triggering on a pulser) a 0.1 mC  $^{137}\text{Cs}$  source is placed in the center of each hemisphere. The reaction



yields a well defined photon line. Such low energy photons tend to deposit all energy in one single crystal. Here we trigger on groups of nine crystals recording more than  $\frac{1}{2}E_\gamma$ , since this is the smallest hardware component which we can trigger on.

The next step is similar to the  $^{137}\text{Cs}$  calibration except that the photon energy is higher. A small Van de Graaff generator (450 keV protons impinging onto a fluorine target) is used to obtain gamma rays of about 6 MeV via the reaction



Now the photon energy is high enough that the shower is no longer contained in a single crystal. Therefore an iterative process has to be used starting from the  $^{137}\text{Cs}$  slopes. The crystal slopes are then adjusted such that the energy sum including neighboring crystals peaks at the nominal gamma ray energy.

The final step is to use beam energy electrons from the reaction  $e^+e^- \rightarrow e^+e^-$ . The energy of these particles again is spread over more than 1 crystal and an iterative procedure similar to the one for the Van de Graaff part has to be invoked. This time the peak energy has to coincide with the nominal beam energy. This results in the final calibration constants.

Up to now we assumed a linear relationship between energy deposit and electronic response. Looking at the invariant masses of  $\pi^0$  and  $\eta$  however we find that these are shifted low by approximately 2%. This can be corrected for by using a small empirical correction, for details see reference [45].

## 4 Datasamples and Production

### 4.1 Datasamples

The data used for this analysis were taken in Fall 1983 and during 1984. This sample corresponds to 222k  $\Upsilon$  resonance events ( $\int L dt \approx 22\text{pb}^{-1}$ ) and 193k  $\Upsilon'$  resonance decays ( $\int L dt \approx 61\text{pb}^{-1}$ ).

The calculation of the luminosity is already described (chapter 3.2.6) and the number of resonance decays is determined from the hadronic event sample. Details on the selection of hadronic events can be found elsewhere [46]. The main problem in calculating the number of resonance decays lies in the subtraction of the nonresonant background below the resonance (see figures 24). This can be done by comparing hadronic events

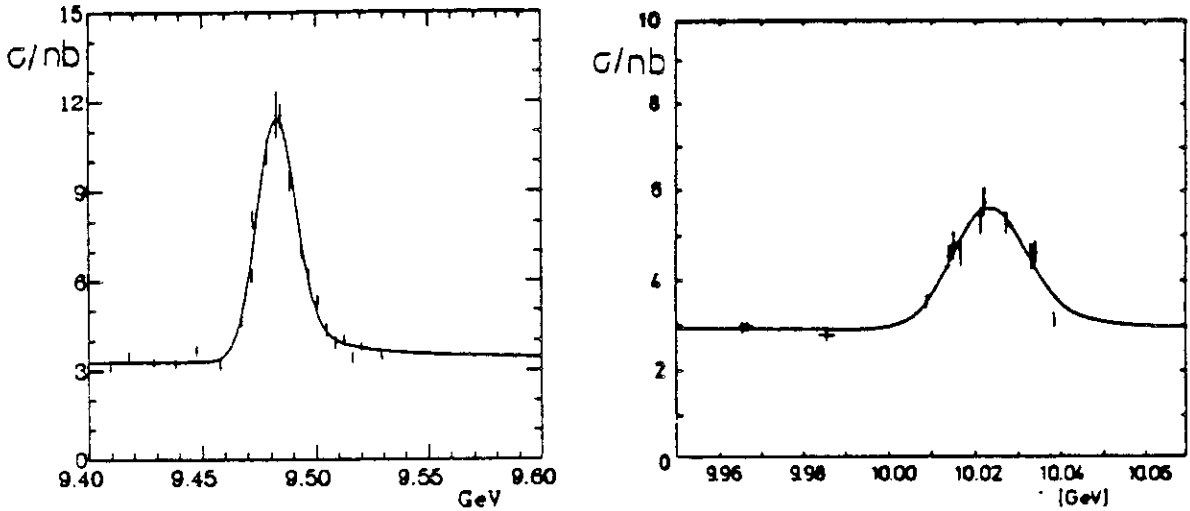


Figure 24: Hadronic cross section vs. CMS energy for  $\Upsilon$  and  $\Upsilon'$

taken on resonance to those taken off resonance, scaling the luminosities and taking into account the energy dependence of the cross section ( $\sim 1/S = 1/E_{\text{CMS}}^2$ ). The off resonance data were taken below the  $\Upsilon'$  at  $\sqrt{S} = 9.98$  GeV. So the number of observed  $\Upsilon'$  events<sup>5</sup> is

$$N_{\text{observed}}(\Upsilon') = N_{\sqrt{S}=10.023}^{\text{Hadrons}} - N_{\sqrt{S}=9.98}^{\text{Hadrons}} \frac{L_{10.023}}{L_{9.98}} \frac{(9.98)^2}{(10.023)^2} \frac{\epsilon_{\text{resonant}}}{\epsilon_{\text{cont}}}$$

with  $N_{\sqrt{S}=X}^{\text{Hadrons}}$  being the number of observed hadrons at CMS energy  $X$  in GeV,  $L_X$  being the accumulated luminosity.  $\epsilon_{\text{cont}}$  is the efficiency for detecting hadrons from continuum decays ( $e^+e^- \rightarrow 2$  quarks  $\rightarrow 2$  jets) and  $\epsilon_{\text{resonant}}$  is the efficiency for detecting hadrons from resonance ( $e^+e^- \rightarrow 3$  gluons  $\rightarrow 3$  jets) production. The number of resonance decays is related to  $N_{\text{observed}}$  by

$$N_{\text{resonant}}(\Upsilon') = \frac{N_{\text{observed}}(\Upsilon')}{\epsilon_{\text{resonant}}}$$

<sup>5</sup> Analogous for the  $\Upsilon$

Details about the determination of  $\epsilon_{\text{resonant}}$  and  $\epsilon_{\text{cont}}$  can be found in reference [46]. The corresponding numbers for the  $\Upsilon$  and  $\Upsilon'$  resonances are summarized in table 4.

We finally find that the error on the number of hadrons is entirely governed by the

	$\Upsilon$	$\Upsilon'$
$\int L dt$	$(22 \pm 1)pb^{-1}$	$(61 \pm 3)pb^{-1}$
$N_{\text{Hadrons}}$	$(222 \pm 16)k$	$(193 \pm 15)k$

Table 4: Luminosities and number of resonance decays for  $\Upsilon$  and  $\Upsilon'$

error of  $\epsilon_{\text{resonant}}/\epsilon_{\text{cont}}$ . These numbers depend on the simulation of the quark and gluon fragmentation in the processes  $e^+e^- \rightarrow 2 \text{ quarks} \rightarrow 2 \text{ jets}$  and  $e^+e^- \rightarrow \Upsilon$  or  $\Upsilon' \rightarrow 3 \text{ gluons} \rightarrow 3 \text{ jets}$  as well as the simulation of the detector response.

## 4.2 Offline Production

The purpose of the so called 'production' is to convert the raw information (ADC and TDC counts recorded on tape) into meaningful quantities (energies, pulseheights, timing information) and to attempt a preliminary identification of particles. The standard procedure described below consists of 6 steps.

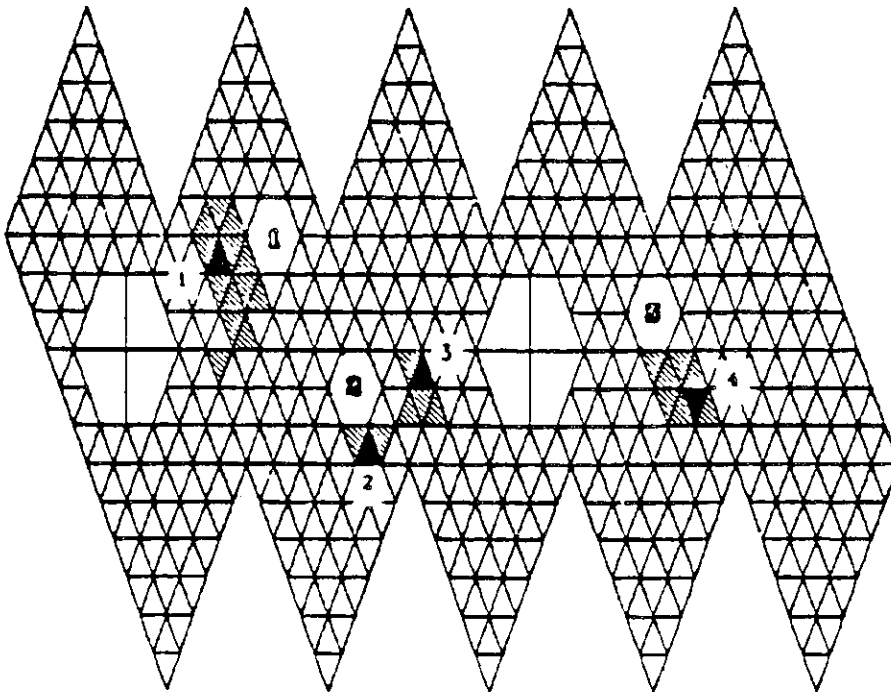
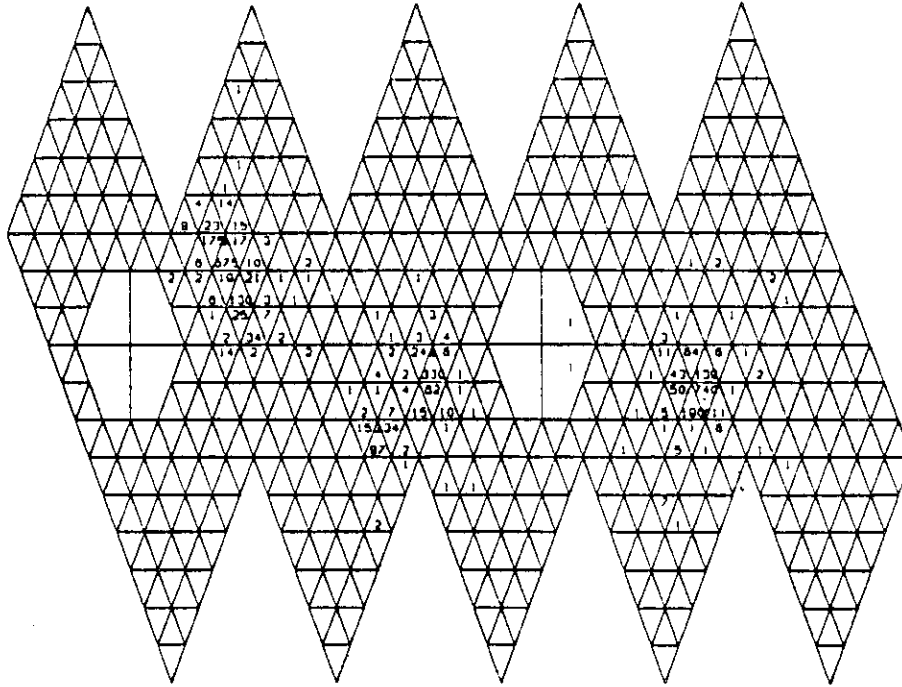
First the 'ENERGY' step converts raw ADC counts of the crystals into energies using the calibration (pedestals and slopes, see chapter 3.2.8). The low channel saturates at 7000 counts. This corresponds to 350 counts in the high channel due to the factor 20 difference in sensitivity of both channels, see chapter 3.2.7. Therefore:

$$E_{\text{Crystal}} = \begin{cases} (C_{\text{HighChannel}} - P_{\text{HC}}) \times \text{Slope}_{\text{HC}} & \text{if } C_{\text{HighChannel}} > 350 \\ (C_{\text{LowChannel}} - P_{\text{LC}}) \times \text{Slope}_{\text{LC}} & \text{if } C_{\text{HighChannel}} \leq 350 \end{cases}$$

where C denotes the number of ADC counts, P the pedestal and Slope the slope for this individual crystal.

A second step, 'CONREG', tries to identify energy clusters within the detector by searching for groups of crystals ( $E_{\text{Crystal}} \geq 10 \text{ MeV}$ ) which form a contiguous set called connected region. A crystal belongs to a contiguous set if it shares a vertex or a face with an other crystal of this set. Figure 25 shows an event with connected regions indicated.

These connected regions however might contain energy contributions from various nearby particles. Therefore an empirical algorithm called 'BUMPS' looks for local maxima in the energy distribution of each connected region. Based on Monte Carlo studies it tries to distinguish between statistical fluctuations and maxima caused by particles. First the highest energy crystal is labelled a bump and the 3 nearest neighbors are associated with it (see figure 26 for definition of these 3 crystals).  $E_{\text{Bump}}$  is the energy sum of the bump module and these 3 neighbors. Additional crystals within this



Connected regions shaded (  ) and numbered in **openface**.  
 Bump modules blackened (  ) and numbered in **boldface**.

Figure 25: Event display indicating connected regions and bump modules

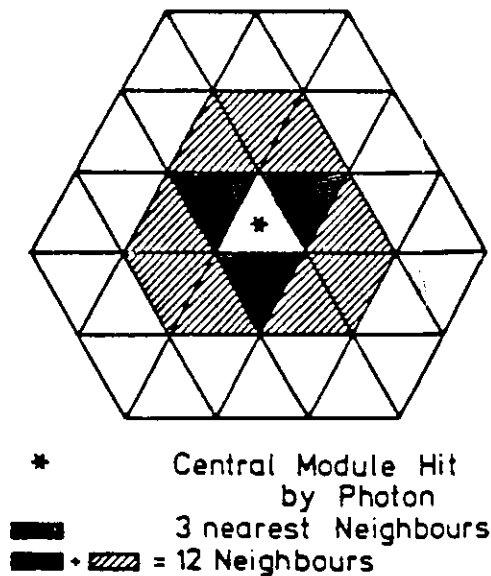


Figure 26: Group of neighbor crystals, indicated is the center crystal and outlined are the 3 nearest neighbors.

connected region are associated with this bump, if

$$E_{\text{Crystal}} < E_{\text{Bump}} \times 0.72e^{-9.4(1-\cos\Theta)} \text{ and } 15^\circ \leq \Theta < 45^\circ$$

or

$$\Theta < 15^\circ$$

where  $\Theta$  is the angle between the centers of the bump module and the crystal under investigation.

The unassociated crystal with the highest energy is called the next bump and the procedure is repeated until all crystals in the connected region are distributed. The dark shaded crystals in figure 25 represent bump modules. Each bump is considered to represent a particle in the detector.

In a fourth analysis step, 'CHGTKS', the tubechamber information is used to distinguish between charged and neutral particles and to improve the directional information for charged particles. First the raw tubechamber information (pulseheights at each end of a tube) is converted into  $\phi$  and  $z$  coordinates ( $z$  from the ratio of pulse heights at each end). Then a searching algorithm tries to construct trajectories from the tubechamber information alone by fitting hits to a straight line. These trajectories are required to originate from the beam line ( $x=y=0$ ) and a  $z$ -vertex of  $-11\text{cm} \leq z \leq 11\text{cm}$ . The later requirement is very loose since the vertex is gaussian distributed with width 1.5 cm, see chapter 3.1. If there are at least 3 hits which can be fit this is called an 'IR' track, since it supposedly originates from the interaction region. IR tracks pointing to a bump module are then associated with this bump and the particle direction from the chambers is used. The remaining hits in the chamber are used to tag bumps as charged. Looking through the bumps a small window in  $\phi$  and  $z$  is used to search for

hits. If there are at least 2 hits in this window the bump is called charged (the direction is determined by the center of the bump module).

In the so called 'ESORT' step final energy assignments are made for the bumps. A standard method for estimating the energy deposited by a track is the energy sum of the bump and its 12 surrounding neighbors,  $\sum_{13}$  (see figure 26), corrected for two effects. First there will be some energy leaking out of  $\sum_{13}$ . It is found from Bhabha events to be 2.2%<sup>6</sup>, to first order independent of energy due to the pyramidal geometry of the detector. Secondly the energy fraction contained in  $\sum_{13}$  will depend on the particles entry point into the crystal. Particles entering near a crystal border will loose more energy in the dead material (wrapping etc.) and the region outside the 12 neighbors than a particle entering in the center. This position correction 'PCORR' is based on the ratio of energy in the bump and  $\sum_{13}$  using empirical factors from Bhabha scattered beam energy electrons.

The direction for non 'IR' tracks is based on the expected shape of energy depositions for Monte Carlo photons. Each bump is subdivided into 16 submodules (for calculational purposes). Going through these 16 possible submodules the one which yields the least difference between expected and observed shape of energy deposition is found. The direction cosines of this submodule are then assigned to this bump.

Finally an attempt is made to disentangle the energies of overlapping energy depositions. Modules within  $\sum_{13}$  might belong to more than 1 shower, thus resulting in a double counting of energies. This can be corrected for by using empirical shower functions.

The final step is the time of flight (TOF) analysis. Hits in the roof TOF system are associated with particle trajectories. This timing information can be used to single out events originating from cosmic rays<sup>7</sup>. Details can be found in reference [50].

With all this information available a preselection (EOTAP) is done, using very loose cuts to single out events which are of no interest (e.g. very high energetic cosmic or extremely asymmetric beam-gas events). Using Monte Carlo methods it can be shown that only a negligible fraction of the events which are of interest in this work is rejected by this preselection. 10% of the events not passing any of the criteria are kept for checking purposes.

---

<sup>6</sup>In principle this could be accounted for in the calibration procedure.

<sup>7</sup>A cosmic ray passes first the TOF, then the interaction region thus having a negative timing. A particle coming from the vertex on the other hand has a positive timing.

## 5 The Decay $\Upsilon, \Upsilon' \rightarrow \gamma X \rightarrow \gamma \tau \bar{\tau}$

### 5.1 Analysis

#### 5.1.1 Introduction

The importance of finding a Higgs boson, one of the last missing building blocks of the standard model, has already been emphasized in chapter 2. The decay of the  $\Upsilon$  as well as the  $\Upsilon'$  into such a relatively heavy object by emission of a photon is the most sensible way to look for this particle if its mass should lie below the  $\Upsilon$  or  $\Upsilon'$ . Limits and predictions for the Higgs mass were already discussed in chapter 2.

There are two principle ways to perform this search. In the inclusive photon spectrum one looks for photons in a hadronic environment, without investigating detailed features of particles in the remainder of the event. On the other hand one can do an exclusive search by identifying all particles in the final state, thus providing not only information about the mass of the produced object (using the photon energy) but also about its decays. A serious drawback of the latter method is the lower detection efficiency since all particles have to be identified as unambiguously as possible. The inclusive approach would catch the decays

$$\text{Higgs} \rightarrow c\bar{c} \rightarrow \text{Hadrons, (c = charmed quark)}$$

the exclusive

$$\text{Higgs} \rightarrow \tau\bar{\tau}$$

For a model with one Higgs doublet these two decay rates scale roughly as 3:1, since the masses of  $c$  and  $\tau$  are roughly equal and the  $c\bar{c}$  mode has an extra factor 3 enhancement due to color.

Though the exclusive analysis will suffer from low detection efficiency it will have less uncertainties. The fragmentation of  $c$  quarks into hadrons is fairly model dependent, while the  $\tau$  decays are well known (see references [28] and [29]). Moreover a search for  $\gamma\tau\bar{\tau}$  final states has a wellknown background from conventional  $\tau$  pair production corrected for bremsstrahlung of the initial state electrons (see appendix B). This process can be used to check the selection procedure because the final photon spectrum has to match this QED prediction in shape and magnitude. The inclusive search on the other hand does not allow for such a check, since the observed photons come from all sorts of reactions ( $\Upsilon \rightarrow 3$  gluons,  $\gamma + 2$  gluons, continuum 2 quark production ...) , all of these reaction having considerable theoretical uncertainties (see reference [47]).

Finally there is the possibility, as already indicated in chapter 2 that the Higgs has a very large branching ratio into  $\tau$  leptons. There the  $\gamma\tau\bar{\tau}$  final state provides the only way to search for this particle.

The Crystal Ball being a nonmagnetic detector does not have a very good identification for charged nonshowering particles (see appendix A), but it does rather well for photons and electrons. Therefore in the following we will limit ourselves to decays of the  $\tau$  lepton into 1 charged particle and up to 2 neutrals. Fortunately about 87% of the  $\tau$  decays are of this type (see chapter 2). Moreover we will only keep events of the type  $\tau \rightarrow e \bar{\nu}_e \nu_\tau$  and  $\tau \rightarrow \mu \bar{\nu}_\mu \nu_\tau$  for this search. This results in a quite distinct signature (it is also the classical signature which led to the discovery of the  $\tau$  lepton, see reference [7]) with an electron on one (including some misidentified interacting pions, see appendix A) and a muon on the other side (including some misidentified minimum ionizing pions) besides a photon. The electron as well as the muon will tend to follow the direction of flight of the  $\tau$ , therefore the leptons will be well separated as long as the Higgs mass is not too low. This ensures a high detection efficiency since the particles will not tend to overlap.

### 5.1.2 Preselection

The input dataset for this selection is the output of EOTAP, as described in chapter 4.2. The data represent all of our 1984  $\Upsilon$  running as well as the Fall 1983/Spring 1984  $\Upsilon'$  data (for the corresponding luminosities see section 4.1). The purpose of the preselection (which will be the basis for the 3 following analyses) described below is to isolate clean events of low multiplicity. Cleanliness means that the amount of spurious beam related energy in the detector is small. Events resulting from a partial loss of beam tend to deposit a lot of energy preferentially in the endcaps and tunnel regions. A low multiplicity is required to separate  $\tau\bar{\tau}$  like events from 3 gluon or quark-antiquark type events. In addition there has to be a candidate for a photon and at least 2 charged particles (from both  $\tau$  leptons decaying into 1 charged particle each).

The cuts imposed and the fraction of events passing the subsequent cuts is given in table 5. 'Separated' in criterion 5 means that there is no other track ( $\sum_{13} \geq 100 \text{ MeV}$ ) within an angle  $\cos\Theta \geq 0.9$ . The above criteria also apply for the  $\Upsilon$  selection, except requiring at least 1 IR track instead of 2 charged tracks in criterion 4 and  $\sum_{13} \geq 100 \text{ MeV}$  in criterion 5.

In the following we will justify these cuts. Requiring at least 2 connected regions is fairly redundant but it rejects a lot of events at an early stage of the analysis thus saving CPU time. The cut on endcap energy can be understood by studying DBM triggered events. These events should only have random noise in them, see figure 27. The restriction on tracks within  $|\cos\Theta| \leq 0.84$  requires the tracks to be contained inside the main ball (not in tunnel crystals). This ensures a good energy measurement from  $\sum_{13}$  since tracks in tunnel crystals tend to loose energy leaking into the tunnels. The requirement of no track with  $\sum_{13} \geq 0.85 \times E_{\text{Beam}}$  is designed to reject most of the

cut	$\Upsilon$	$\Upsilon'$
Input from preselection	3625787	8824289
1 $\geq 2$ connected regions No endcap with $\sum_{\text{Energy}} \geq 100 \text{ MeV}$	82%	74%
within $ \cos \Theta  \leq 0.84$ :		
3 No track with $\sum_{13} \geq 0.85 \times E_{\text{Beam}}$	66%	67%
4 $\geq 2$ charged tracks $\sum_{13} \geq 100 \text{ MeV}$	26%	10%
5 $\geq 1$ gamma, neutral, $\sum_{13} \geq 50 \text{ MeV}$ , standard pattern cut, separated.	12%	4.2%
6 2-4 tracks ( $\sum_{13} \geq 100 \text{ MeV}$ ) besides gamma as defined in 5	4.8%	3.0%
Output	172486	263831

Table 5: Preselection criteria and transmission of subsequent cuts

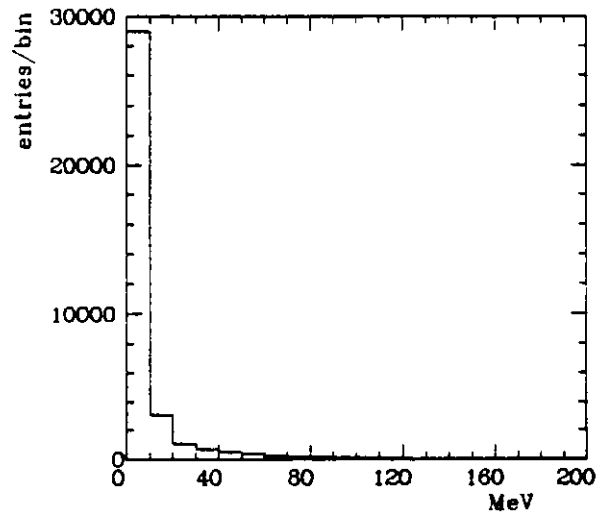


Figure 27: Energy in the endcaps for DBM events.

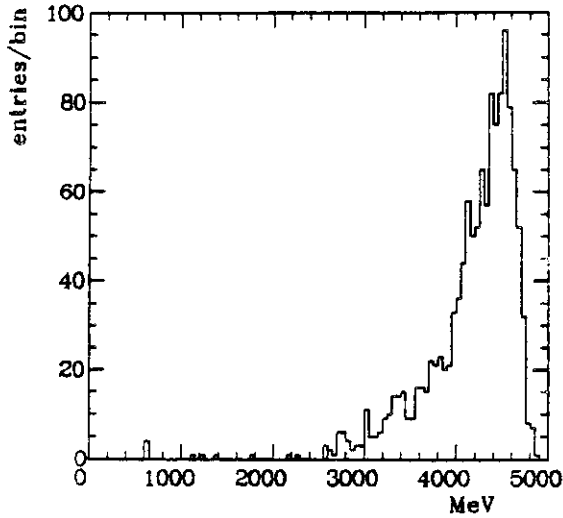


Figure 28: Track energies ( $\Sigma_{13}$ ) for Bhabha events

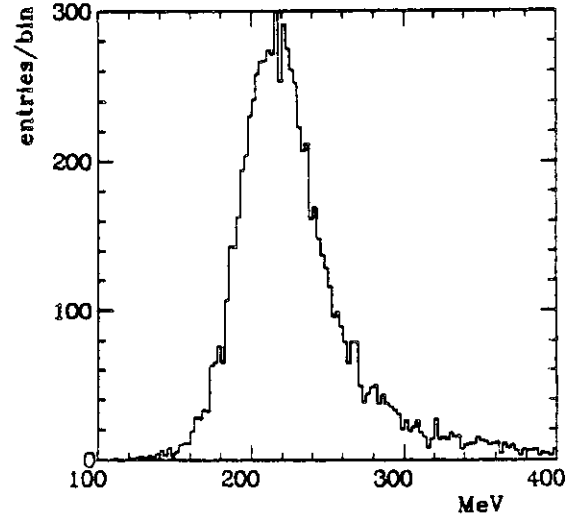


Figure 29: Track energies ( $\Sigma_{13}$ ) for minimum ionizing particles

$e^+e^-$  and  $e^+e^-\gamma$  final states from Bhabha scattering. This is demonstrated in figure 28. The electron energy spectrum is generated by a Monte Carlo generator for this process (reference [55]) with the behaviour of the final state particles in the detector being simulated (for details see appendix B).

The following cuts are designed to single out the low multiplicity topology. The energy distribution for minimum ionizing<sup>8</sup> particles in the Crystal Ball detector is shown in figure 29. Therefore the requirement of at least 2 charged particles with  $\Sigma_{13} \geq 100$  MeV is a reasonable choice to reject all-neutral events from 2 photon interactions which otherwise would represent a major background. In addition there has to be at least one well defined photon with more than 50 MeV energy being tagged as neutral by the tubechambers and passing a standard pattern cut. This pattern cut resulted from studies of Monte Carlo photons. One realizes that photons have a characteristic range in the variables  $\frac{E_4}{E_{13}}$  and  $\frac{E_1}{E_4}$ , whereas e.g. minimum ionizing particles occupy a different range in these variables (for a definition of  $E_1$ ,  $E_4$  and  $E_{13}$ , see figure 26, for details on pattern cuts appendix A). Allowing for 2-4 particles with  $\Sigma_{13} \geq 100$  MeV besides photons as defined above ensures the low multiplicity nature of the preselected sample.

### 5.1.3 Final Selection

In this final step we will try to select the events originating from the reaction under investigation. To this end we have to develop criteria which on the one hand suppress events from background processes as much as possible and on the other hand have a high efficiency for the ones we search for.

Therefore the preselected data are analyzed according to cuts designed to select

<sup>8</sup>An charged particle which has enough kinetic energy to transverse the ball will deposit at least this energy, for details see reference [49].

$\Upsilon, \Upsilon' \rightarrow \gamma X \rightarrow \gamma \tau \bar{\tau}$ . A first look at the total energy of the data at this stage compared to a Monte Carlo simulation of  $\tau$  pair production (see figures 30 and 31) shows that it is overwhelmed by non  $\gamma \tau \bar{\tau}$  type background. In figure 32 we display the same quantity for data where the  $e^+$  and  $e^-$  beams are separated using an electric field such that the two bunches miss each other at the interaction point by  $\approx 1\text{mm}$  in the vertical direction. This reveals that the background at low  $E_{\text{Total}}$  is not due to  $e^+e^-$  annihilation processes.

In the following we will show that this excess at low  $E_{\text{Total}}$  is probably caused by beam-wall (with wall we denote the beampipe) and/or beam-gas interactions. Beam-gas interactions are characterized by a zero vertex in the  $x - y$  plane (perpendicular to the beamaxis, in the following  $\rho = \sqrt{x^2 + y^2}$ ) and a flat distribution in the z-vertex (along the beam), for a comparison of the z-vertex for  $e^+e^-$  annihilation events and separated beam data see figures 33 and 34 <sup>9</sup>. Beam-wall events have in addition a nonzero  $\rho$  vertex and  $\rho$  will cluster at the radius of the beam pipe. Our standard software however (see chapter 4.2, charged tracking and tagging) can reconstruct a nonzero z-vertex, but assumes a zero  $\rho$  radius ('onaxis tracking'). Therefore a special routine was used ('TAGTRK') [50] which is able to perform offaxis tracking in a low multiplicity environment. It uses the tubechamber information ( $z$  and  $\phi$ ) together with the directional information from the energy depositions of two charged tracks. For a given  $z$  and  $\rho$  vertex we can extrapolate the 2 particle trajectories through the chambers. Varying the  $z$  and  $\rho$  vertices as well as the impact point of both particles within their bump modules we can optimize the correlation of tubechamber hits with particle trajectories. Figures 35, 36 and 37 show an offaxis (beam wall) event which is tracked onaxis (by standard software) and offaxis (by TAGTRK) together with an onaxis event.

With this tool at hand we can try to distinguish events from  $e^+e^-$  annihilation against events from beam-gas and/or beam-wall interactions. In figures 33, 34, 38 and 39 we show the  $z$  and  $\rho$  vertex distributions for colliding beam and separated beam data. A scatterplot of the total energy versus  $z$  and  $\rho$  vertex (figures 40 and 41) shows clearly that the accumulation at low total energy comes from beam-wall and beam-gas type events in the colliding beam sample. So it would be suggestive to cut in the  $z$  and  $\rho$  vertices to get rid of this sort of background reactions. The z-vertex distribution (figure 33) however shows a beam-gas contribution (flat distributed) under the  $e^+e^-$  annihilation part (gaussian distributed). Since this cannot be subtracted it would be helpful to have an additional variable which is sensitive to non  $e^+e^-$  annihilation events. Such a quantity is

$$E_T^2 = \sum_{i=1}^{720} E_i^2 \sin^2 \Theta_i$$

In figures 42, 43 and 44 we display  $E_T^2$  distributions for colliding and separated beam

<sup>9</sup>The spikes at 0cm correspond to the cases where no z-vertex can be reconstructed by the software.

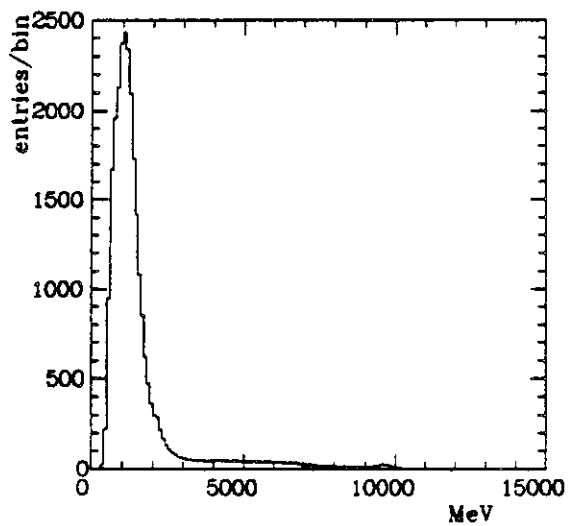


Figure 30: Total energy for data

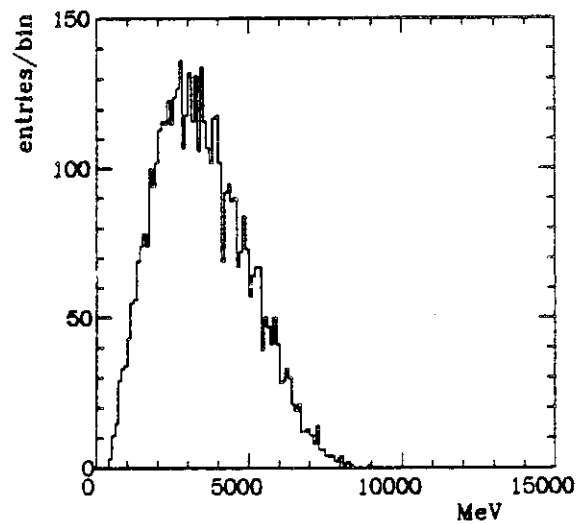


Figure 31: Total energy for Monte Carlo  $\gamma\tau\bar{\tau}$

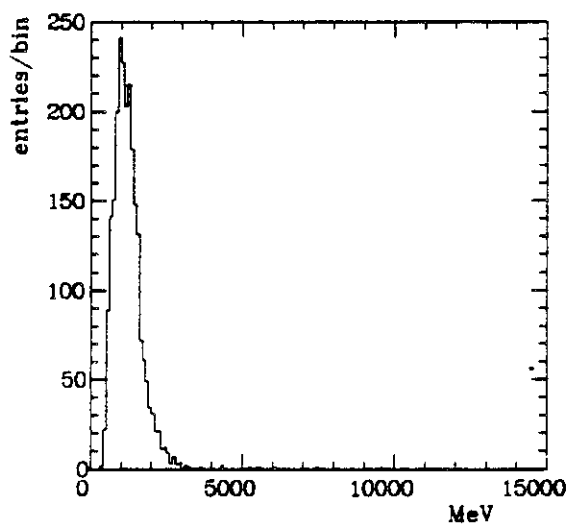


Figure 32: Total energy for separated beam data

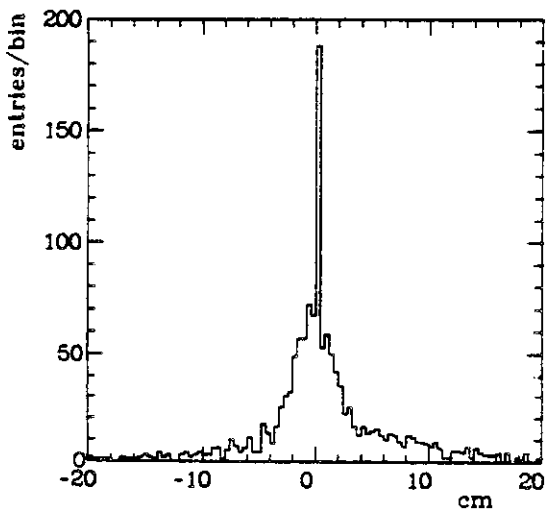


Figure 33: z vertex for colliding beam data

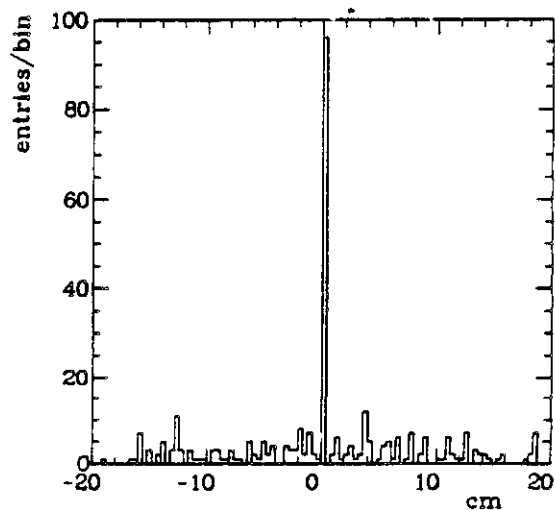


Figure 34: z vertex for separated beam data

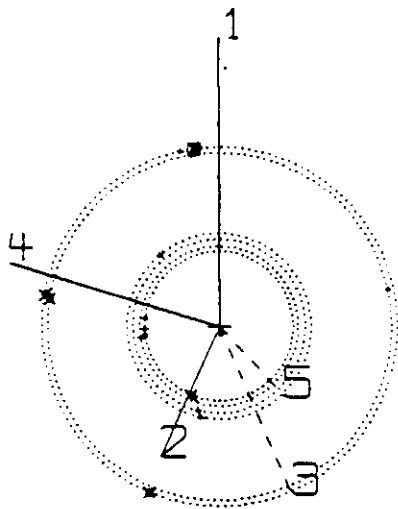


Figure 35: Offaxis event tracked onaxis

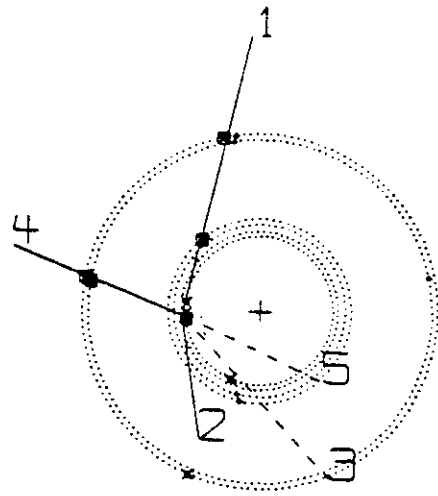


Figure 36: Offaxis event tracked offaxis

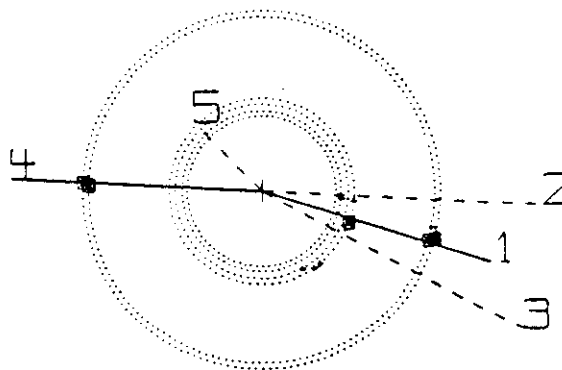


Figure 37: Onaxis event tracked onaxis

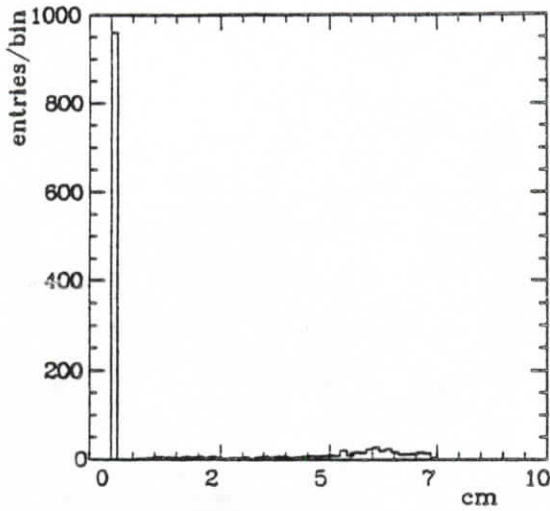


Figure 38:  $\rho$  vertex for colliding beam data

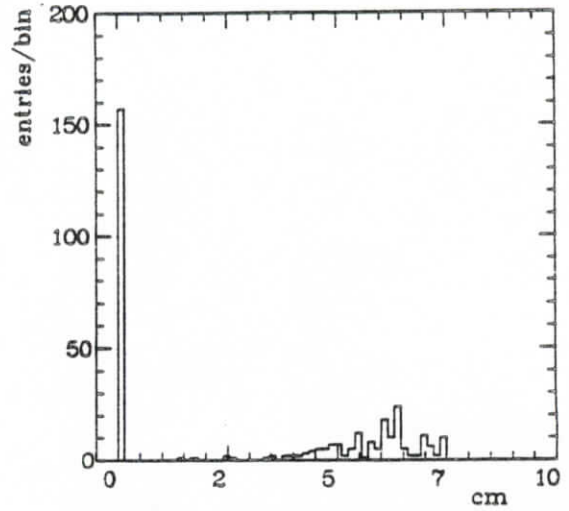


Figure 39:  $\rho$  vertex for separated beam data

data as well as Monte Carlo data. Scatterplots of  $E_T^2$  versus the  $z$  and  $\rho$  vertices show a high correlation between low  $E_T^2$  values and beam-gas/beam-wall type  $z$  and  $\rho$  vertices (see figures 45 and 46).

The criteria for the final selection together with the fraction of events passing the subsequent cuts are given in table 6. In the above cuts a neutral particle is identified as a  $\pi^0$  if

$$\text{Shower mass} \geq \frac{\sum_{13} \times 300}{4000} \text{ MeV and } 400 \text{ MeV} \leq \sum_{13} \leq 2000 \text{ MeV}$$

These criteria come from figures 93, 94 in appendix A. The chance for merging of the two photons into one deposition of energy is negligible for  $\sum_{13} \leq 400$  MeV and the algorithm cannot distinguish a photon from a  $\pi^0$  above  $\sum_{13} \geq 2000$  MeV.

In the following we will comment on these cuts. Requiring a total energy of less than 8 GeV is clearly justified by comparing figures 30 and 31. The data show some remnant enhancement at twice the beam energy. These events probably originate from  $e^+e^- \rightarrow e^+e^-(\gamma)$  or  $e^+e^- \rightarrow \gamma\gamma(\gamma)$ . Allowing for no track in the tunnel region (with  $\sum_{13} \geq 100$  MeV) ensures that there is no contribution from high multiplicity decays of the  $\tau$  lepton (e.g.  $\tau \rightarrow \pi\pi^0\pi^0$ ) which could pollute the photon spectrum with gammas from  $\pi^0$  decays. This is supplemented by requiring exactly 2 charged tracks with  $\sum_{13} \geq 150$  MeV. Cuts 4-7 define the final state topology. Cutting at  $\sum_{13} \geq 500$  MeV for the electron resembles a trade off between  $e/\pi$  separation and electron detection efficiency. The spectrum of electron energies from  $\tau$  decays recorded in the detector (see figure 47) would suggest as low a cut off as possible. For low electron energies however the background from pions passing the electron criteria starts to increase rapidly. This in turn pollutes the photon spectrum via  $\pi^0$ s from the most probable  $\tau$  decay,  $\tau^- \rightarrow \rho \nu_\tau \rightarrow \pi \pi^0 \nu_\tau$ . This would be a very serious background due to the high production rate for  $\tau$  pairs.

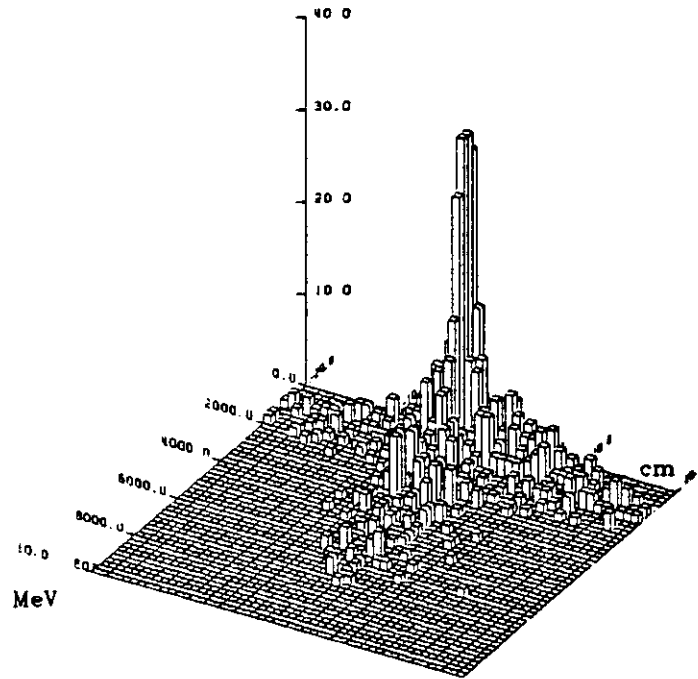


Figure 40: Total energy versus  $z$  vertex for colliding beam data

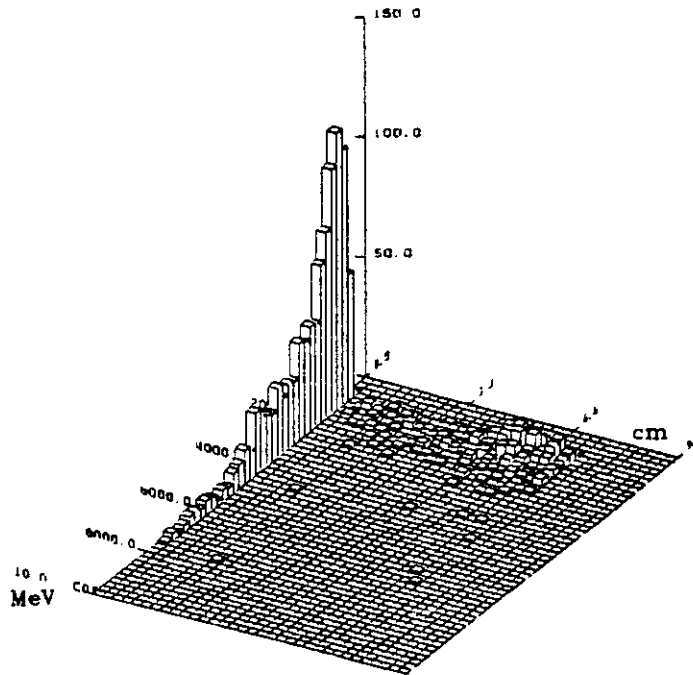


Figure 41: Total energy versus  $\rho$  vertex for colliding beam data

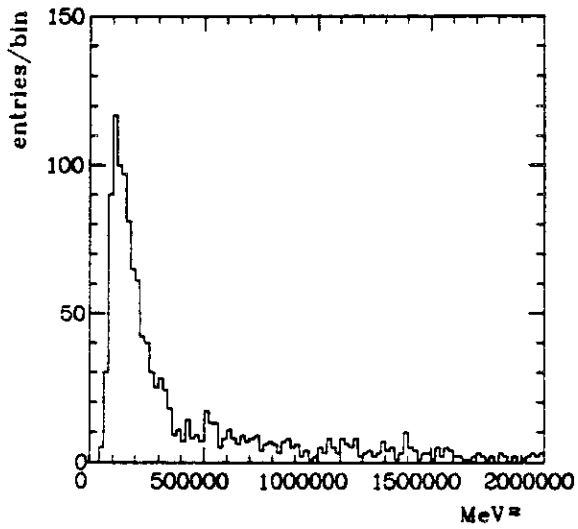


Figure 42:  $E_T^2$  for colliding beam data

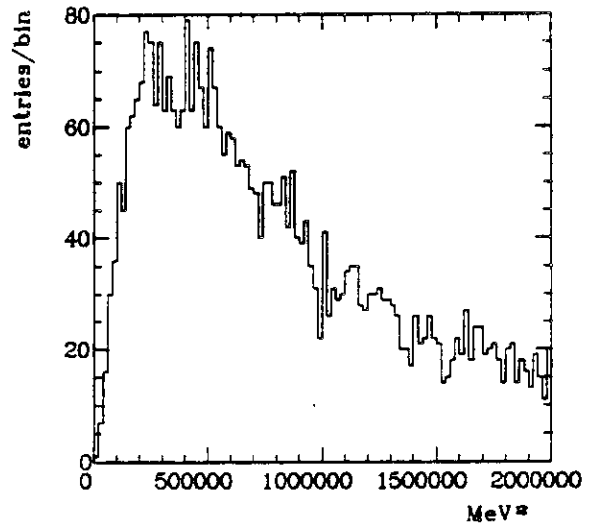


Figure 43:  $E_T^2$  for Monte Carlo  $\gamma\tau\tau$  events

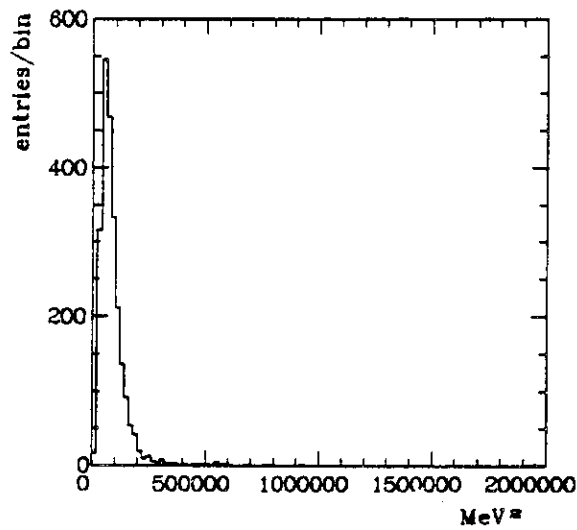


Figure 44:  $E_T^2$  for separated beam data

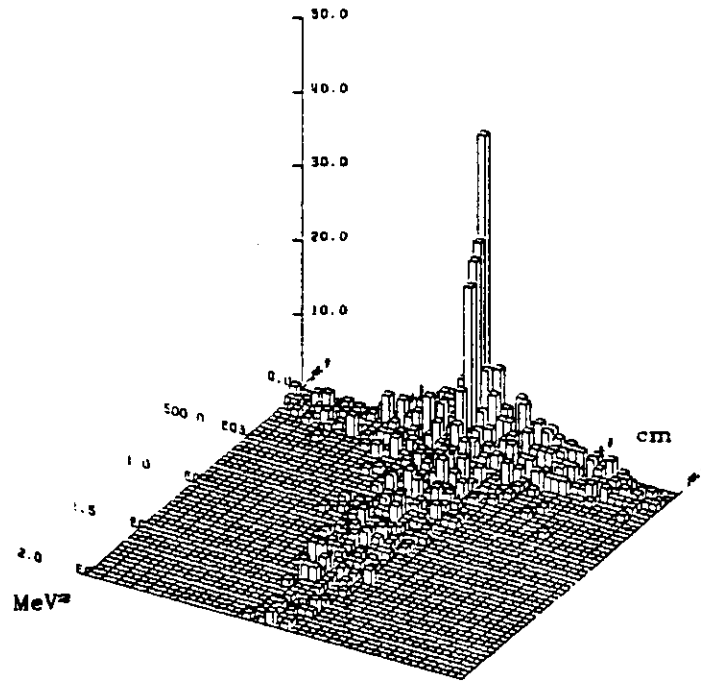


Figure 45:  $E_T^2$  versus  $z$  vertex (colliding beams)

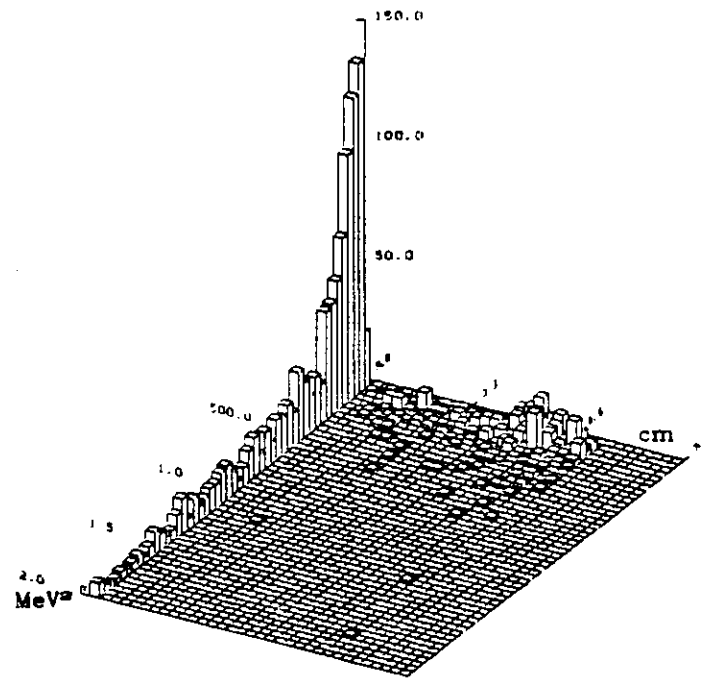


Figure 46:  $E_T^2$  versus  $\rho$  vertex (colliding beams)

cut		$\Upsilon$	$\Upsilon'$
Input from preselection		172486	263831
1	$E_{\text{Total}} \leq 8 \text{ GeV}$	99%	99%
2	No track in tunnel with $\sum_{13} \geq 100 \text{ MeV}$	69%	75%
3	2 charged tracks $\sum_{13} \geq 150 \text{ MeV}$	14%	40%
4	1 electron, charged, $\sum_{13} \geq 500 \text{ MeV}$ , standard pattern cut.		
5	1 muon, charged, $150 \text{ MeV} \leq \sum_{13} \leq 350 \text{ MeV}$ , minimum ionizing pattern cut.	0.38%	0.56%
6	Trigger simulation	0.37%	0.54%
7	1 gamma, neutral, not a merged $\pi^0$	0.15%	0.23%
8	no $\pi^0$	0.13%	0.21
9	exactly 3 tracks with $\sum_{13} \geq 50 \text{ MeV}$ in $ \cos \Theta  \leq 0.84$	0.11%	0.16%
10	$E_T^2 \geq 0.2 \text{ GeV}^2$	0.074%	0.089%
11	No offaxis tracking as of TAGTRK	0.067%	0.070%
Output		115	184

Table 6: Final selection criteria and transmission of subsequent cuts

The muon definition is standard (see appendix A) with a  $\approx 30\%$  pion contamination from non interacting pions. There is however no way to avoid this misidentification since the Crystal Ball detector has no muon identification system. The gamma finally must not be consistent with originating from a  $\pi^0$  with both photons being merged to a single energy deposition (details in  $\pi^0/\gamma$  separation in appendix A). This is another cut against the above mentioned background of  $\tau \rightarrow \rho \nu_\tau$ .

The cut off at 50 MeV for additional tracks in the main detector proves to be un-critical from DBM trigger studies, see figure 48 where we display the typical energy of tracks in DBM events. The final two cuts on  $E_T^2$  and onaxis tracking where already justified above. The cut value for  $E_T^2$  can be read off figures 42, 44 and 43.

Finally the trigger simulation ensures that the Monte Carlo simulated data are treated the same way the real data are. The thresholds in the criteria applied are set slightly higher than for the actual data taking in order to be on the safe side. If the trigger criteria would be less restrictive than the actual trigger we would pass Monte Carlo events which would never have been triggered on in the real world.

This analysis leaves us with a final sample of 115 events for the  $\Upsilon$  and 184 events for the  $\Upsilon'$  data. Physics results from this sample will be deferred until after discussing how the acceptance for the reaction under investigation is calculated.

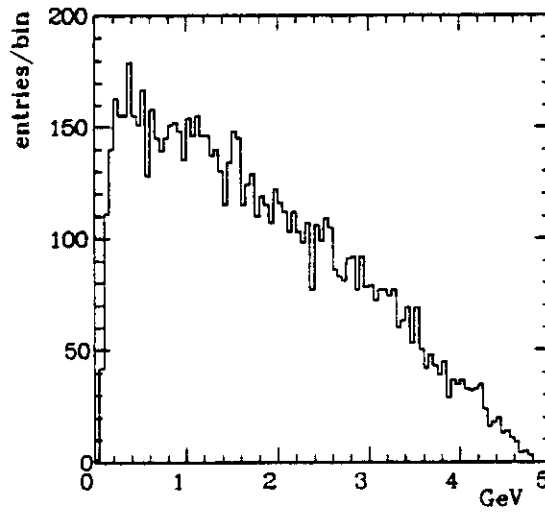


Figure 47: Electron energy spectrum from  $\tau$  decays

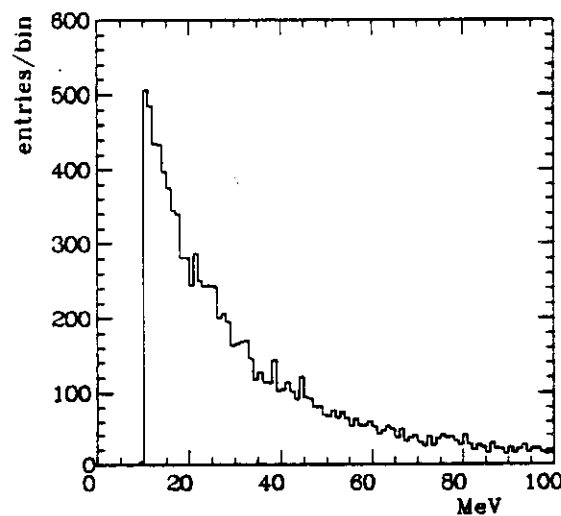


Figure 48: Energy of tracks from DBM events

## 5.2 Acceptance Studies

### 5.2.1 Monte Carlo Studies

The Crystal Ball Monte Carlo consists of two subsequent steps, STEP1 generating the 4-vectors for the reaction under investigation and STEP2 simulating the response of the various detector components. For this analysis we need to simulate the following reactions:

- $\Upsilon, \Upsilon' \rightarrow \gamma X \rightarrow \gamma \tau \bar{\tau}$  (for various masses of X)
- $e^+ e^- \rightarrow \gamma \tau \bar{\tau}$  (initial state bremsstrahlung)

We need the first reaction to calculate the efficiency for finding events of this type. The second one will allow us to check whether the observed background photon spectrum can be explained by conventional  $\tau$  pair production (in shape and magnitude). Details on both generators and STEP2 can be found in appendix B. To make the output of STEP2 look like real data EOTAP (see chapter 4.2) was applied. In addition the information from beam related background has to be added, since the simulation does not account for that. This is accomplished by adding to each Monte Carlo event the crystal energy information of a DBM event (from a sample selected proportional to luminosity), so called 'DBM merging'. This datasample is then subjected to the same analysis programs as the data.

Due to differences in the tubechamber performance for simulation and data the detection efficiencies have to be corrected. Probabilities for a charged particle to be identified as charged by the software can be found for Monte Carlo data by using the STEP1 information. Starting from a particle found in the detector we search for the generated track which is closest. A Monte Carlo tubechamber efficiency is then defined by:

$$\epsilon_{\text{MonteCarlo}}^{\text{Tubechamber}} = \frac{\text{Number of identified charged MC tracks seen in detector}}{\text{Number of generated charged MC tracks}}$$

On the other hand we can find a tubechamber efficiency for data by looking into events of the type  $e^+ e^- \rightarrow e^+ e^-$  and  $e^+ e^- \rightarrow \mu^+ \mu^-$ . Selecting such events allows a determination of

$$\epsilon_{\text{Data}}^{\text{Tubechamber}} = \frac{\text{Number of charged tracks seen in detector}}{2 \times \text{number of events}}^{10}$$

The first reaction has to be corrected for contributions from  $e^+ e^- \rightarrow \gamma \gamma$  using Monte Carlo methods. We can also ask how many neutral tracks are misidentified as charged. This misidentification results from random hits in the tubechambers and from photons converting into an  $e^+ e^-$  pair in the material of the beampipe or the tubechambers. This conversion probability amounts to about 10% leading to  $\approx 6\%$  of the neutrals to be found

---

<sup>10</sup>Since there are 2 tracks per event.

	$\Upsilon$	$\Upsilon'$
Charged particle, identified charged	97%(96%)	94%(93%)
Neutral particle, identified neutral	$(97\pm 0.5)\%$	$(94\pm 0.5)\%$

Table 7: Tubechamber efficiencies

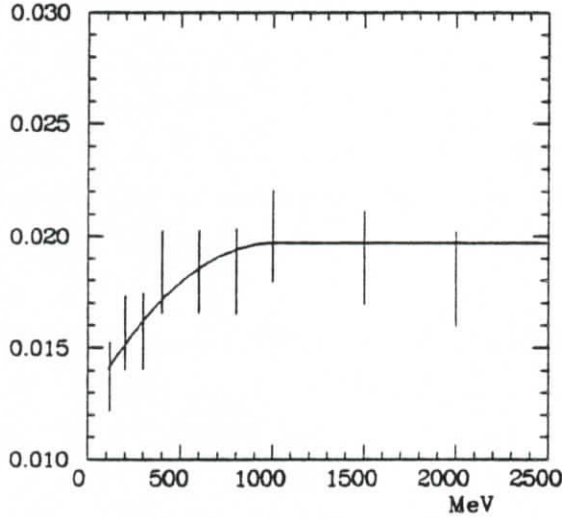


Figure 49: Detection efficiency for  $\Upsilon \rightarrow \gamma X \rightarrow \gamma \tau \bar{\tau}$  as function of the photon energy

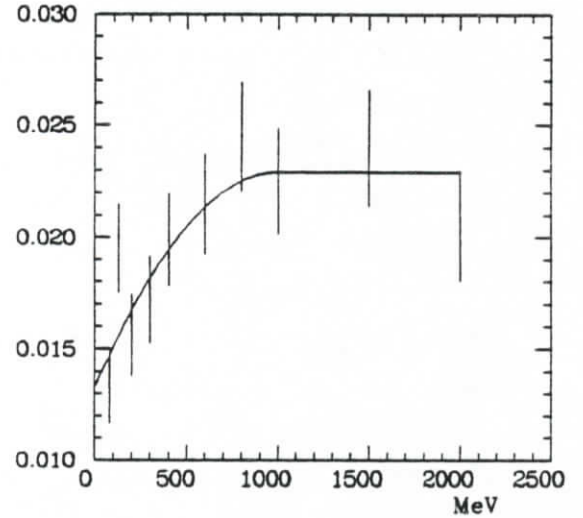


Figure 50: Detection efficiency for  $\Upsilon' \rightarrow \gamma X \rightarrow \gamma \tau \bar{\tau}$  as function of the photon energy

as charged. This difference is due to the fact that a conversion in the last layer of the tubechambers would not lead to an identification as charged, but is included in the 10%. For Monte Carlo data this is done analogous to the charged case, for data using a sample of photons from  $\gamma\gamma$  production of the  $f$ -meson ( $f \rightarrow \pi^0 \pi^0$ ). A compilation of the relevant numbers can be found in table 7. The numbers are for  $e^+e^- \rightarrow e^+e^-$ , in parentheses are those for  $e^+e^- \rightarrow \mu^+\mu^-$ . These numbers however can only be used for corrections to the detection efficiency if the tubechamber efficiency proves to be independent of the particle type and momentum. Table 7 already shows a small difference between beam energy electrons and muons. We estimate the variation in efficiency over the whole range of particle types and energies to be less than  $\pm 5\%$ .

Taking the Monte Carlo samples after DBM merging and EOTAP, corrected for different tubechamber efficiencies, leads to the detection efficiencies of figures 49 and 50. The decreasing efficiency at low photon energies is mostly due to the photon recognition, since we require the photon to pass a standard pattern cut. The efficiencies are so low due to the small branching fraction of  $\tau\tau \rightarrow e\mu$  (+ neutrinos) of  $\approx 6.3\%$ .

### 5.2.2 Systematic Effects

There are various sources for systematic uncertainties:

- Tubechamber efficiencies (data and Monte Carlo)
- Monte Carlo simulation of detector response
- Number of hadrons (see chapter 4.1)

Concerning the tubechamber efficiency in the data, subtraction of the  $\gamma\gamma$  contamination yields an uncertainty of 5% due to the uncertainty in the Monte Carlo calculation of both processes ( $e^+e^- \rightarrow e^+e^-$  and  $e^+e^- \rightarrow \gamma\gamma$ ). This uncertainty does not originate on the generator level, but at the stage of recognition in the detector (both processes are strongly peaked forward). The variation of ionization for different particles amounts to another 5% (see above). Finally a statistical error due to a limited Monte Carlo data sample for these studies amounts to 0.5%. Simulating the detector response induces an overall estimated error of 10%. This is mostly due to uncertainties in the simulation of hadrons and to imperfections in defining the detector components (e.g. multiple scattering and energy loss in the beampipe and tubechambers is not included.), for details see appendix B. Finally the number of hadrons is known only up to  $\pm 7.5\%$  ( see chapter 4.1) due to uncertainties in the detection efficiency for hadrons.

Adding all these errors in quadrature <sup>11</sup> yields a total systematic error of

$$\epsilon_{\text{systematic}} = 14\%$$

### 5.3 Physics Results

In this section we will present the final photon spectrum for  $\gamma e\mu$  final states. For the  $\Upsilon$  decays the minimum photon energy is 100 MeV (50 MeV for the  $\Upsilon'$ ).

Since we do not observe significant signals we will convert these spectra into upper limits for the reaction  $\Upsilon, \Upsilon' \rightarrow \gamma X \rightarrow \gamma\tau\bar{\tau} \rightarrow \gamma e\mu (+\text{neutrinos})$ . Figures 51, 52, 53 and 54 show these spectra for  $21.8\text{pb}^{-1}$   $\Upsilon$  and  $37.2\text{pb}^{-1}$   $\Upsilon'$  decays together with an equivalent of  $21.4\text{pb}^{-1}$   $\Upsilon$  and  $25.8\text{pb}^{-1}$   $\Upsilon'$  Monte Carlo data for the reaction  $e^+e^- \rightarrow \gamma\tau\bar{\tau}$ . In table 8 we compare the number of events for data and Monte Carlo. The later are corrected for different tubechamber efficiencies in data and Monte Carlo as well as luminosities. Corrections for  $\tau$  pairs from  $\Upsilon, \Upsilon', \dots$  decays are also applied. The resonance decays contribute 'photons' to the spectra which are either misidentified merged  $\pi^0$ s or gammas from open  $\pi^0$ s. This latter contribution is evaluated using Monte Carlo methods. Comparing the spectra for data and Monte Carlo for  $\Upsilon$  and  $\Upsilon'$  we observe that they agree well in shape (both are approximately flat on a logarithmic scale due to the  $1/k$  nature of photons from initial state bremsstrahlung). Table 8 on the other hand shows an agreement (within errors) also in magnitude. Thus we conclude that the observed events of the type  $\gamma e\mu$  are consistent with originating from direct  $\tau$  pair production. Observing no obvious monochromatic photon line (figure 55 shows Monte Carlo expect-

<sup>11</sup>This is justified assuming these errors to be gaussian and uncorrelated.

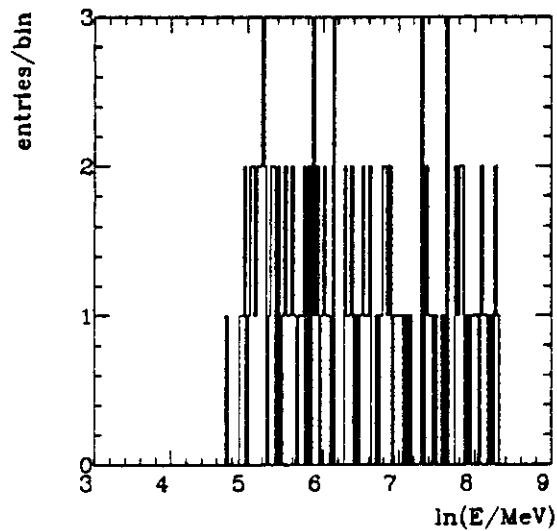


Figure 51: Photon energy for  $\gamma e\mu$  final states,  $\Upsilon$

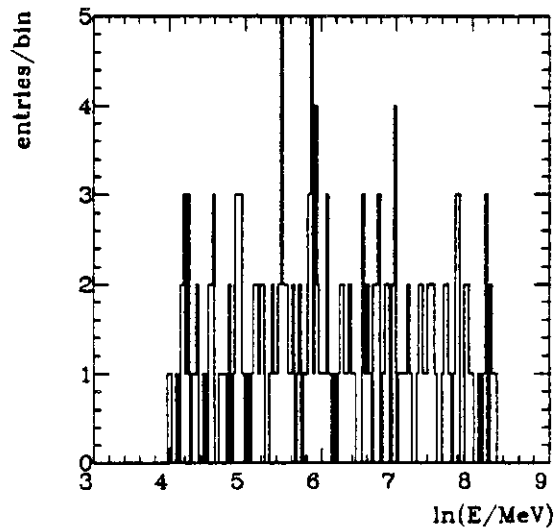


Figure 52: Photon energy for  $\gamma e\mu$  final states,  $\Upsilon'$

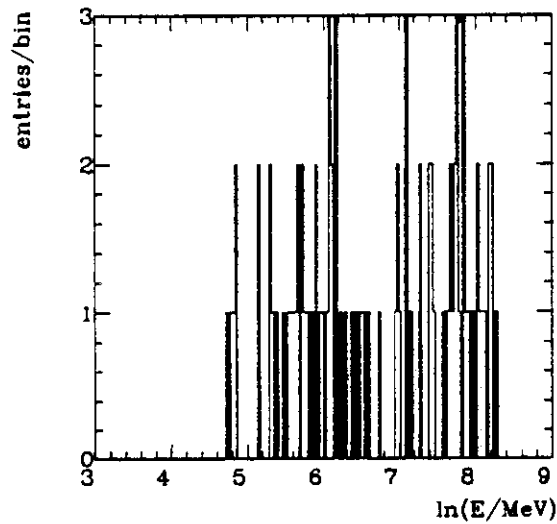


Figure 53: Photon energy for  $\gamma e\mu$  final states,  $\Upsilon$  Monte Carlo

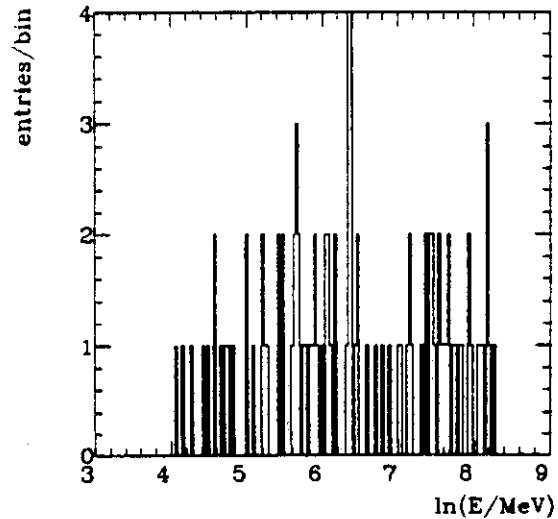


Figure 54: Photon energy for  $\gamma e\mu$  final states,  $\Upsilon'$  Monte Carlo

	data	Monte Carlo
$\Upsilon$	$115 \pm 11$	$114 \pm 11 \pm 16$
$\Upsilon'$	$184 \pm 14$	$174 \pm 13 \pm 24$

Table 8: Number of events for  $\gamma e \mu$  final state. The errors are statistical and systematical respectively.

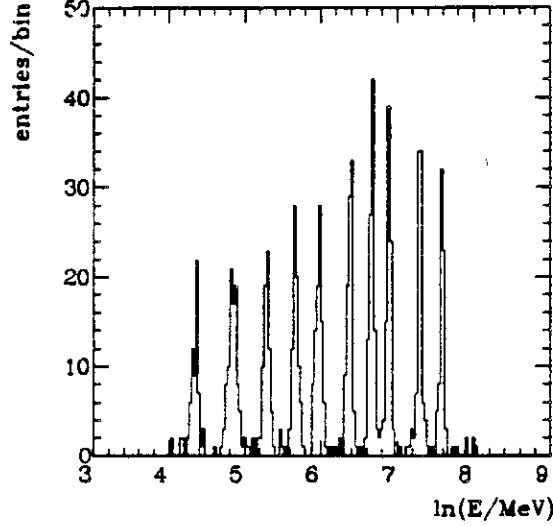


Figure 55: Photon energy distribution Monte Carlo events,  $\Upsilon, \Upsilon' \rightarrow \gamma X \rightarrow \gamma \tau \bar{\tau}$  for various masses X (9.4 GeV – 7.2 GeV)

tations for various masses of X) we convert the photon spectra into an upper limit for the existence of the reaction  $\Upsilon, \Upsilon' \rightarrow \gamma X \rightarrow \gamma \tau \bar{\tau}$ . To this end we perform for each photon energy a fit (maximum likelihood, see appendix C) to the photon spectra, assuming a gaussian signal of known width ( $\frac{2.7\%}{(E/\text{GeV})^{0.22}}$ , as of figure 55) and variable amplitude on top of a flat background. With the background parameters fixed to the values of maximum likelihood we vary the amplitude from essentially  $-\infty$  to  $+\infty$ . The amplitude  $A_0$  for which ( $L = \text{likelihood}$ ,  $A = \text{amplitude}$ )

$$\int_0^{A_0} L(A) dA = 0.9 \int_0^{+\infty} L(A) dA$$

is defined as the upper limit at 90% confidence level. In figures 56 and 57 we display the upper limits for  $\Upsilon$  and  $\Upsilon'$ , corrected for efficiency and divided by the number of hadrons as function of the mass X in  $\Upsilon, \Upsilon' \rightarrow \gamma X \rightarrow \gamma \tau \bar{\tau}$ .

The upper limits for the  $\Upsilon$  are about a factor 2 lower than those for the  $\Upsilon'$  since the resonant production cross section is higher for the  $\Upsilon$ , see chapter 4.1, figure 24. Therefore the number of QED (background) events per resonance event turns out to be 3 times higher at the  $\Upsilon'$ .

For example we can rule out a heavy object of mass  $X = 8.3 \text{ GeV}$  decaying into a  $\tau$  pair in radiative  $\Upsilon$  decays with a branching ratio  $\text{BR} < 1 \times 10^{-3}$  at a 90% confidence level.

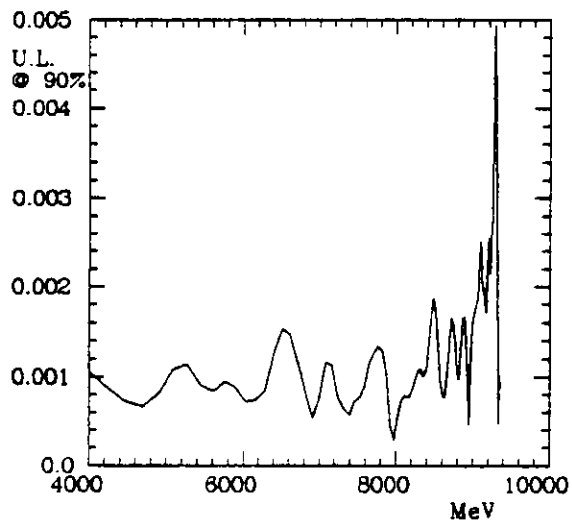


Figure 56: 90% upper limit as function of recoil mass,  $Y$

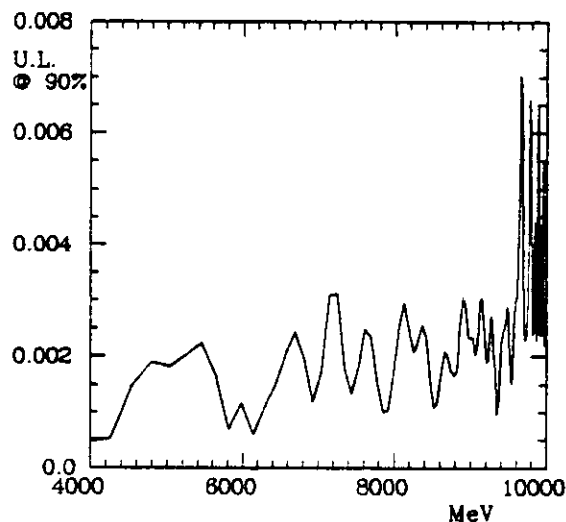


Figure 57: 90% upper limit as function of recoil mass,  $Y'$

## 6 The Decays $\tau \rightarrow e\gamma$ and $\tau \rightarrow e\pi^0$

### 6.1 Analysis

#### 6.1.1 Introduction

The two reactions under investigation,  $\tau \rightarrow e\gamma$  and  $\tau \rightarrow e\pi^0$ ; though not foreseen in the standard model are predicted by various composite model theories. Possible mechanisms for such decays were already discussed in chapter 2. Since both decay modes are very similar in their topology (a  $\pi^0$  is light on the scale of a beam energy  $\tau$  lepton) we will discuss them together.

In principle there are two possible ways to look for such reactions in  $\tau$  pair decays. First one can identify all final state particles and therefore proof that there was a conventional decay of one of the  $\tau$  leptons. In the decay of the other  $\tau$  lepton one can then try to search for the reactions under investigation. This method however suffers badly from efficiency problems since the  $\tau$  lepton identification in the Crystal Ball detector looks only feasible in  $\tau \rightarrow e \bar{\nu}_e \nu_\tau$  and  $\tau \rightarrow \mu \bar{\nu}_\mu \nu_\tau$ .

Therefore we choose a semi inclusive method. By using the preselected data sample of the  $Y' \rightarrow \gamma X \rightarrow \gamma \tau \bar{\tau}$  (see chapter 5.1.2) analysis we start from a low multiplicity ( $\tau$  pair like) environment (for the criteria of this preselection see table 5). The  $\tau$  lepton, which decays conventional, is not analyzed further and the decays  $\tau \rightarrow e\gamma$  and  $\tau \rightarrow e\pi^0$  of the second  $\tau$  are characterized by their peculiar topology. This approach is supported by Monte Carlo studies of the decay kinematics which lead to a good separation of both  $\tau$  leptons. Therefore in most of the cases the conventional  $\tau$  decay products will be confined to one halfsphere and the other halfsphere can be searched for the unconventional decay.

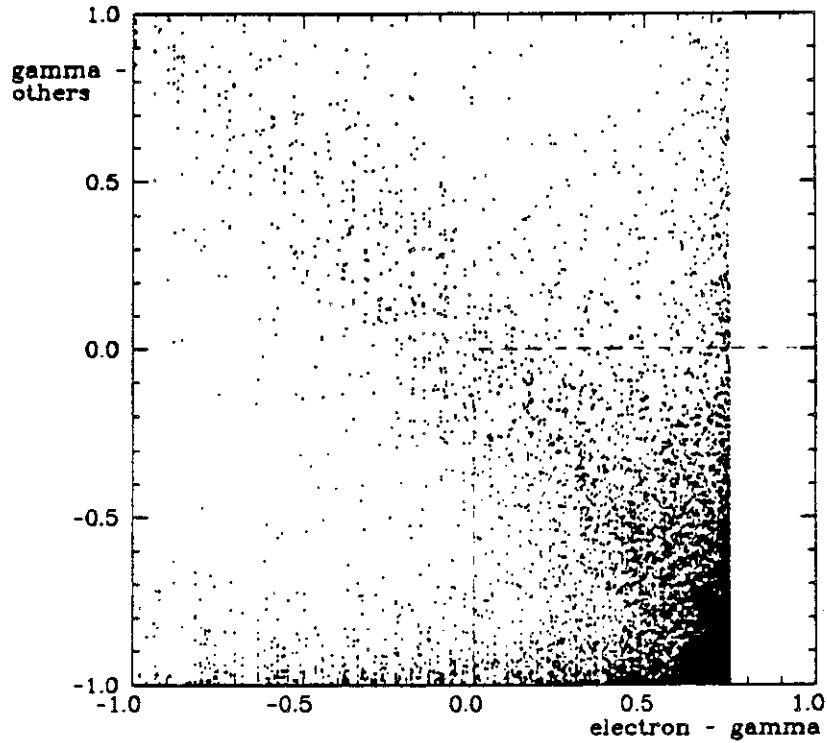


Figure 58: Cos(angle) between gamma and electron versus cos(angle) between gamma and others

### 6.1.2 Selection of $\tau \rightarrow e\gamma$

In order to develop selection criteria we generate Monte Carlo events according to

$$e^+e^- \rightarrow \tau_1\tau_2 \quad \begin{array}{l} \tau_1 \rightarrow \text{conventional modes} \\ \tau_2 \rightarrow e\gamma \text{ or } \tau_2 \rightarrow e\pi_0 \end{array}$$

for details of the generation see appendix B. Already at the generator level (STEP1) we recognize some important features. In figure 58 we show the angle between the gamma and the electron from  $\tau \rightarrow e\gamma$  versus the angle between the gamma and decay products of the other  $\tau$  which decays conventional. We observe a clear correlation between electron and gamma. This suggests to require an electron and a gamma without other particles in a halfsphere defined by the gamma direction. This cut is indicated in figure 58 by the dotted line.

A major background arises from radiative Bhabha events

$$e^+e^- \rightarrow e^+e^-\gamma$$

The photon and one of the electrons will be in one halfsphere and the second electron will fake a conventional  $\tau$  decay which is not analyzed further. Most of these events can be rejected by a cut in the total energy, since this type of events should deposit the whole CMS energy in the detector in contrast to the  $\tau$  leptons where the neutrinos carry away a substantial fraction of the energy. In figure 59 we display the total energy

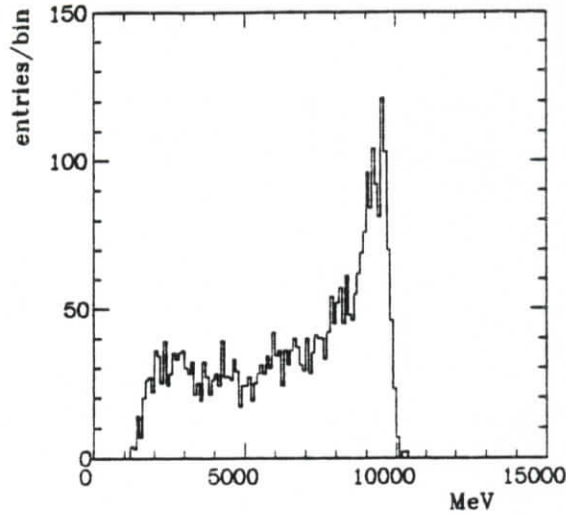


Figure 59: Total energy for events with an isolated electron gamma pair

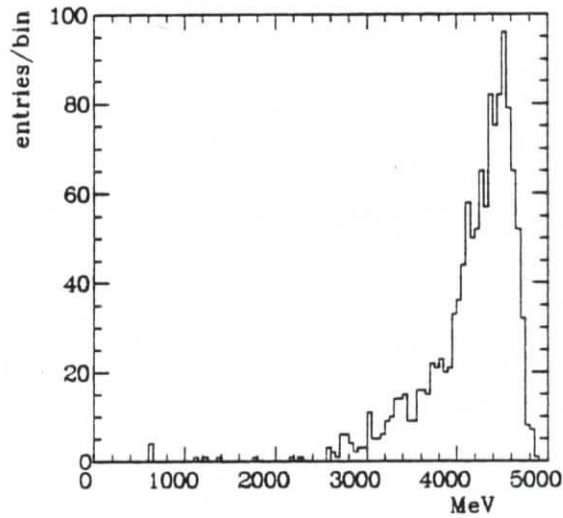


Figure 60: Energy ( $\sum_{13}$ ) of beamenergy Monte Carlo electrons

for events with one electron and one gamma in one hemisphere. A clear accumulation at twice the beam energy is visible.

There are events however where the energy of one of the final state particles is not measured correctly. This effect is called leakage<sup>12</sup> and results from fluctuations in the shower development, decreasing the containment of energy in the detector. This is illustrated by figure 60 displaying the energy distribution ( $\sum_{13}$ ) for beam energy Monte Carlo electrons. The tail towards low energies is due to this leakage effect. The total energy of such events will be substantially lower than the CMS energy. To reject these we calculate the opening angle of the two electrons in their restframe  $\Theta^*$  (the boost of this frame is given by the photon energy). For radiative Bhabhas this angle should be  $180^\circ$ . Indeed we observe a spike in this quantity (figure 61) which is only found much smaller in the Monte Carlo simulation of  $\tau \rightarrow e\gamma$  and  $\tau \rightarrow e\pi^0$ , see figure 62.

<sup>12</sup>For a detailed discussion of this effect see reference [49]

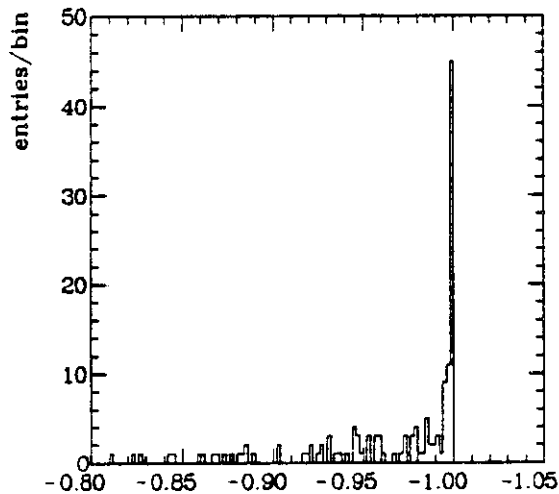


Figure 61: Cos(Opening angle) of the 2 electrons in their restframe, data

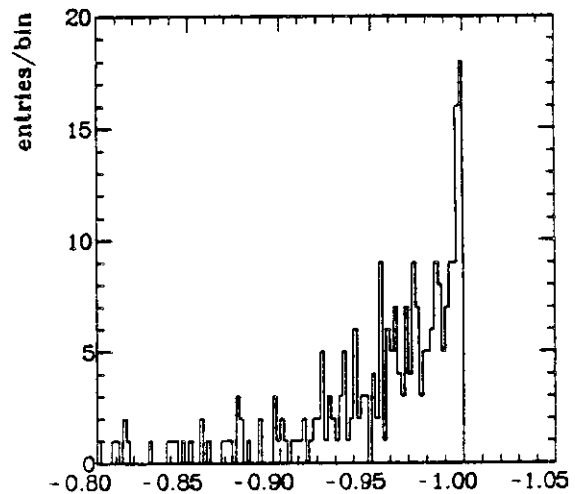


Figure 62: Cos(Opening angle) of the 2 electrons in their restframe, Monte Carlo

For events where one electron misses a lot of energy due to leakage  $\Theta^*$  will not be exactly  $180^\circ$  since the particle momentum used in the Lorentz transformation is too small. These events are finally rejected if they can be fit kinematically to the hypothesis

$$e^+e^- \rightarrow e^+e^-\gamma$$

(leaving the two electron energies free) with a confidence level of more than 10% (see section 6.1.3 for details).

In the following we will describe (in table 9) and discuss the selection criteria used. We start from the preselected data sample as of chapter 5.1.2. This sample contains low multiplicity ( $\tau\tau$  like events). In cuts 1-4 we isolate events with at least one photon and one lepton. At this stage we still keep the events with 1 muon as well as with 1 electron for technical reasons. We require that there is no other particle ( $\sum_{i3} \geq 50 \text{ MeV}$ ) in this halfsphere. This is justified by the strong correlation between electron and photon (see figure 58).

Comparing the total energy at this stage (see figure 59) with the Monte Carlo prediction in figure 63 <sup>13</sup> shows that we can reject a lot of background from radiative Bhabha events by requiring the total energy to be less than 8 GeV. On the other hand the lower bound on  $E_{\text{Total}}$  should be about  $E_{\text{Beam}}$ , since the total energy of the decay products from  $\tau \rightarrow e\gamma$  should be seen in the detector.

The next two cuts are designed to reject events from conventional  $\tau$  pair production. The peculiar topology of the decays under study with high energetic energy depositions in the ball yields high values of  $E_T$  ( $E_T = \sum_{i=1}^{720} E_i \sin \Theta_i$ ) and  $E_T^2$  (as defined in chapter 5.1.3). For a comparison of data and Monte Carlo prediction see figures 64 and 65 for

<sup>13</sup>The clustering at  $E_{\text{Beam}}$  is due to events where the  $\tau$  which decays conventional is lost. The decay products of  $\tau \rightarrow e\gamma$  deposit  $E_{\text{Beam}}$ .

cut	$\Upsilon'$
Input from preselection	554504
within $ \cos \Theta  \leq 0.84$ :	
1 $\geq 1$ gamma, neutral, $\sum_{13} \geq 500$ MeV, standard pattern cut.	
2 $\geq 1$ electron, charged, $\sum_{13} \geq 500$ MeV, standard pattern cut or $\geq 1$ muon	5.0%
3 $\geq 1$ gamma with no track $\sum_{13} \geq 50$ MeV in same hemisphere besides e or $\mu$	2.0%
4 $\geq 1$ gamma with exactly 1 lepton in same hemisphere	1.1%
5 Trigger simulation	1.1 %
6 $\geq 1$ electron	0.61 %
7 $4500 \text{ MeV} \leq E_{\text{Total}} \leq 8000 \text{ MeV}$	0.21 %
8 $E_T \geq 1250 \text{ MeV}$	0.053 %
9 $E_T^2 \geq 2 \text{ GeV}^2$	0.043 %
10 $E_{\text{Debris}}/E_{\text{Total}} \leq 0.1$	0.035 %
11 1 gamma, no $\pi^0$	0.034 %
12 Opening angle $\cos \Theta^* \geq -0.998$	0.016 %
13 for 2 charged, 1 gamma events: confidence level for kinematic fit $CL \leq 10\%$	0.011 %
Output	60

Table 9: Selection criteria for the decay  $\tau \rightarrow e\gamma$

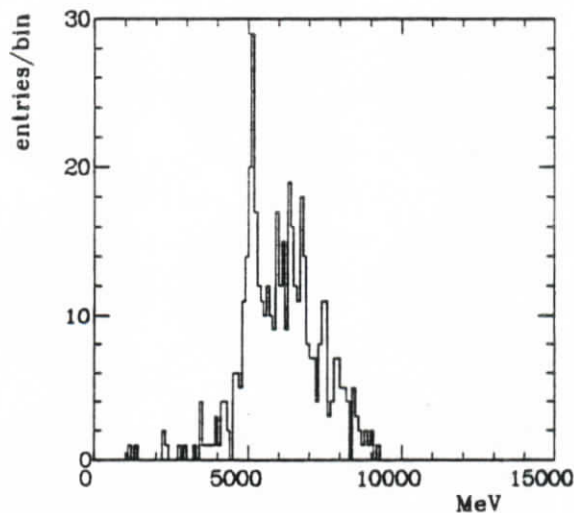


Figure 63: Total energy for  $\tau \rightarrow e\gamma$ , Monte Carlo prediction

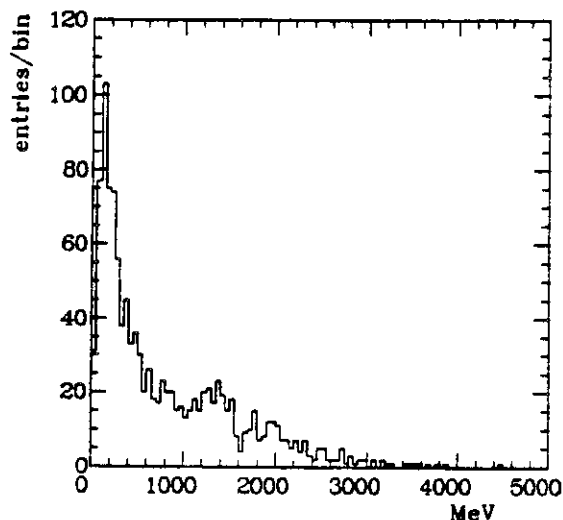


Figure 64:  $E_T$  for data

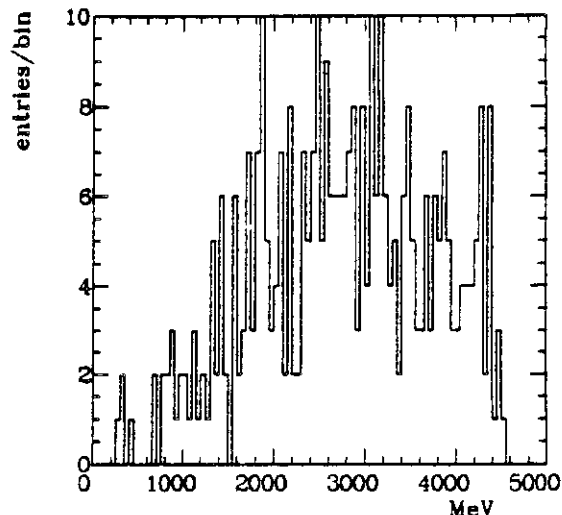


Figure 65:  $E_T$  for Monte Carlo

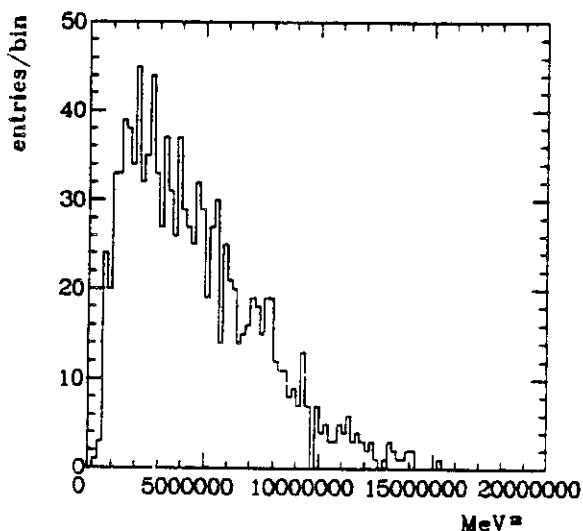


Figure 66:  $E_T^2$  for data

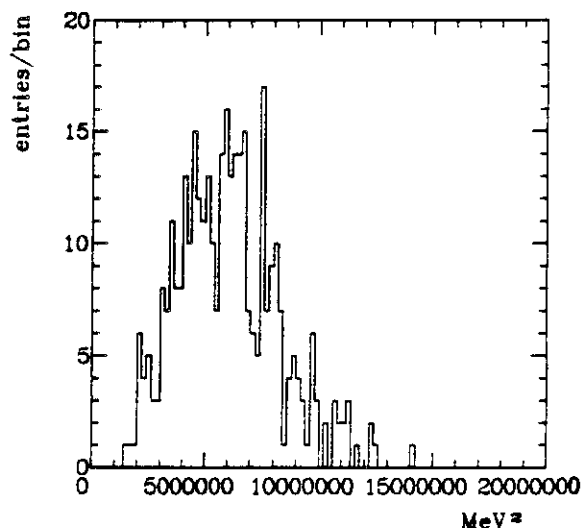


Figure 67:  $E_T^2$  for Monte Carlo

$E_T$  and figures 66 and 67 for  $E_T^2$ . It is suggestive to cut at the values given in table 9.

In a next step we want to keep only clean events. Clean means that there should not be too much extra energy outside energy depositions from particles (so called debris). A particle should deposit most of its energy in a group of 13 crystals ( $\Sigma_{13}$ ), see chapter 4.2. Therefore the fraction of energy outside these groups of 13 crystals is a measure for the cleanliness of an event. We show the fraction  $E_{\text{Debris}}/E_{\text{Total}}$  in figures 68 and 69 for data and Monte Carlo respectively. An excess can be seen for the data, thus we cut at 10% debris energy. Note that the  $\Sigma_{13}$  which enters the energy sum is not corrected by PCORR (see chapter 4.2), since we want to have the energy deposited and not the best measure for the particle energy.

The photon candidate is required to be inconsistent with a  $\pi^0$ . This is again done

---

products of  $\tau \rightarrow e\gamma$  deposit  $E_{\text{Beam}}$ .

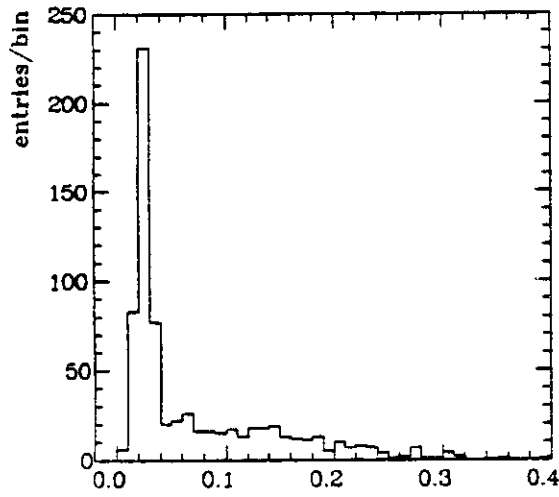


Figure 68: Debris energy for  $\tau \rightarrow e\gamma$  data

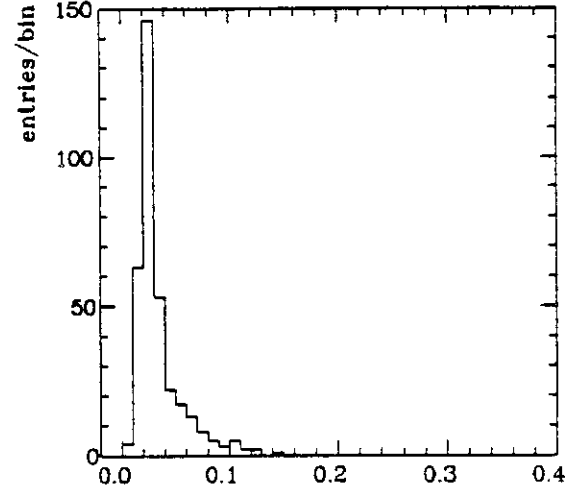


Figure 69: Debris energy for  $\tau \rightarrow e\gamma$  Monte Carlo data

by using the shower mass and requiring (see chapter 5.1.3)

$$\text{Shower mass} \geq \frac{\sum_{13} \times 300}{4000} \text{ MeV and } 400 \text{ MeV} \leq \sum_{13} \leq 2000 \text{ MeV}$$

The two final cuts were already discussed above.

### 6.1.3 Kinematic Fitting

A kinematic fit uses the constraints of four momentum conservation ( $E_{\text{Total}} = E_{\text{CMS}}$ ,  $P_X^{\text{Total}} = P_Y^{\text{Total}} = P_Z^{\text{Total}} = 0$ ) to improve the measured values ( $E$ ,  $\Theta$ ,  $\Phi$ ,  $m$ ) of each final state particle. This is accomplished by minimizing a  $\chi^2$  under these constraints for each particle. This  $\chi^2$  is defined as

$$\chi^2 = \sum_{i=1}^n \sum_{j=1}^3 (X_{i,j}^{\text{measured}} - X_{i,j}^{\text{fitted}})^2 / \sigma_{i,j}^2$$

where  $X_j$  denotes the variables ( $E$ ,  $\Theta$ ,  $\Phi$ ) for each of the  $n$  final state particles and  $\sigma$  are the measurement errors of these variables. A confidence level which is a measure for the event to originate from the reaction assumed, can then be defined as ( $n_D$  = number of degrees of freedom)

$$\text{CL} = \int_{\chi_0^2}^{\infty} d\chi^2 P_{n_D}(\chi^2)$$

where  $\chi_0^2$  is the  $\chi^2$  for this particular event and

$$P_n(\chi^2) = \frac{1}{2^{n/2} \Gamma(n/2)} (\chi^2)^{n/2-1} e^{-\chi^2/2} d\chi^2$$

the probability density function<sup>14</sup>. For gaussian distributed measurement errors it can be shown that the confidence level should be distributed flat between 0% and 100%.

<sup>14</sup>For a derivation and further details see reference [51].

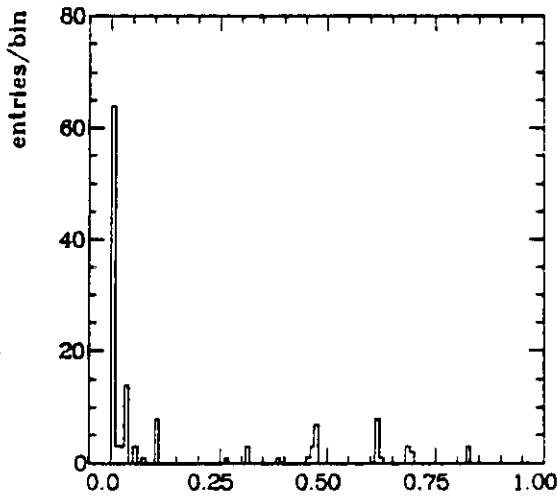


Figure 70: Confidence level distribution  $\tau \rightarrow e\gamma$  Monte Carlo events

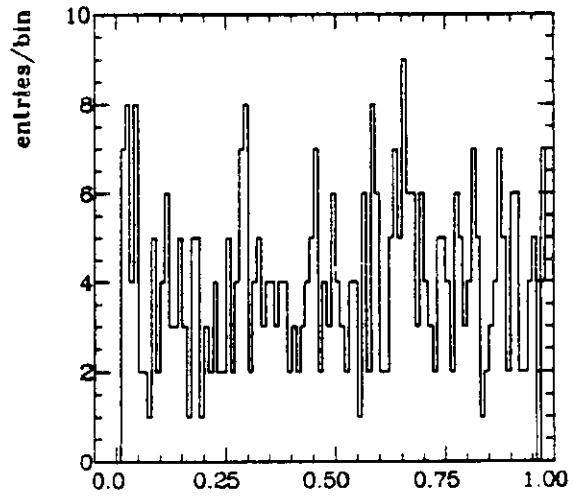


Figure 71: Confidence level distribution for Monte Carlo radiative Bhabha events

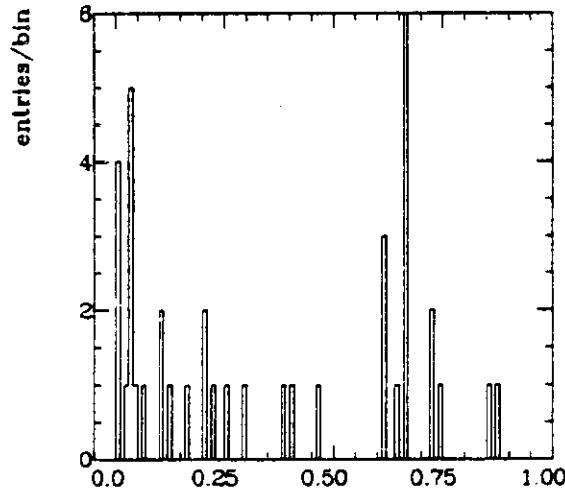


Figure 72: Confidence level distribution for data.

Figure 70 displays this distribution for  $\tau \rightarrow e\gamma$  Monte Carlo events. These events cannot be fit to the hypothesis  $e^+e^- \rightarrow e^-e^- \gamma$ , therefore we observe a clustering at low confidence level. Figure 71 on the other hand shows the confidence level (CL) distribution for Monte Carlo simulated radiative Bhabha events. These can be fitted to the hypothesis  $e^+e^- \rightarrow e^+e^- \gamma$ , leading to a flat CL distribution. In figure 72 we finally show the CL distribution for the events under investigation. Here we observe a flat component which is probably due to radiative Bhabhas. In order to reject these we require a  $CL \leq 10\%$  for our analysis.

The fits were performed leaving both electron energies free to avoid an influence of leakage. This can be done since the kinematic fit is fourfold overconstrained due to four momentum conservation ( regarding the two electron momenta as free variables results in a problem which is still twofold overconstrained).

cut	$\Upsilon'$
Input from preselection	263831
1 within $ \cos \Theta  \leq 0.84$ :	
$\geq 1 \pi^0$ , neutral, $\sum_{13} \geq 500 \text{ MeV}$ , shower mass $\geq 80 \text{ MeV}$	
2 $\geq 1$ electron, charged, $\sum_{13} \geq 500 \text{ MeV}$ , standard pattern cut or $\geq 1$ muon	3.8%
3 $\geq 1 \pi^0$ with no track $\sum_{13} \geq 50 \text{ MeV}$ in same hemisphere besides e or $\mu$	1.3%
4 $\geq 1 \pi^0$ with exactly 1 lepton in same hemisphere	0.65%
5 Trigger simulation	0.64%
6 $\geq 1$ electron	0.42%
7 $4500 \text{ MeV} \leq E_{\text{Total}} \leq 8000 \text{ MeV}$	0.17%
8 $E_T \geq 1250 \text{ MeV}$	0.053%
9 $E_T^2 \geq 2 \text{ GeV}^2$	0.039%
10 $E_{\text{Debris}}/E_{\text{Total}} \leq 0.1$	0.025%
11 $1 \pi^0$	0.021%
12 Opening angle $\cos \Theta^* \geq -0.998$	0.017%
Output	44

Table 10: Selection criteria for the decay  $\tau \rightarrow e\pi^0$

#### 6.1.4 Selection of $\tau \rightarrow e\pi^0$

The selection for this channel follows in its main characteristics the one for  $\tau \rightarrow e\gamma$ . Again the selection criteria are motivated by a Monte Carlo simulation of the process. The strong correlation between electron and  $\pi^0$  is again present. The background from radiative Bhabha events is easier to handle in this case, since we require a  $\pi^0$  in the event. Here we define it (since the 2 photons will be merged into a single energy deposition) by its shower mass

$$\text{Shower mass} \geq 80 \text{ MeV}$$

This cut is motivated by looking at this variable versus  $\pi^0$  energy, figure 93 in appendix A. Almost all  $\pi^0$ s are kept with this cut and the photon contamination starts only above 2 GeV to become serious. The other cuts are kept as in  $\tau \rightarrow e\gamma$  besides leaving out the kinematic fit since the background of radiative Bhabha events is already very low at this point (mostly due to the  $\pi^0$  requirement).

In table 10 we give the selection criteria together with their transmission rates.

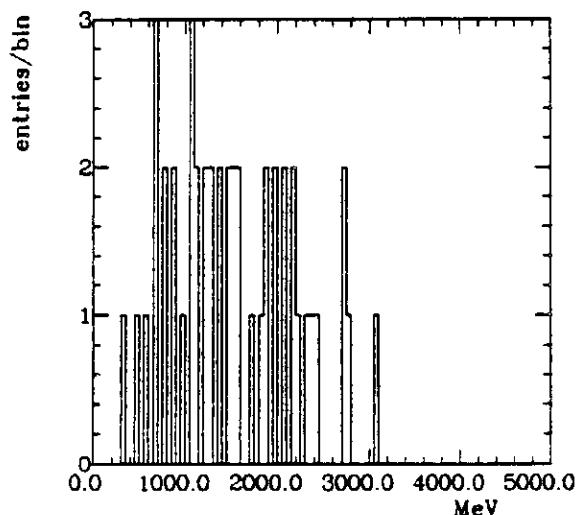


Figure 73: Invariant mass of electron and gamma, data

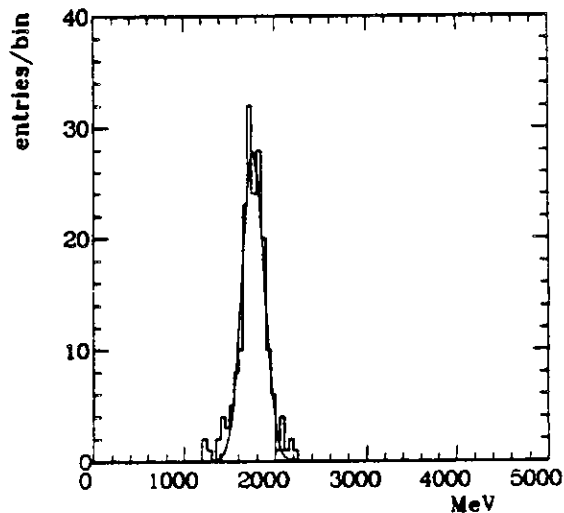


Figure 74: Invariant mass of electron and gamma, Monte Carlo

## 6.2 Physics Results

### 6.2.1 The Decay $\tau \rightarrow e\gamma$

In figure 73 we show the electron gamma invariant mass spectrum for  $60.6\text{pb}^{-1}$   $\Upsilon'$  data. We would expect a signal to look like the one of figure 74 where we display the electron gamma invariant mass for a Monte Carlo simulation. We observe that the fit to figure 74 gives a peak position with an error which is due to the statistical fluctuations of the spectrum. Therefore later on we will have to calculate the upper limit considering this uncertainty. We fit the data to a smooth (linear) background plus a gaussian with fixed width and position (as of figure 74) of variable amplitude. In analogy to the  $\Upsilon, \Upsilon' \rightarrow \gamma X \rightarrow \gamma\tau\bar{\tau}$  analysis we integrate the likelihood function (as a function of the amplitude) up to 90% to get an upper limit at 90% confidence level on the amplitude. Since the expected peak position had an uncertainty we get the upper limits given in table 11. The efficiency for the selection is calculated with Monte Carlo simulation to

Position of peak	Upper limit
1756 MeV	6.4
(1756 + 12) MeV	6.4
(1756 - 12) MeV	6.3

Table 11: Upper limits for  $\tau \rightarrow e\gamma$  as function of peak position

be

$$\epsilon_{\text{Selection}}^{\tau \rightarrow e\gamma} = 0.153$$

The cross section for  $\tau$  pair production is calculated using a radiatively corrected  $\tau$  pair Monte Carlo generator, for details see appendix B. With a luminosity of  $60.6\text{pb}^{-1}$  and the cross section (at  $\sqrt{S} = 10.023$  GeV) of  $1.02\text{nb}$  we find a total number of 123600  $\tau$

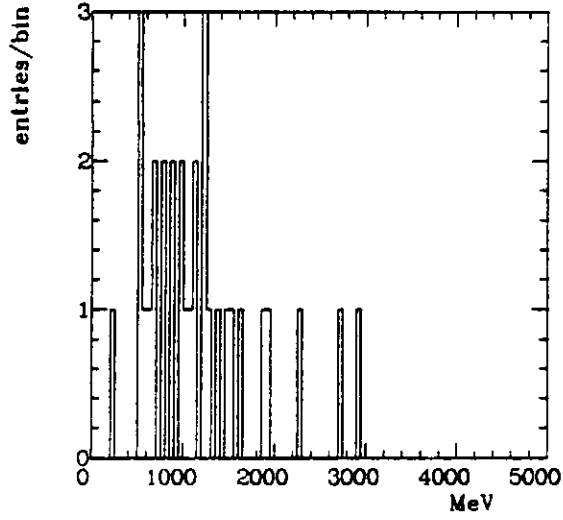


Figure 75: Invariant mass of electron and  $\pi^0$ , data

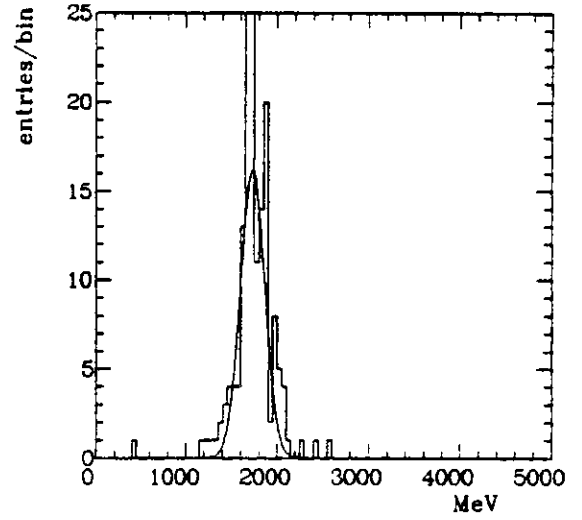


Figure 76: Invariant mass of electron and  $\pi^0$ , Monte Carlo

leptons. An upper limit of 6.4 events then translates into a branching ratio (BR)

$$\text{BR}(\tau \rightarrow e\gamma) < \frac{6.4}{0.153} \frac{1}{123600} = 3.4 \times 10^{-4} (90\% \text{ CL})$$

### 6.2.2 The Decay $\tau \rightarrow e\pi^0$

We present the final  $e\pi^0$  invariant mass spectrum for  $37 \text{ pb}^{-1}$  in figure 75 together with the Monte Carlo expectation for a decay  $\tau \rightarrow e\pi^0$  in figure 76. Again we cannot see a significant structure of the expected shape and therefore use the data to calculate an upper limit for the existence of this  $\tau$  decay mode in an analogous manner as for  $\tau \rightarrow e\gamma$ . Varying the peak position of an expected signal (within the expected range) does not change the upper limit significantly. We arrive at the upper limits in table 12. The efficiency for detecting this decay is found to be

Position of peak	Upper limit
1742 MeV	4.2
(1742 - 14) MeV	4.2
(1742 + 14) MeV	4.1

Table 12: Upper limits for  $\tau \rightarrow e\pi^0$  as function of peak position

$$\epsilon_{\text{Selection}}^{\tau \rightarrow e\pi^0} = 0.127$$

With a cross section of  $1.02 \text{ nb}^{-1}$  and a total of 75500  $\tau$  leptons ( $37 \text{ pb}^{-1}$ ) we thus arrive at an upper limit for the branching ratio:

$$\text{BR}(\tau \rightarrow e\pi^0) < \frac{4.2}{0.127} \frac{1}{75500} = 4.4 \times 10^{-4} (90\% \text{ CL})$$

## 7 Conclusions

We presented an analysis of  $\gamma X \rightarrow \gamma\tau\bar{\tau}$  type final states in decays of the  $\Upsilon$  and  $\Upsilon'$  resonances. No obvious significant enhancement in the corresponding photon spectra were observed. The analysis represents the first search for this final state in  $\Upsilon'$  decays. In the  $\Upsilon$  case we achieved an improvement for masses  $M_X$  near the  $\Upsilon$  ( $E_\gamma \leq 1 \text{ GeV}$ ). The upper limits obtained

$$\begin{aligned} \text{BR}(\Upsilon \rightarrow \gamma X \rightarrow \gamma\tau\bar{\tau}) &< 1 \times 10^{-3} \\ \text{BR}(\Upsilon' \rightarrow \gamma X \rightarrow \gamma\tau\bar{\tau}) &< 2 \times 10^{-3} \end{aligned}$$

cannot exclude the production of a standard (minimal) Higgs boson in  $\Upsilon, \Upsilon'$  decays predicted to be

$$\text{BR}(\Upsilon, \Upsilon' \rightarrow \gamma \text{Higgs}) \approx 10^{-4} - 10^{-5}$$

They can however be used to constrain the ratio of vacuum expectation values for models with two Higgs doublets.

The search for Higgs bosons in the  $\gamma\tau\bar{\tau}$  final state might prove to be very important in case the Higgs coupling to  $\tau$  pairs should dominate. A search for Higgs  $\rightarrow c\bar{c} \rightarrow$  Hadrons, ( $c =$  charmed quark) in a high multiplicity environment would then no longer be sensitive.

The second part of this work was devoted to exotic decay modes of the  $\tau$  lepton. Composite model theories, which provide a natural explanation for the rich spectrum of quarks and leptons, predict corrections to parameters as well as exotic decay channels. The corrections are very tiny and therefore not sensitive. Exotic decays of the  $\tau$  lepton such as  $\tau \rightarrow e\gamma$  and  $\tau \rightarrow e\pi^0$  on the other hand provide a way to find limits on the compositeness mass scale  $\Lambda$ .

Our limits of

$$\text{and} \quad \begin{aligned} \text{BR}(\tau \rightarrow e\gamma) &< 3.4 \times 10^{-4} \\ \text{BR}(\tau \rightarrow e\pi^0) &< 4.4 \times 10^{-4} \end{aligned}$$

improve considerably existing limits of previous experiments (in particular  $\tau \rightarrow e\pi^0$ ). The limit on  $\tau \rightarrow e\gamma$  can be used to set a lower limit on the compositeness scale

$$\Lambda > 65 \text{ TeV}$$

# A Particle Identification

## A.1 Introduction

In the following we will describe the methods of particle identification in the Crystal Ball detector. Since it is a non magnetic device the identification will be based mostly on the crystal information.

First we will describe the behaviour of different particle types like  $e$ ,  $\mu$ ,  $\pi$ ,  $\gamma$  in the detector. Then we will introduce the concept of pattern cuts and how it can be used for particle identification. For  $\pi^0/\gamma$  separation we will add a method for reconstructing the invariant mass of a shower from its energy deposition in the ball.

## A.2 Signature of Particles

In principle we can subdivide the particles according to their interaction in the NaI(Tl) of the detector as in table 13.

$e, \gamma(\pi^0 \rightarrow \gamma\gamma)$	electromagnetic shower
$\mu$	minimum ionizing
$\pi$	minimum ionizing or hadronic shower

Table 13: Particle types and their interactions in NaI(Tl)

An electromagnetic shower is induced by the joint reactions of bremsstrahlung and pair production. Both processes can only take place in the presence of a nucleus which ensures simultaneous conservation of energy and momentum. A high energetic electron entering the NaI(Tl) will radiate a bremsstrahlung photon which in turn converts into an  $e^-e^-$  pair and so on. The number of particles grows very rapidly and the average energy per particle will decrease accordingly. The average mean free path between these processes is the so called radiation length. The energy deposited will be confined to a certain angular cone around the initial particles impact. Finally the process comes to an end when the probability for energy loss of the electrons by ionization becomes bigger than the probability for bremsstrahlung. In the case of a gamma ray the same processes occur besides the first process being pair production. For a detailed account see reference [49]. The important features for particle identification are

- Almost all energy of the particle will be seen in the detector since its thickness is  $15.7 X_0$  ( $X_0$  = radiation length).
- The energy will be deposited in a relatively small cone, in our case a group of 13 crystals ( $\Sigma_{13}$ ), characterized by the so called Moliere radius.



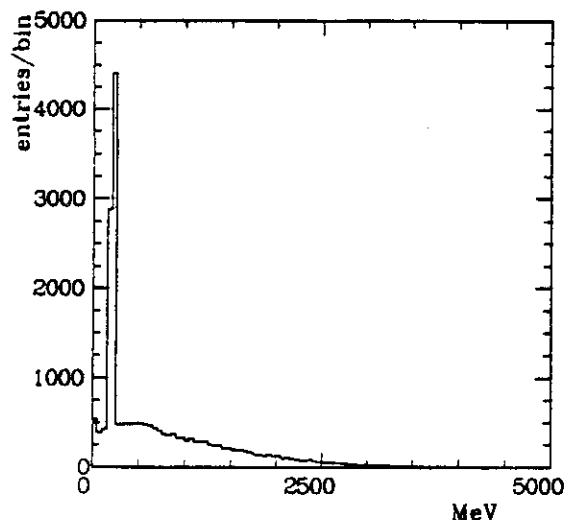


Figure 81: Seen energy for 5 GeV pions

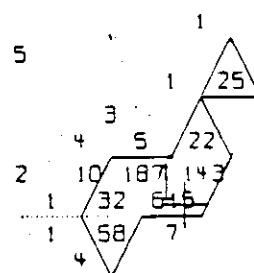


Figure 82: Pion of 5 GeV

Figure 78 shows a 5 GeV muon in the NaI(Tl) crystals.

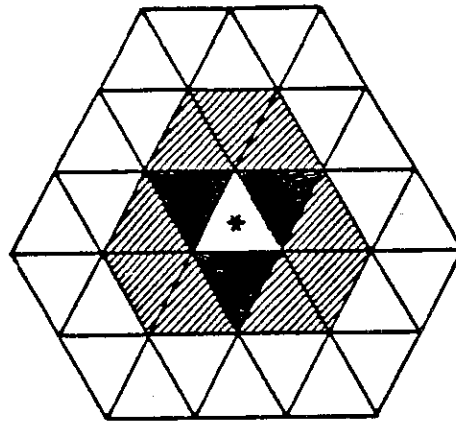
An interacting pion finally will have a fairly irregular behaviour. Because the Crystal Ball detector is only 1 nuclear interaction length thick a pion will undergo a nuclear interaction in about 64% of the cases. Many nuclear processes (strong interaction) will contribute and thus the energy deposited will not be predictable in such a precise manner as for electrons and photons. In figure 81 we display the energy seen in the detector for a 5 GeV pion. The 'minimum ionizing' peak at about 205 MeV is due to the above 36% of non interacting pions. The main features are

- Energy deposition from minimum ionization up to the total energy
- Spread over many crystals with irregular pattern

Figure 82 finally shows a 5 GeV pion in the ball.

### A.3 Patterns

The above described different particle types can be characterized by the form of their energy deposit. An electromagnetic shower will be fairly symmetric, a minimum ionizing particle will leave almost all its energy in one crystal and an interacting pion will exhibit



\* Central Module Hit  
by Photon  
 ■ 3 nearest Neighbours  
 ■ + ▨ = 12 Neighbours

Figure 83: Definition of  $E_1, E_2, E_4$  and  $E_{13}$

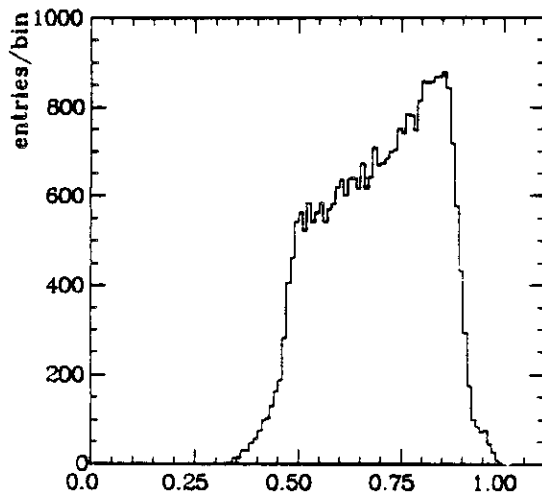


Figure 84:  $\frac{E_1}{E_4}$  for electrons

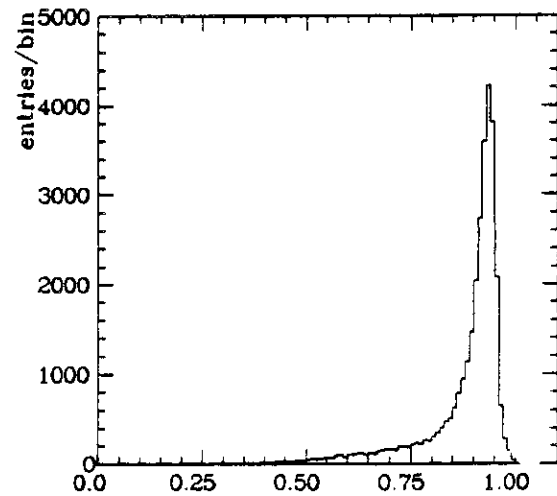


Figure 85:  $\frac{E_4}{E_{13}}$  for electrons

an asymmetric distribution in the crystals. These different characteristics can be used for particle identification. The relevant quantities are  $E_1, E_2, E_4, E_{13}$  which are defined in figure 83 as well as their ratios. In figures 84 to 89 we display various of these quantities for electrons, pions and muons with energies between 500 MeV and 3 GeV (distributed flat in momentum). The cuts used in the various analyses are accumulated in table 14. We observe a clear separation between electrons and muons as well as between pions and electrons.

#### A.4 $\pi^0/\gamma$ separation

Photons from  $\pi^0$ s above  $E_{\pi^0} \approx 600$  MeV tend to overlap such that they appear as one single bump in the detector. Gammas and  $\pi^0$ s can be separated by pattern cuts only

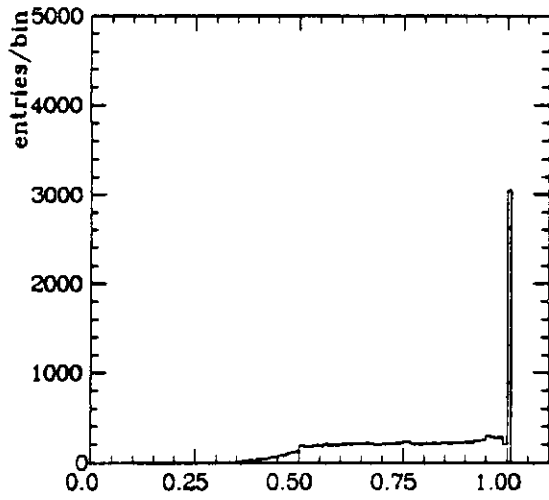


Figure 86:  $\frac{E_1}{E_4}$  for pions

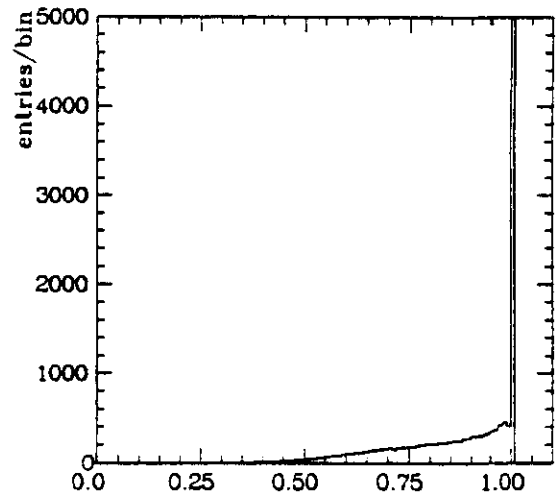


Figure 87:  $\frac{E_4}{E_{13}}$  for pions

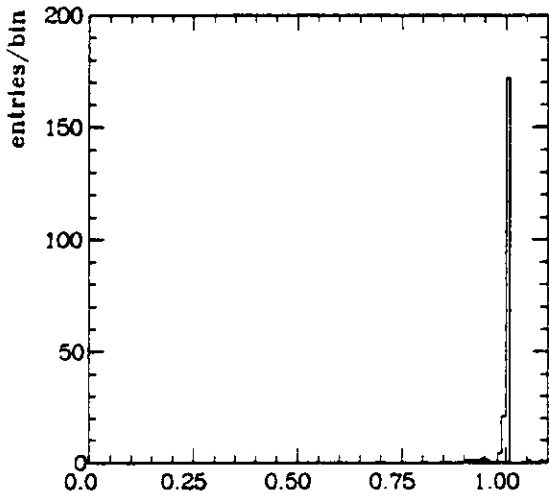


Figure 88:  $\frac{E_1}{E_2}$  for muons

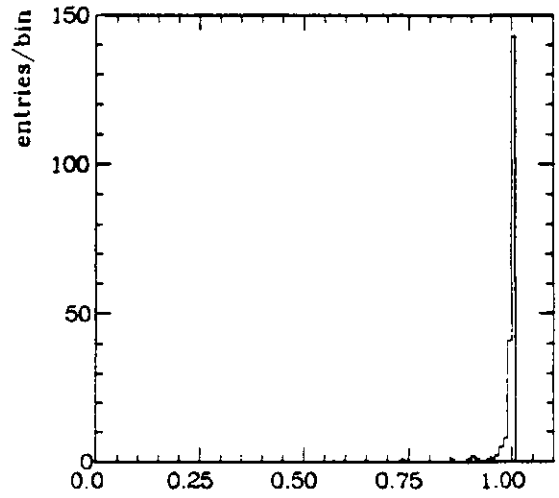


Figure 89:  $\frac{E_4}{E_{13}}$  for muons

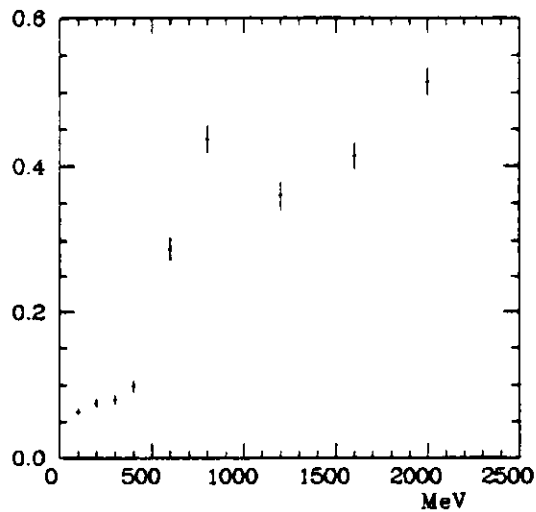


Figure 90: Probability for a  $\pi^0$  to pass a photon pattern cut



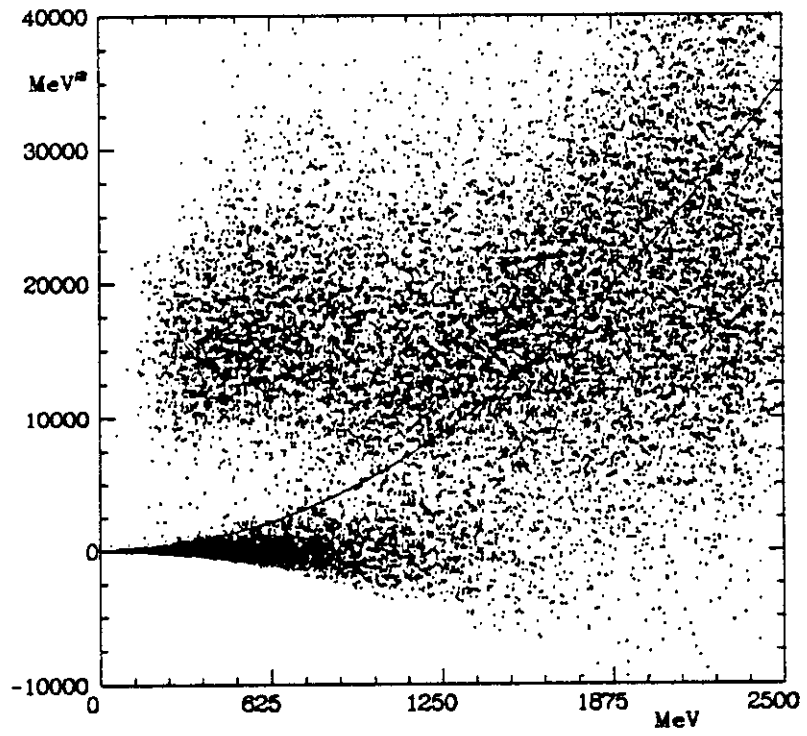


Figure 93: Shower mass for  $\pi^0$  s

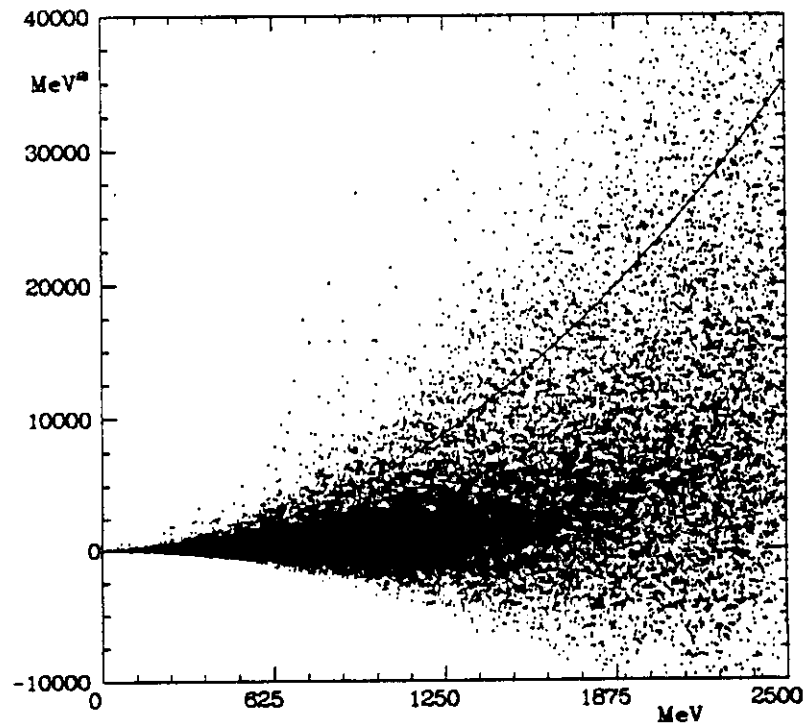


Figure 94: Shower mass for gammas

## B Monte Carlo Techniques

### B.1 Introduction

In the following we will describe how to use Monte Carlo techniques to convert purely experimental results (number of events of a certain type) into quantities which can be compared with theory (e.g. decay width for a certain process). In principle we could do this conversion analytically by using all our knowledge about the physics of the process under investigation and the response of the detector to certain types of particles. This however proves to be impossible due to the large number of processes taking place. For example it is extremely hard to calculate analytically the response of a crystal and its wrapping (see chapter 3.2.1) to a showering particle. The individual processes taking place are known, the electromagnetic ones very well, the ones involving strong interaction to a less extent. It is the enormous number of subsequent steps which renders the analytical calculation impossible. Therefore we can try to simulate them using random distributed numbers to account for the random nature of the processes involved. An electron for example undergoes bremsstrahlung with exponentially decreasing probability, parameterized by the radiation length. Thus we can expect that with a large number of samplings according to this theoretical probability we will resemble the overall features of the process. Repetition of this simulation of the processes involved will finally supply us with a sample of 'events' which should be as random in nature as the real world. These events then enable us to translate the experimental results back to the quantities of the underlying process (to be compared with theory).

Moreover we can use this so called Monte Carlo data sample to optimize the selection criteria for the reaction under investigation. We will divide the discussion into two parts:

- Simulation of the physics involved, e.g.  $\Upsilon, \Upsilon' \rightarrow \gamma X \rightarrow \gamma \tau \bar{\tau}$  (STEP1)
- Simulation of the detector response to the final state particles (STEP2)

### B.2 STEP1

Here we will describe how to generate four-vectors of final state particles for the reactions

- $\Upsilon, \Upsilon' \rightarrow \gamma X \rightarrow \gamma \tau \bar{\tau}$
- $e^+ e^- \rightarrow \tau \bar{\tau}(\gamma)$ ,  $\tau \rightarrow$ conventional decay channels
- $e^+ e^- \rightarrow \tau \bar{\tau}(\gamma)$ ,  $\tau \rightarrow e \gamma \tau \rightarrow e \pi^0$

The first process is relatively easy to simulate since it consists of two subsequent two body decays. The energies of the photon and the particle X are determined by the mass of the  $\Upsilon$  and X. The angular distribution of the particles depends on the spin of X.

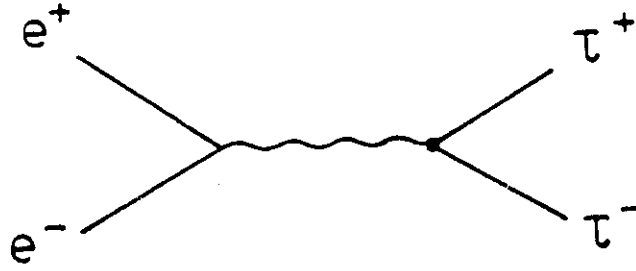


Figure 95: Lowest order diagram for  $e^+e^- \rightarrow \tau\bar{\tau}$

For a spin 0 object the angular distribution is of the form  $1 + \cos^2 \Theta$ , where  $\Theta$  is the angle of the photon with respect to the  $e^+$  beam and isotropic in the azimuth  $\Phi$ . For a detailed description of the helicity formalism which leads to the above distributions see reference [53]. In the sequential decay  $X \rightarrow \tau\bar{\tau}$  the angular distribution is isotropic in  $\cos \Theta$  and  $\Phi$  in the  $X$  restframe. A Lorentz boost yields the four-momenta of the various final state particles in the laboratory system. The sampling of  $1 + \cos^2 \Theta$ ,  $\cos \Theta$  and  $\Phi$  is accomplished using random numbers, for a detailed description of sampling methods see reference [54]. The  $\tau$  lepton decays are simulated according to the modes given in table 2.

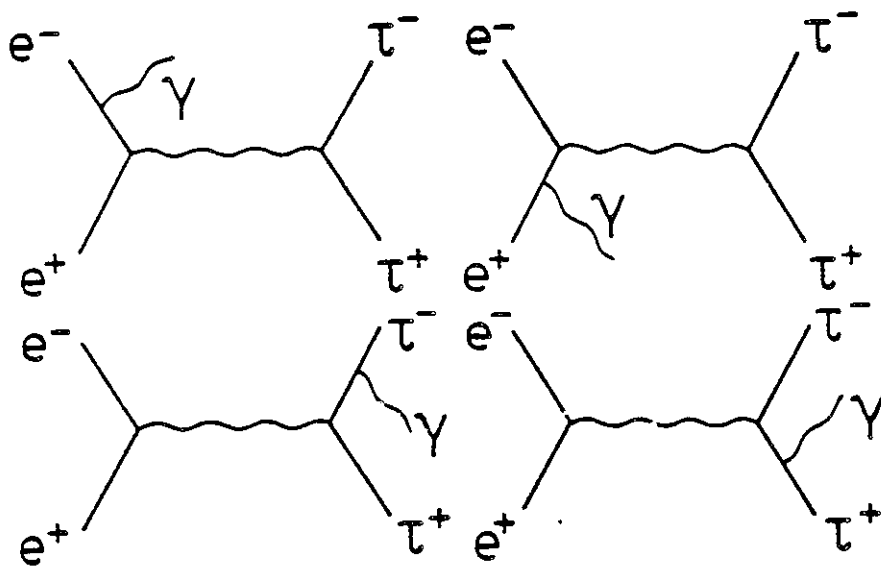
The second process, radiatively corrected  $\tau$  pair production is more involved. In lowest order we have to account for the diagram in figure 95. The cross section is given by

$$\frac{d\sigma}{d\Omega} = \frac{\alpha^2}{4S} \left(1 - \frac{4M^2}{S}\right)^{1/2} \left(1 + \cos^2 \Theta + \frac{4M^2}{S} \sin^2 \Theta\right)$$

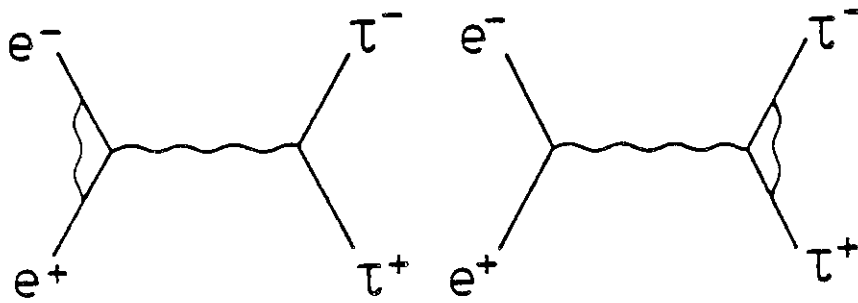
where  $\Theta$  is the angle between electron and  $\tau$  lepton,  $\sqrt{S}$  is the CMS energy and  $M$  is the  $\tau$  mass. One has to add corrections to this process, namely virtual and bremsstrahlungs corrections, see figure 96. Upon integrating the bremsstrahlungs spectrum we find it to be infrared divergent. Including the virtual corrections cures these divergences. In order to generate radiatively corrected  $\tau\bar{\tau}$  final states we can use two different methods.

In the first method we choose a photon momentum  $k_0$  below which a photon would no longer be detected. A typical value is 1% of  $E_{\text{Beam}}$  ( $\approx 50$  MeV in our case). The total cross section for photon emission with momenta less than  $k_0$ ,  $\sigma_{\text{SOFT}}$ , can be calculated as well as  $\sigma_{\text{HARD}}$  for photon momenta above  $k_0$ . We decide which type of event to generate upon the ratio  $\frac{\sigma_{\text{SOFT}}}{\sigma_{\text{HARD}}}$ . In case we are in the soft region we then generate a nonradiative  $\tau\bar{\tau}$  pair according to the above cross section. In the hard region we generate a three body  $\gamma\tau\bar{\tau}$  final state.

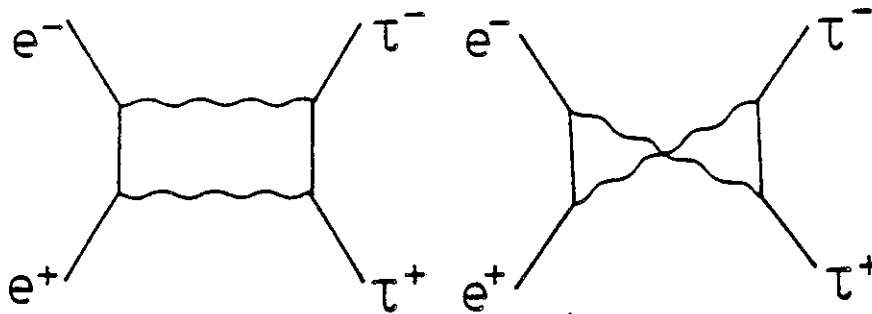
Another possibility, chosen here, is to make use of the so called 'exponentiation'. For low photon momenta we can exponentiate the leading log part of the virtual corrections, thus accounting for the arbitrary number of very soft photons being emitted (infrared catastrophe of the second kind). We can extend this treatment also to hard photons.



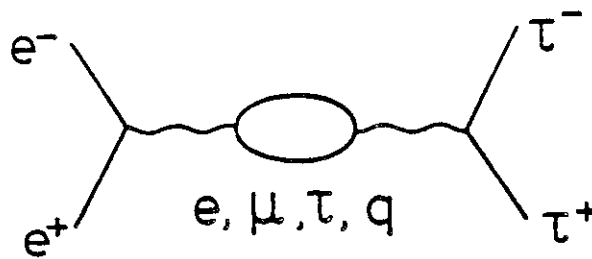
a) bremsstrahlung



b) vertex corrections



c) box diagrams



d) vacuum polarization

Figure 96: Corrections to  $e^+e^- \rightarrow \tau\bar{\tau}$ , a) bremsstrahlung, b) vertex corrections, c) box diagrams and d) vacuum polarization

This leaves us with an integrated, non divergent, photon spectrum which can be used for random sampling of photon momenta. The three body final state is then generated similar as above. For a detailed discussion of the underlying theory, see reference [55].

It should be noted that including corrections due to  $Z_0$  exchange and angular correlations, see references [56] has a negligible effect on the detection efficiencies for the process under discussion. The same is true for  $\alpha^4$  corrections, see reference [57].

Finally we treat the decays  $\tau \rightarrow e\gamma$  and  $\tau \rightarrow e\pi^0$ , where the second  $\tau$  lepton decays conventionally. Again as in the first reaction simple two body kinematics with an isotropic angular distribution in  $\cos\Theta$  and  $\Phi$  in the  $\tau$  restframe is involved. This concludes the list of generators used in this work.

### B.3 STEP2

This part of the event simulation starts from the generated four-vectors and propagates the particles through all detector components. It simulates the corresponding physical processes leading to signals in the various detector components. These processes can be divided into two classes, electromagnetic and hadronic interactions. The electromagnetic part is generated by EGS (Electron Gamma Simulation), see reference [58] and the hadronic part by GHEISHA (Gamma Hadron Electron Interaction SH(A)ower code), reference [59].

#### B.3.1 Electromagnetic Interactions

Electrons (positrons) loose energy upon passage through matter and photons are absorbed. An electron colliding with an atom will excite this atom and the following deexcitation will yield a low energy gamma or electron which deposits its energy locally. This collision energy loss dominates at low energies whereas shower development due to successive pair production and bremsstrahlung (see appendix A) dominates at higher energies. The shower gets a lateral spread due to the opening angles induced by the elementary processes. Coulomb and Compton scattering also contribute to this spread of the shower.

The simulation itself is decomposed into simulating the transport and the individual interactions of the single particle. The transport proceeds in steps which are a fraction of the interaction (radiation) length until an interaction takes place (to be determined by random sampling) or the particle energy drops below a cut-off. Below this cut-off the particle energy is deposited locally. For a description of all the details see the EGS writeup, quoted above.

The agreement between data and Monte Carlo simulation is very good. This can be seen in figures 97 and 98 taken from reference [60] for a comparison of data and Monte Carlo predictions for electrons in NaI(Tl). Figure 97 shows the observed and calculated

resolution as a function of electron energy and figure 98 displays the energy resolution versus beam displacement.

### B.3.2 Hadronic Interactions

The simulation of hadrons passing through matter is much more involved than for electrons and photons. Whereas only a few processes calculable in QED contribute to EGS, the hadronic transport code, GHEISHA, simulates a multitude of processes which partly have to be adjusted using experimentally determined parameters. The particle transport, multiple scattering and energy loss by ionization are treated similarly to EGS. The cross sections for elastic and inelastic hadron nucleon interactions are taken from data and the dependence on atomic number is fitted. Various empirical and semi empirical models are used to predict final state multiplicities and momentum distributions in inelastic processes. The agreement between Monte Carlo prediction and experimental data is very good despite the empirical approximations made. See figures 99 and 100 taken from reference [61] for a comparison of Monte Carlo and data for pions in BGO. Figure 99 compares the energy deposited for data and Monte Carlo and figure 100 shows the longitudinal shower profiles in BGO.

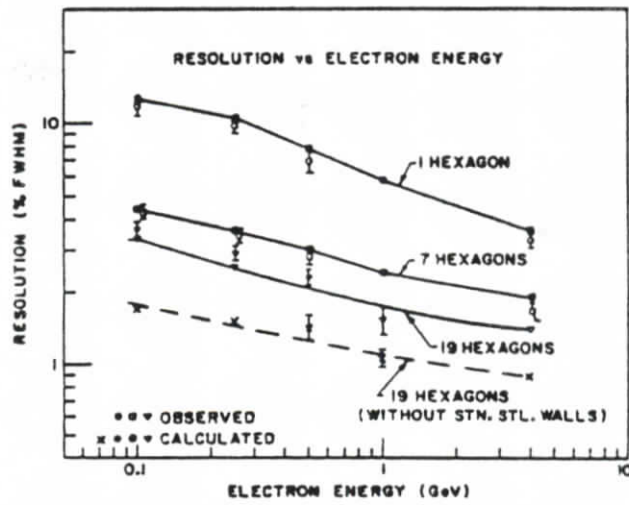


Figure 97: Resolution versus electron energy

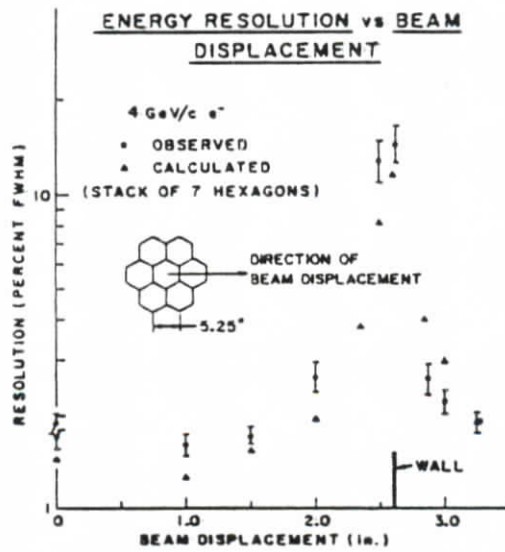


Figure 98: Resolution versus beam displacement

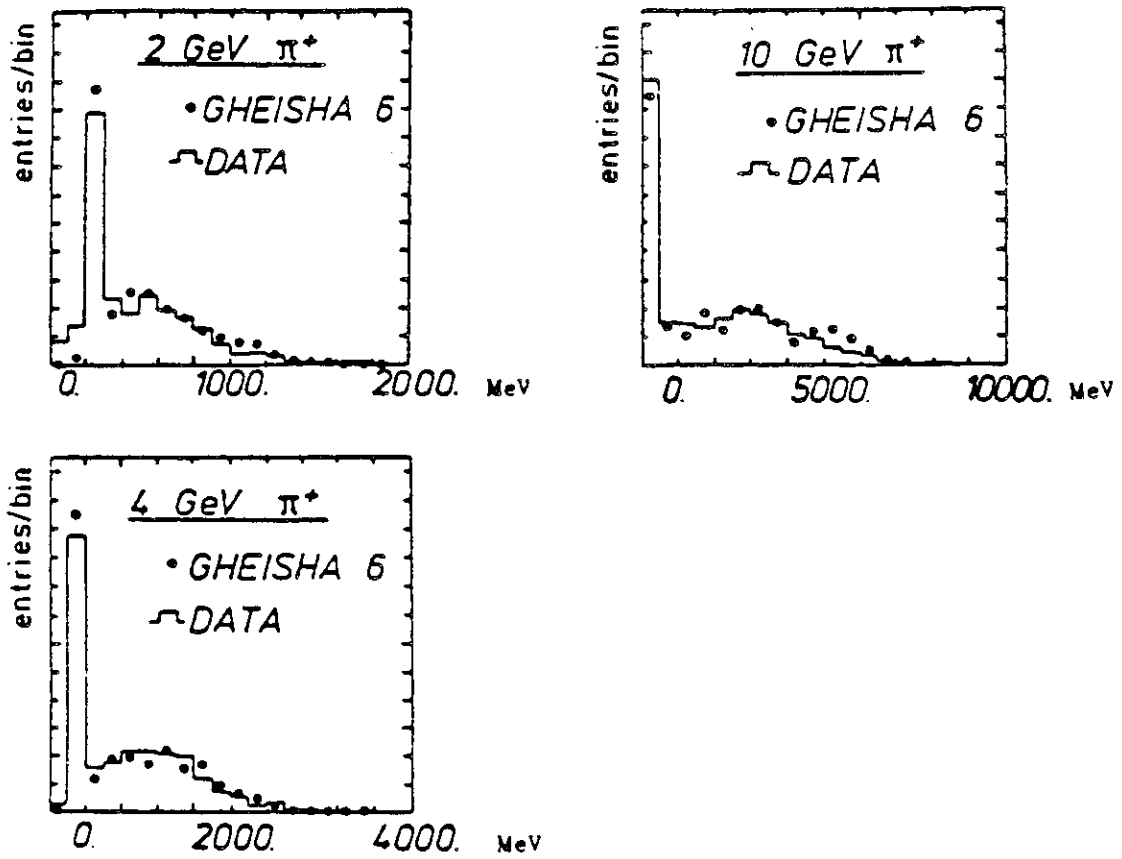


Figure 99: Energy deposited by pions in BGO, Monte Carlo and data

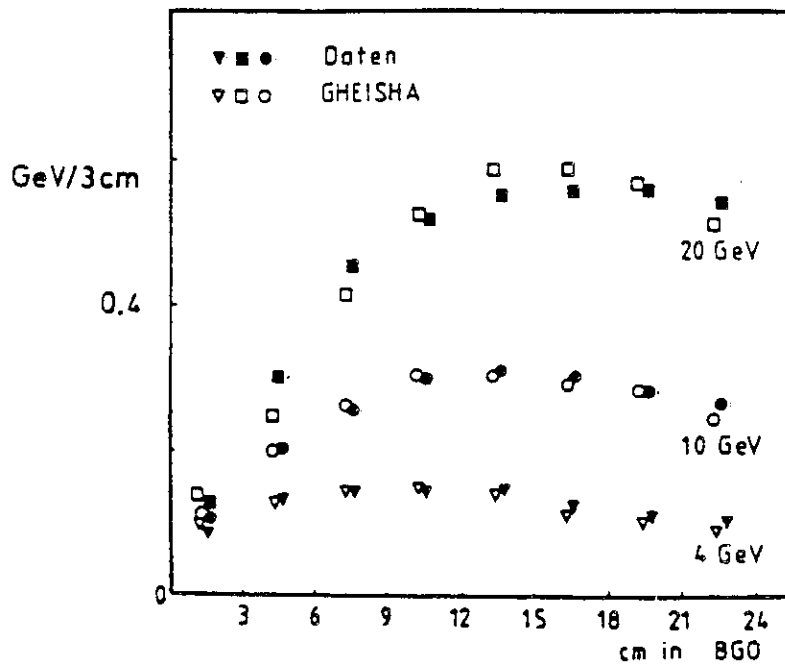


Figure 100: Longitudinal shower profile for pions in BGO, Monte Carlo and data

# C Statistical Methods

## C.1 Introduction

In the following we will introduce some basic statistical tools which will enable us to make predictions on parameter values based on the experiment performed. The uncertainties involved can also be calculated within this approach. We will start from the concept of a likelihood function and show that, by maximization, it allows the determination of parameters from experimental data. Finally we will describe how to obtain limits on parameters if their value does not differ significantly from zero.

## C.2 Likelihood Function

Suppose we have a set of experimental data, e.g. number of events per bin,  $N_i$ ,  $i = 1, n$ . Moreover we have a theoretical expectation of how the number of events per bin should be distributed,  $f_i$ ,  $i = 1, n$ . These  $f_i$  depend on  $m$  parameters  $\lambda_j$ ,  $j = 1, m$ . We then define a likelihood as

$$L(\lambda_j) = \prod_{i=1}^n f_i(N_i, \lambda_j).$$

We can interpret this likelihood function as a measure for the probability to observe the particular sample of experimental data originating from the underlying function  $f(\lambda_j)$ . Due to statistical fluctuations, e.g. governed by Poisson statistics, the experimental data  $N_i$  will deviate from the predicted  $f_i$  even for the right set of parameters  $\lambda_j$ . The likelihood  $L$  however will be maximal. Therefore a numerical method for maximizing a function has to be used to get the parameters  $\lambda$ . Such a program is MINUIT, see reference [62]. For a detailed collection of maximizing procedures see reference [63].

A likelihood for gaussian distributed bin contents would read

$$L(\lambda) = \prod_{i=1}^n \exp \frac{-(N_i - f_i(\lambda))^2}{2f_i(\lambda)}$$

Maximizing  $L$  is equivalent to minimizing  $-\ln(L)$  and thus

$$-\ln(L) = \sum_{i=1}^n \frac{(N_i - f(\lambda))^2}{2f_i(\lambda)} = \frac{1}{2}\chi^2$$

turns out to resemble the wellknown Pearson  $\chi^2$ . Thus maximizing a likelihood is equivalent to minimizing a  $\chi^2$  in the case of gaussian statistics.

Since we have in our spectra only a very small number of entries per bin we have to use Poisson statistics. In order to use gaussian statistics we would have to increase the bin size. This however would diminish the experimental information. A likelihood for Poisson statistics then reads

$$L(\lambda) = \prod_{i=1}^n \frac{\exp(-f_i(\lambda))f_i(\lambda)^{N_i}}{N_i!}$$

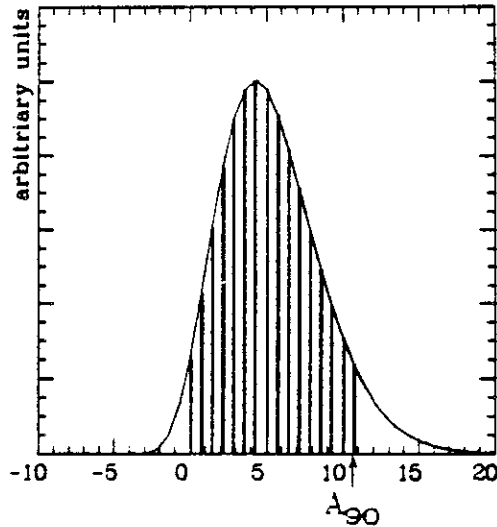


Figure 101: Likelihood as function of amplitude A

In the following we will show an example of such a likelihood. The parameter  $\lambda$  will be the amplitude of a possible signal.

We use the final photon spectrum from the  $\gamma\tau\bar{\tau}$  search, figure 51. We want to fit a gaussian shaped signal (due to our resolution function) superimposed on a smooth polynomial background to this spectrum. We can vary the amplitude A of the signal and keep all other parameters fixed to their values at maximum likelihood. In figure 101 we display the likelihood as a function of A for a particular photon energy and observe a most probable amplitude of 4.52 counts. The likelihood looks fairly gaussian, although computed using poisson statistics due to the very small number of entries <sup>16</sup>. It is suggestive to define an error  $\sigma$  on the most probable amplitude  $A_0$  (in analogy to gaussian statistics) such that 68% of the likelihood is within a window  $A_0 \pm \sigma$ . We observe that  $A_0$  differs only by  $1.45 \sigma$  from zero. Thus the probability for  $A_0$  not being caused by a fluctuation of the background is only 85% (i.e. the probability for a background fluctuation of  $< 1.45 \sigma$ ). In such a case we do not claim this to be a real signal since the probability for a fluctuation of the background is so high. We prefer to calculate an upper limit for the amplitude at a certain confidence level.

### C.3 Upper Limits

An upper limit  $A_X$  at X% confidence level implies that there is a X% probability for the observed number of counts not to originate from a signal with an amplitude greater than  $A_X$ . This means that the fluctuations of the background are too large to give a positive proof for the existence of a signal. On the other hand we neither can exclude a possible signal of amplitude less than  $A_X$  at a confidence level of X%. We integrate the likelihood for positive amplitudes (since a negative signal would be unphysical) up

<sup>16</sup>The distortion at the lower edge is an artifact.

to X%. The amplitude where we reach X% is then the upper limit. Hatched indicated in figure 101 is the 90% area according to

$$\int_0^{A_0} L(A)dA = 0.9 \int_0^{\infty} L(A)dA$$

The point labelled  $A_{90}$  is then the 90% confidence level upper limit.

#### C.4 Summary

The likelihood method allows us to calculate the best estimate for parameters of an underlying theoretical hypothesis. The behaviour of this likelihood as a function of parameters allows us to define an uncertainty on the determination of the parameters. The statistical significance emerges then as the ratio of most probable value to uncertainty. If this significance is too low, an upper limit  $A_0$  at say 90% confidence level can be computed. This allows to exclude a signal of more than  $A_0$  counts at a 90% confidence level.

## References

- [1] S.L. Glashow, Nucl. Phys. 22 (1961) 579  
S. Weinberg, Phys. Rev. Lett. 19 (1967) 1264  
A. Salam, 'Elementary Particle Theory', Ed. N.Svartholm, Almqvist and Wiksell, Stockholm (1968), pp. 367
- [2] F.J. Hasert *et al.*, Phys. Lett. B46 (1973) 121, Phys. Lett. B46 (1973) 138
- [3] G. Arnison *et al.* Phys. Lett. B122 (1983) 103, Phys. Lett. B126 (1983) 398, M. Banner *et al.*, Phys. Lett. B122 (1983) 476  
P.Bagnaia *et al.*, Phys. Lett. B129 (1983) 130
- [4] P.W. Higgs, Phys. Lett. 12 (1964) 132,  
P.W. Anderson, Phys. Rev. 130 (1963) 439
- [5] S. W. Herb *et al.*, Phys. Rev. Lett. 39 , 252 (1977).
- [6] C. Berger *et al.*, Phys. Lett. B76 (1978) 243  
C.W. Darden *et al.*, Phys. Lett. B76 (1978) 246  
J.K. Bienlein *et al.*, Phys. Lett. B78 (1978) 360  
C.W. Darden *et al.*, Phys. Lett. B78 (1978) 364
- [7] M.L. Perl *et al.*, Phys. Rev. Lett. 35 (1975) 1489  
G.J. Feldman *et al.*, Phys. Rev. Lett. 38 (1977) 117
- [8] S. Sakata, Progr. Theor. Phys. 16 (1956) 686
- [9] M. Gell-Mann, Phys. Lett. 8 (1964) 214  
G. Zweig, CERN-TH-412 (1964)
- [10] O.W. Greenberg, Phys. Rev. Lett. 13 (1964) 598
- [11] C.E. Carlson, T.H. Hansson and C. Peterson, Phys. Rev. D30 (1984) 1594  
M. Chanowitz and S. Sharpe, Nucl. Phys. B222 (1983) 211  
B. Berg and A. Billoire, Nucl. Phys. B221 (1983) 109  
K. Ishikawa, M. Teper and G. Schierholz, Phys. Lett. B116 (1982) 429
- [12] C.N. Yang, Phys. Rev. 77 (1950) 242
- [13] S. Okubo, Phys. Lett. 5 (1963) 165  
G. Zweig, CERN Preprints CERN-TH-401, 402,412 (1964)  
J. Iizuka Prog. Phys. Suppl. 37-38 (1966) 21
- [14] M. Kobayashi and T. Maskawa, Progr. Theor. Phys. 49 (1973) 652

- [15] J. Goldstone, *Nuovo Cim.* 19 (1964) 154
- [16] P.W. Higgs, *Phys. Lett.* 12 (1964) 132, *Phys. Rev. Lett.* 13 (1964) 508, *Phys. Rev.* 145 (1966) 1156  
 F. Englert and R. Brout, *Phys. Rev. Lett.* 13 (1964) 321  
 C.S. Guralnik, C.R. Hagen and T.W.B. Kibble, *Phys. Rev. Lett.* 13 (1964) 585  
 T.W.B. Kibble, *Phys. Rev.* 155 (1967) 1554
- [17] S. Weinberg, *Phys. Rev. Lett.* 36 (1976) 294  
 A.D. Linde, *JETP Lett.* 23 (1976) 64
- [18] R.S. Willey and H.-L. Yu, *Phys. Rev.* D26 (1982) 3287
- [19] B.W. Lee, C. Quigg and H.B. Thacker, *Phys. Rev.* D16 (1977) 1519
- [20] Review of Particle Properties, *Phys. Lett.* B176 (1986)
- [21] H.E. Haber and J.L. Kane, *Phys. Rep.* 117 (1985) 75
- [22] H.E. Haber and G.L. Kane, *Phys. Lett.* B135 (1984) 196  
 M.B. Wise, HUTP-81/A017 (1981)  
 M. Drees and K. Grassie, *Phys. Lett.* B149 (1984) 367  
 K. Lane, S. Meskov and F. Wilczek, *Phys. Rev. Lett.* 53 (1984) 1718  
 S.L. Glashow and M. Machacek, *Phys. Lett.* B145 (1984) 302  
 H. Georgi, A. Manohar and G. Moore, *Phys. Lett.* B149 (1984) 234  
 R.S. Wiley, *Phys. Rev. Lett.* 52 (1984) 585  
 M. Shin, H. Georgi and M. Axenides, *Nucl. Phys.* B253 (1985) 205
- [23] F. Wilczek, *Phys. Rev. Lett.* 39 (1977) 1304
- [24] M.I. Vysotsky, *Phys. Lett.* B97 (1980) 159  
 J. Ellis, K. Enqvist and D.V. Nanopoulos S. Ritz, *Phys. Lett.* B158 (1985) 417  
 P. Nason, CU-TP-346 (1986)
- [25] H. Albrecht *et al.*, *Phys. Lett.* B154 (1985) 452
- [26] H. Albrecht *et al.*, *Phys. Lett.* B163 (1985) 404
- [27] E. Fernandez *et al.*, *Phys. Rev. Lett.* 54 (1985) 1624
- [28] F.J. Gilman and S.H. Rhie, *Phys. Rev.* D31 (1985) 1066
- [29] W. Ruckstuhl, CALT 68-1232 (1985)
- [30] W. Buchmüller and D. Wyler, *Nucl. Phys.* B268 (1986) 621

- [31] D. Zeppenfeld, private communication
- [32] W. Buchmüller, private communication
- [33] K.G. Hayes *et al.*, Phys. Rev. D25 (1982) 2869
- [34] K. Wille, DESY 81-047 (1981)
- [35] K. Wille, DESY M 83-16 (1983)
- [36] P. Schmitt, Diploma thesis (unpublished), Würzburg (1983)
- [37] D.P. Barber *et al.*, DESY 83-065 (1983)
- [38] A.A. Sokolov and I.M. Ternov, Sov. Phys. Dokl. 8 (1964) 1203
- [39] D.P. Barber *et al.*, Phys. Lett. B135 (1984) 498
- [40] H. Albrecht *et al.*, Phys. Lett. B134 (1984) 137
- [41] M. Oreglia, PhD thesis (unpublished), SLAC 236 (1980)
- [42] J.E. Gaiser, PhD thesis (unpublished), SLAC 255 (1982)
- [43] Y. Chan *et al.*, IEEE Trans. on Nucl. Sci., NS-25 (1978) 333
- [44] J.S. Leffler, PhD thesis (unpublished), SLAC 293 (1986)
- [45] D.M. Gelfman, PhD thesis (unpublished), SLAC 286 (1985)
- [46] R. Nernst, PhD thesis (unpublished), DESY F-31-85-01 (1985)
- [47] B. Anderson *et al.*, Phys. Rep. 97 (1983) 33
- [48] F.A. Berends and R. Kleiss, Nucl. Phys. B228 (1983) 537
- [49] K. Kleinknecht, 'Detektoren für Teilchenstrahlung',  
B.G. Teubner Stuttgart (1984)
- [50] M. Kobel, Diploma Thesis (unpublished), Erlangen (1986)
- [51] W.T. Eadie *et al.*, 'Statistical methods in physics', North Holland Pub. (1971)
- [52] R. Lee, PhD thesis (unpublished), SLAC 282 (1985)
- [53] J.D. Richman, CALT 68-1148 (1984)
- [54] F. James, CERN DD/80/6 (1980)
- [55] F.A. Berends and R. Kleiss, Nucl. Phys. B178 (1981) 141

- [56] S. Jadach and Z. Was, Acta Physica Polonica B15 (1984) 1151, Comp. Phys. Comm. 36 (1985) 191
- [57] U. Schneekloth, private communication
- [58] R.L. Ford and W.R. Nelson, SLAC 210 (1978)
- [59] H. Fesefeld, Aachen Univ., PITHA 85-02 (1985)
- [60] R.L. Ford *et al.*, IEEE Trans. on Nucl. Sci., NS-24 (1977) 264
- [61] T. Haeck *et al.*, Aachen Univ., PITHA 85-06 (1985)
- [62] F. James and M. Ross, Comp. Phys. Comm. 10 (1975) 343
- [63] F. James, CERN 72-21 (1972)

## Acknowledgements

This thesis is the result of a joint effort of the Crystal Ball group. Therefore I would like to thank all members of this collaboration. I would also like to thank DESY for financial support.

There are however some people who had a particularly important impact on this work. My thesis advisor Prof. M. Scheer taught me in many discussions how to comprehend the interrelationship between physics phenomena. At this place I would like to thank him for his continuous support and interest in my work. Dr. K. Königsmann provided me with many insights into problems of high energy physics. Special thanks go to P. Schmitt, who was a partner in many discussions and, more important, a true friend over all the years since 1982.

Finally I would like to thank my wife Ursula. She is the person who made all this possible, with her love and the tremendous amount of patience which was needed e.g. to bridge the distance Stanford - Hamburg various times. Therefore this thesis is devoted to her.